Imaging of Cranial and Facial Fractures

Mehmet Ruhi Onur, Ilkay Idilman,
and Erhan Akpinar

Contents

M. R. Onur (✉) · I. Idilman · E. Akpinar
Faculty of Medicine, Department of Radiology,
Hacettepe University, Ankara, Turkey

Abstract

Craniofacial fractures represent one of the most frequent encountered emergency settings after motor vehicle accidents, assaults, fall, or other trauma types. Appropriate management of patients with craniofacial fractures depends on a comprehensive assessment of imaging findings including fracture sites, patterns, and associated injuries. Computed tomography is the mainstay imaging technique in craniofacial fractures with its superiorities including thin-section image acquisition and multiplanar and three-dimensional image generation capability. Decision of treatment method and preoperative planning necessitates assessment of imaging features according to current classifications of maxillofacial fractures. Cranial fractures should be evaluated with accompanying intracranial injuries. Maxillofacial fractures manifest with imaging features that usually represent injury mechanism and disruption of facial buttresses. Management of patients with craniofacial fractures can be accomplished by multidisciplinary approach including assessment of imaging features and decision of treatment method to prevent further complications.

1   Introduction

Craniofacial skeleton is formed by multiple articulating bones, which encase critical anatomical structures including the brain and sensorineural organs such as eye, ear, and olfactory system. Craniofacial fractures may result from blunt or penetrating traumas including motor vehicle and pedestrian accidents, work, and sport-related accidents, falls, and assaults. Primary imaging technique in craniofacial trauma is computed tomography (CT) due to its capability of fast imaging, thin-section (submillimeter) acquisition, easy patient positioning and multiplanar reconstruction (MPR), and three-dimensional (3D) reconstruction facilities. 3D post-processing techniques including

surface-shaded display (SSD) and volume rendering (VR) have been widely used in craniofacial fractures. Cinematic rendering (CR) is a novel 3D post-processing CT technique that enables to generate more photo-realistic representations of the human body by using different lightmaps from CT or magnetic resonance imaging (MRI) datasets (Fig. 1) (Dappa et al. 2016). Awareness of imaging findings, anatomical key points, and classifications of fractures is necessary for comprehensive assessment of craniofacial fractures. Appropriate management of craniofacial fractures necessitates assessment of fracture patterns, classifications, and implications for preoperative planning.

2   Cranium

The cranium is a bony structure formed by calvarium (dome-like superior portion of the cranium) and skull base (floor of the cranium). Cranial bones are separated from each other by cranial sutures. The frontal and occipital bones are also included in the calvarial bones and contribute to the skull base skeleton with their horizontally oriented portions. In this section, cranial fractures including squamous part of frontal bone and parietal and occipital bones are presented. Frontal sinus fractures are mentioned in maxillofacial skeleton section since frontal sinus fractures are usually encountered with the fractures of facial skeleton.

2.1   Calvarium

The calvarium is formed by the squamous (superior) portion of the frontal bone anteriorly, parietal bones laterally, and the occipital bone posteriorly. Frontal bone is a smooth, broad, and a bowl-shaped bone that surrounds the anterior cranial fossa. Frontal bone is divided into vertical (squamous) and horizontal (orbital) parts. Squamous part of the frontal bone forms the skeletal part of forehead, while orbital part forms the thin roofs of the orbits. Frontal bones articulate with two parietal bones via the coronal suture and

Fig. 1 CR images of cranium. Anterior (**a**), lateral (**b**), and posterior (**c**) view of cranium on CR images

with nasal bones at the frontonasal suture. Zygomatic, lacrimal, ethmoid, and sphenoid bones constitute other cranial bones, which articulate with the frontal bone. In infants, the halves of the frontal squama are divided by the metopic suture, which is not visible after the age of 6. A remnant of the metopic suture may be visible in 8% of adults and mimic fracture on radiographs (Fig. 2) (Zdilla et al. 2018).

Parietal bones are smooth convex bones, which form superior and lateral aspect of the calvarium. Two parietal bones join in the midline via the sagittal suture. Lambdoid suture is located between parietal bones and occipital bone. Other bony structures that articulate with parietal bones are temporal bones and greater wings of the sphenoid bone. An accessory suture named as intraparietal or sub-sagittal suture in the parietal bone
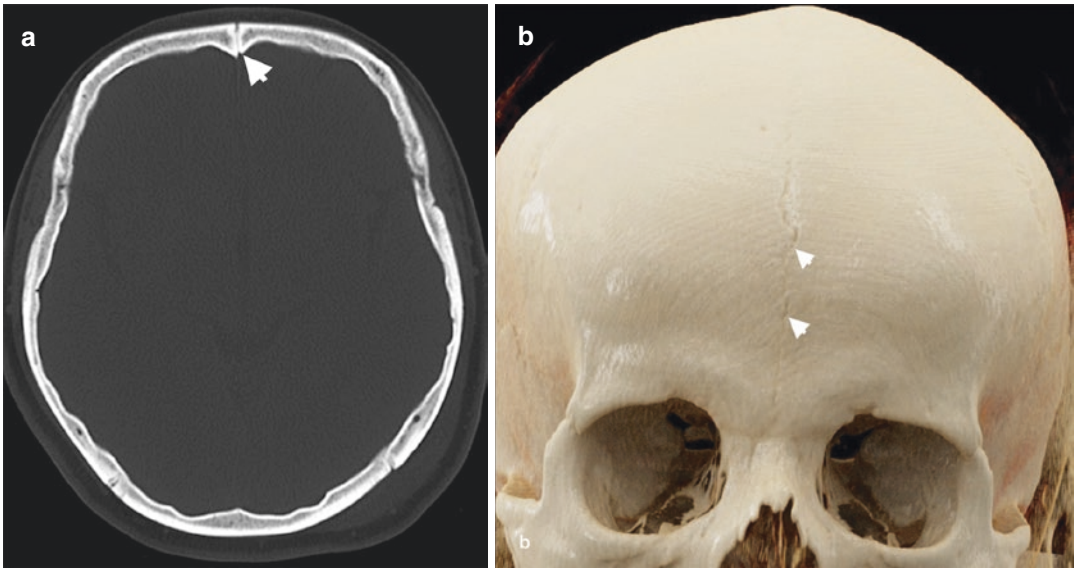
Fig. 2 Metopic suture. Axial CT (**a**) and CR (**b**) images of a 54-year-old woman demonstrate a metopic suture (arrowheads) in the midline extending from bregma to the nasion

may mimic a linear fracture on radiographs (Sanchez et al. 2010).

Occipital bone forms the posterior and inferior parts of the calvarium. Occipital bones articulate with first cervical vertebrae via occipital condyles. Persistent occipital suture that extends from the dorsal aspect of the foramen magnum may mimic occipital fracture. This accessory suture has been shown not to extend more than 2 cm from the edge of the foramen magnum (Sanchez et al. 2010). A longer fissure in the same location represents a fracture.

2.2 Imaging Techniques

Primary imaging modality in the diagnosis of craniofacial fractures is CT. Although plain film radiography is not primarily used in craniofacial fractures, familiarity with radiographic imaging features of craniofacial fractures may be helpful in emergency settings. Skull fractures can be evaluated on radiographs obtained at anteroposterior (A-P) and lateral views of the skull. Occipital fractures can be depicted at the Towne view. The assessment of cranial fractures on radiographs can be difficult in children due to the

presence of numerous synchondroses and unusual accessory sutures, especially in parietal and occipital bones (Sanchez et al. 2010).

The scan area for CT examination in cranial fractures should extend from the skull base to the vertex. CT images should be acquired with thin-section ($\leq$1.25 mm) collimation and reconstructed with at least 2-mm-thick axial, coronal, and sagittal images. CT images should be reviewed at bone and soft-tissue window settings. Bone window setting enhances the margins of the bony cortex and provides the ability to depict localization and extension of cranial fractures, while scalp injuries and intracranial injuries such as extra-axial and intracranial hemorrhages and parenchymal injuries can be detected at soft-tissue window setting.

2.3 Cranial Fractures and Imaging Features

Cranial fractures may be caused by blunt or penetrating trauma. Blunt trauma usually occurs as motor vehicle accidents (MVA), falls, and assaults, whereas penetrating trauma consists of gunshot injury, stabbing, and impalement

(Hijaz et al. 2011). Frontal bone fractures, being the most frequent calvarial bone fracture, occur in 37% of all cranial fractures (Pappachan and Alexander 2006). Blow effects of trauma in parietal and occipital bones are usually minimized secondary to the distribution of impact force through the convexity of these bones. Cranial fractures can manifest as linear (nondisplaced and most frequent form), depressed, diastatic, and comminuted (fragmentation into multiple parts) forms. Linear fractures are characterized by separation of bone edges without displacement. Depressed fracture is defined as displacement of fracture segment deeper than the uninvolved skull. Comminuted fracture is defined as fragmentation of involved calvarial bone into multiple parts and radiation of multiple linear fractures from the point of impact through areas of weakness.

Cranial fractures manifest on radiographs as radiolucent line or depressed osseous fragments (Fig. 3). CT images at bone window setting reveal linear fracture as separation of bone portions with non-sclerotic edges (Fig. 4). Depressed fractures present as displacement of fracture fragment from the uninvolved skull (Fig. 5). Diastatic fracture refers to fracture type that follows a cranial suture and causes widening of the suture (Fig. 6). Comminuted cranial fractures are characterized by multiple fracture fragments with more significant fracture displacement (Fig. 7). In infants and children, cranial fractures more commonly present as diastatic fractures that may also manifest as growing fractures secondary to herniation of cerebrospinal fluid (CSF) or brain parenchyma into the subcutaneous tissue through the relevant dural tear (Mulroy et al. 2012). In children, plain film radiographs demonstrate growing fractures as persistent diastatic fracture enlarging on follow-up imaging. Cross-sectional imaging techniques can demonstrate extension of intracranial tissue or a leptomeningeal cyst between the edges of the growing fracture (Fig. 8) (Carter and Anslow 2009). Differentiation between cranial sutures
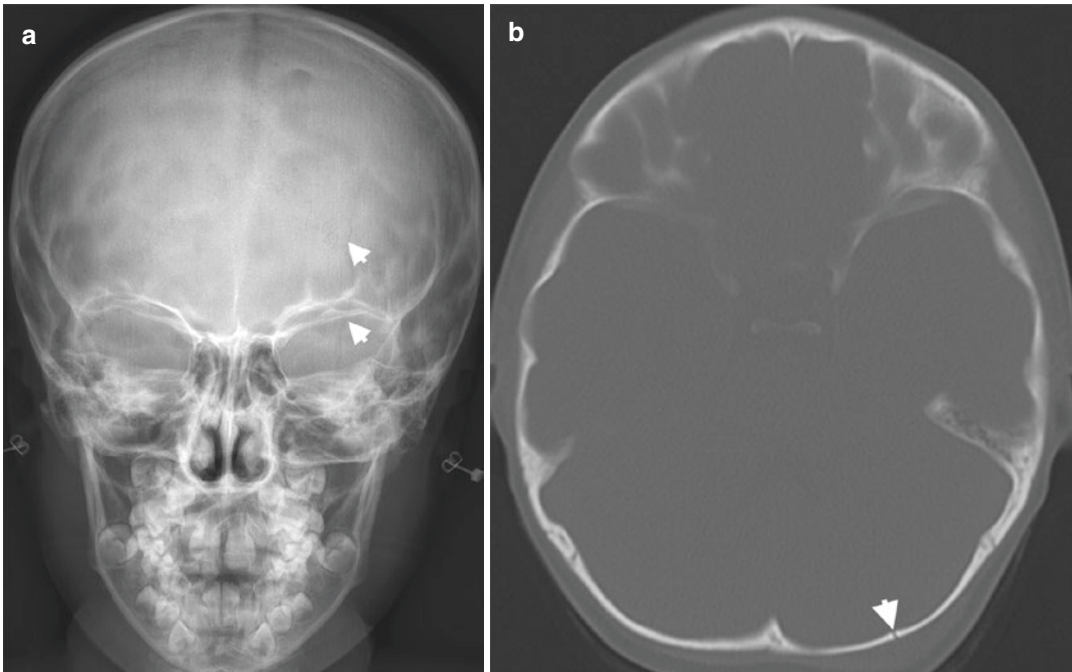

Fig. 3 Linear fracture in occipital bone. (**a**) A-P view of skull radiograph of a 6-year-old female patient presented to emergency department after fall reveals a unilateral linear vertically extending radiolucency (arrowheads) in left side of occipital bone. (**b**) Axial CT image confirms the presence of linear fracture (arrowhead) in the occipital bone
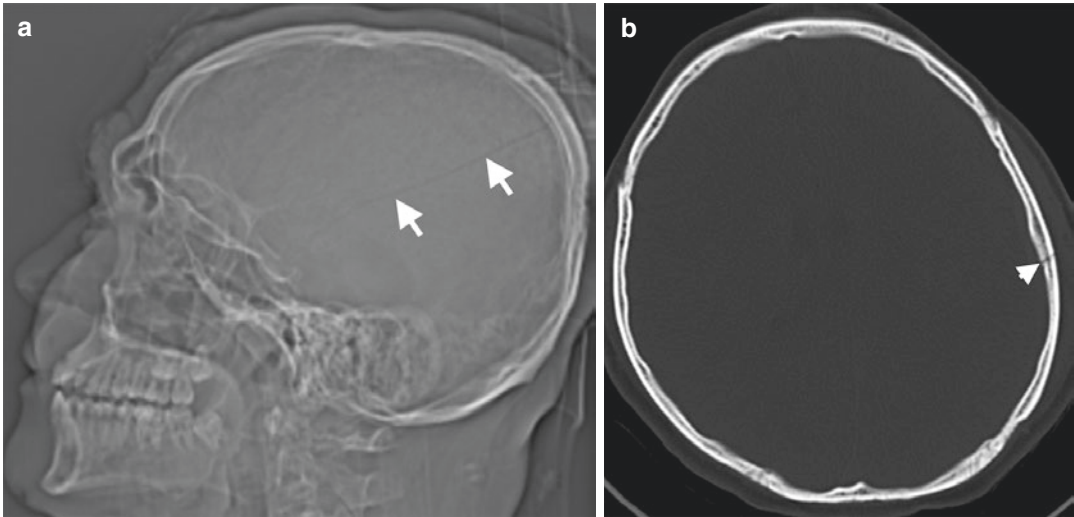
Fig. 4 Linear fracture in parietal bone. (**a**) Scenogram image reveals fracture as radiolucent line extending through temporal and parietal bones (short arrows). (**b**) Axial CT image of the same patient demonstrates linear fracture (arrowhead) in parietal bone
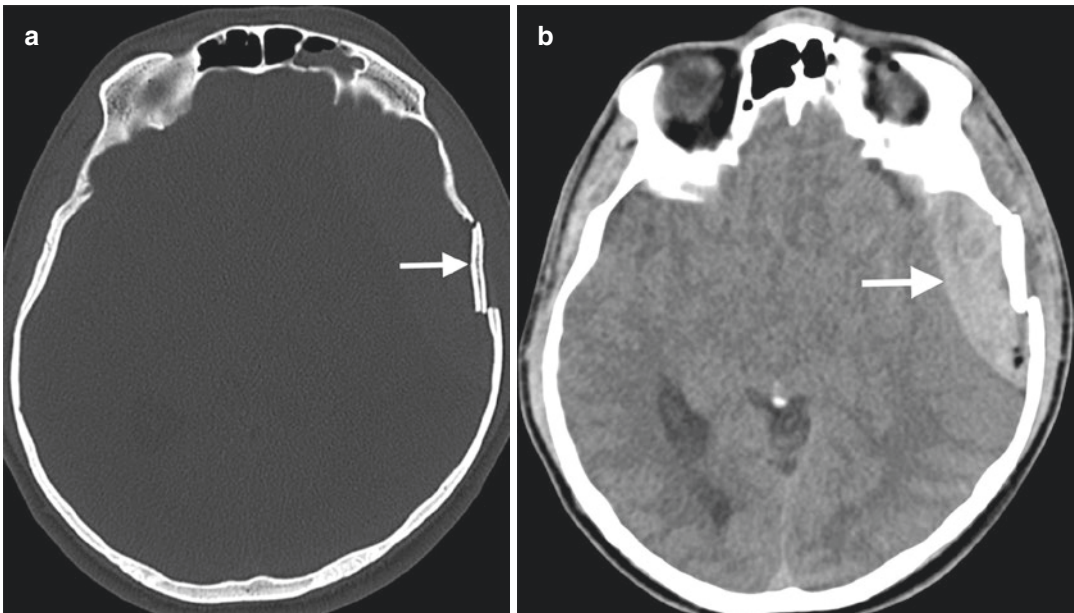

Fig. 5 Depressed fracture in temporal bone. (**a**) Axial CT image on bone window shows a depressed temporal bone fracture characterized by displacement of fracture fragment (arrow) from the uninvolved temporal bone part. (**b**) Axial CT image on soft-tissue window demonstrates accompanying epidural hemorrhage (arrow) resulting from depressed fracture
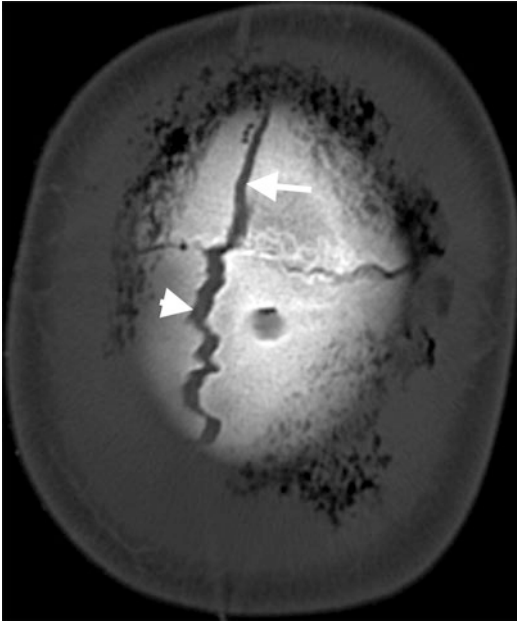
Fig. 6 Cranial fracture with diastasis of neighboring suture. Axial CT image shows linear fracture (arrow) in the vertex that extends from the frontal bone and results in diastasis of the sagittal suture (arrowhead)

and fractures on plain radiographs and CT is crucial for avoiding misdiagnosis (Table 1). Non-depressed fractures in cranial bones appear as sharp lucencies with non-sclerotic edges, while accessory sutures present as radiolucent lines with irregular interdigitations, also known as zigzag pattern, and sclerotic borders (Fig. 9). Cranial fractures usually manifest with adjacent soft-tissue swelling indicating a scalp hemorrhage or edema. Widening of fracture line as it extends to the suture or synchondrosis is another helpful feature in depicting fracture. Cranial fractures resulting from high-impact trauma can cross suture lines in contrast to accessory sutures, which join with the major suture (Sanchez et al. 2010). Accessory sutures often present bilaterally and fairly symmetric in appearance, especially in the parietal bones (Weir et al. 2006). Skull fractures caused by high-energy trauma may also occur bilaterally; however, bilateral skull fractures almost always appear as comminuted and depressed fractures with marked asymmetry due
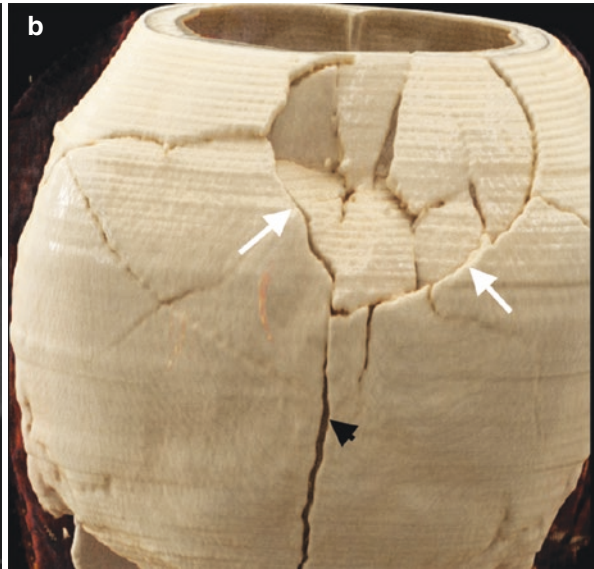
Fig. 7 Comminuted fracture in cranium. (**a**) Axial CT image of a 58-year-old male patient reveals comminuted fracture (arrow) of occipital bone, and (**b**) CR image shows comminuted fracture (arrows) in the occipitopari-etal bone. A linear fracture (black arrowhead) is radiating from the comminuted fracture extending through the occipital bone

Fig. 8 Growing fracture. (**a**) CR image of a 1-year-old child shows a fracture in right frontal bone with separated bony edges (arrow). (**b**) Axial image of follow-up CT performed 1-month after initial CT demonstrates a low attenuated fluid collection (arrow) representing leptomeningeal cyst herniating from the scalp through fracture defect (arrowhead). (**c**) CR image of follow-up CT reveals increased distance between the bony edges of right frontal fracture (long arrow and arrowhead) with accompanying left frontal fracture (short arrow)

to the underlying high-energy impact (Sanchez et al. 2010). Vascular or peripheral nerve grooves should also be distinguished from linear fractures. Well-corticated margins, decreased sharpness, and asymmetric extension of the grooves created by neurovascular structures may be helpful to distinguish vascular grooves in cranial bones from linear fractures.

Linear, depressed, and comminuted fractures of cranium can cause extra-axial hemorrhage when they cross vessel grooves such as those encompassing the middle meningeal artery or dural venous sinuses. Venous injuries may also result in thrombosis of the veins leading to venous infarction. Parietal bone fractures may cause injuries in the parietal branch of middle

Table 1 Imaging features for differentiation between cranial fracture and suture (Sanchez et al. 2010)

Cranial fracture	Cranial suture
Linear radiolucency with sharp edges	Extends with zigzag pattern
Non-sclerotic edges	Sclerotic edges
Often associated with diastasis of suture	No associated diastasis
Widens as approaching to suture	Joins adjacent suture
May cross adjacent suture lines	No crossing suture lines
Usually unilateral, asymmetric if bilateral	Often bilateral, fairly symmetric (accessory sutures)
Soft-tissue swelling (subgaleal hematoma, scalp hematoma)	No soft-tissue swelling
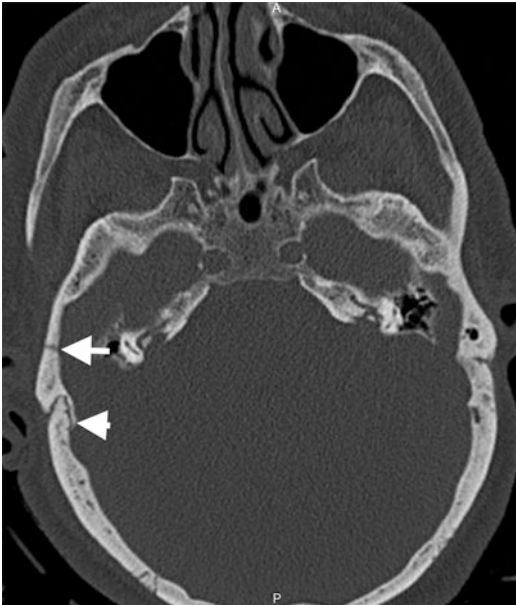
Fig. 9 Cranial fracture and suture. Axial CT image at bone window shows a linear fracture in right temporal bone with sharp and non-sclerotic edges (arrow) nearby occipitomastoid suture, which manifests with interdigitating appearance and sclerotic edges (arrowhead)

meningeal artery and veins. Frontal branch of the middle meningeal artery may also be injured since this vessel traverses the underlying anterior part of the parietal bone superior to the pterion where four cranial bones (frontal, parietal, sphenoid, and temporal bones) articulate. Parietal bone fractures may damage the parietal branch of superficial temporal artery and posterior auricular artery in the scalp. Occipital bone fractures may cause injury to the transverse sinus, confluence of sinuses, and caudal portion of superior sagittal sinus (Fig. 10).

Dural tears and arachnoid tears may occur as an immediate consequence of calvarial fractures. Dural tears can result in subdural hygroma and CSF leakage, which may present as rhinorrhea or otorrhea depending on the location of the dural tear. Arachnoid tears may also cause subdural hygroma formation (Hijaz et al. 2011).

3 Temporal Bone

3.1 Anatomy

Temporal bone forms inferolateral aspect of lateral calvarial vault and contributes to the skull base skeleton. Temporal bone articulates with occipital bone posteriorly, parietal bone superiorly, and greater wing of the sphenoid bone anteriorly. Temporal bone contains five distinct portions as squamous, mastoid, petrous, tympanic part, and styloid process. Squamous part of the temporal bone is the thinnest and weakest part of calvarial bones that contains the posterior zygomatic process and anterior part of the mandibular fossa. Mastoid portion includes mastoid air cells and connects to epitympanum via aditus ad antrum. Skull base part of temporal bone constitutes petrous and mastoid portions. Tympanic part divides into epitympanum, mesotympanum, and hypotympanum. Mesotympanum encloses ossicles named as malleus, incus, and stapes, which articulate with each other via incudomalleal and incudostapedial joints. Tympanic portion is separated from external auditory canal (EAC) by tympanic membrane. The boundaries of middle ear consist of tympanic membrane laterally, inner ear medially, tegmen tympani superiorly,
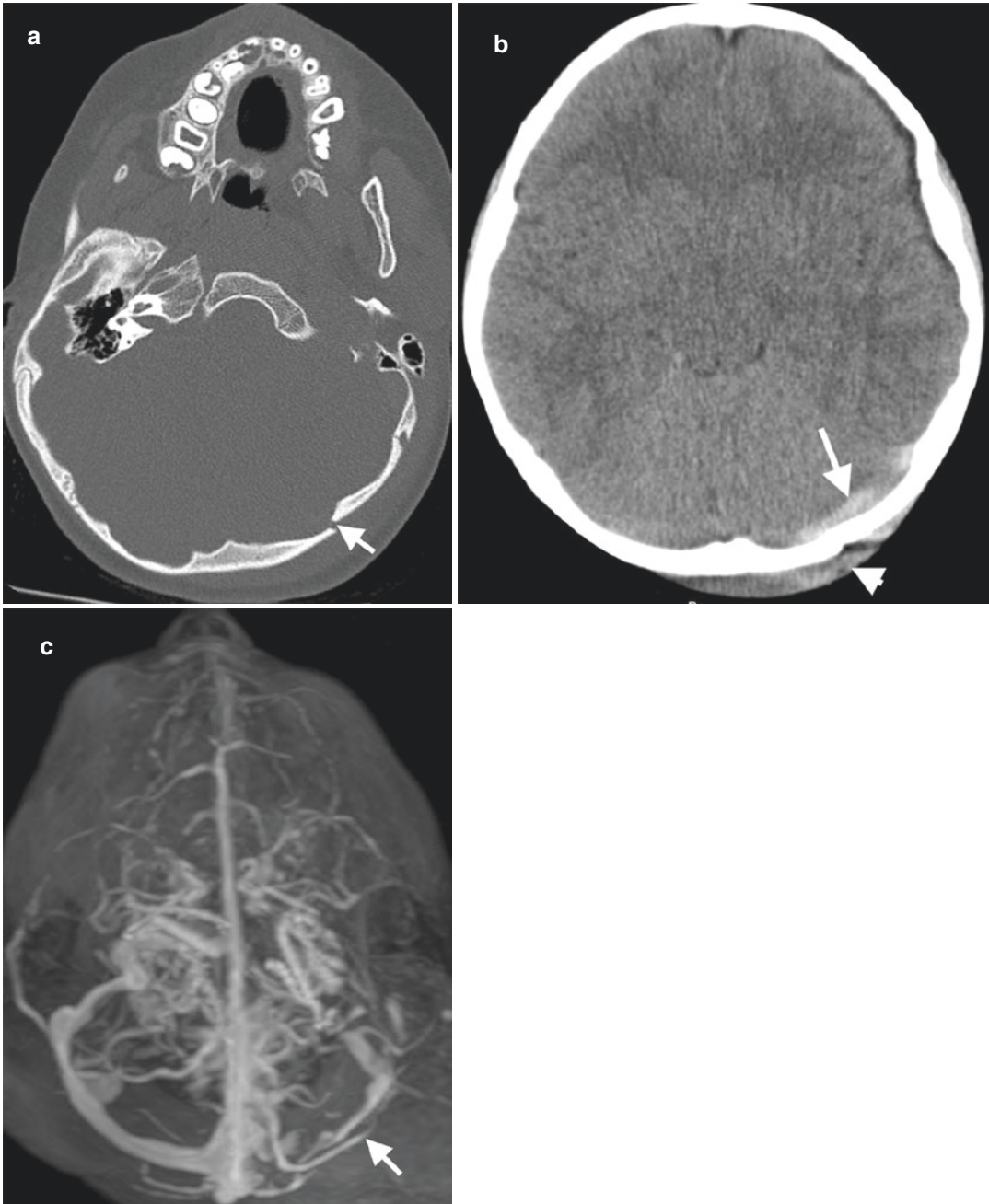
Fig. 10 Cranial fracture resulting in venous sinus thrombosis. (**a**) Axial CT image of a 5-year-old boy demonstrates a depressed fracture (arrow) in left occiput. (**b**) Axial CT image at soft-tissue window shows increased density in left transverse sinus trajectory (arrow) suggestive of sinus thrombosis. A scalp hematoma (arrowhead) can be seen as an accompanying imaging feature at the fracture site. (**c**) MR venography reveals thrombosis of the left transverse sinus with loss of blood flow signal in the sinus (arrow)

and jugular wall inferiorly. Petrous portion of the temporal bone contains inner ear that is comprised of cochlea, vestibule, and semicircular canals within the osseous labyrinth. Osseous labyrinth is surrounded by the otic capsule, which is the densest part of the temporal bone. Carotid
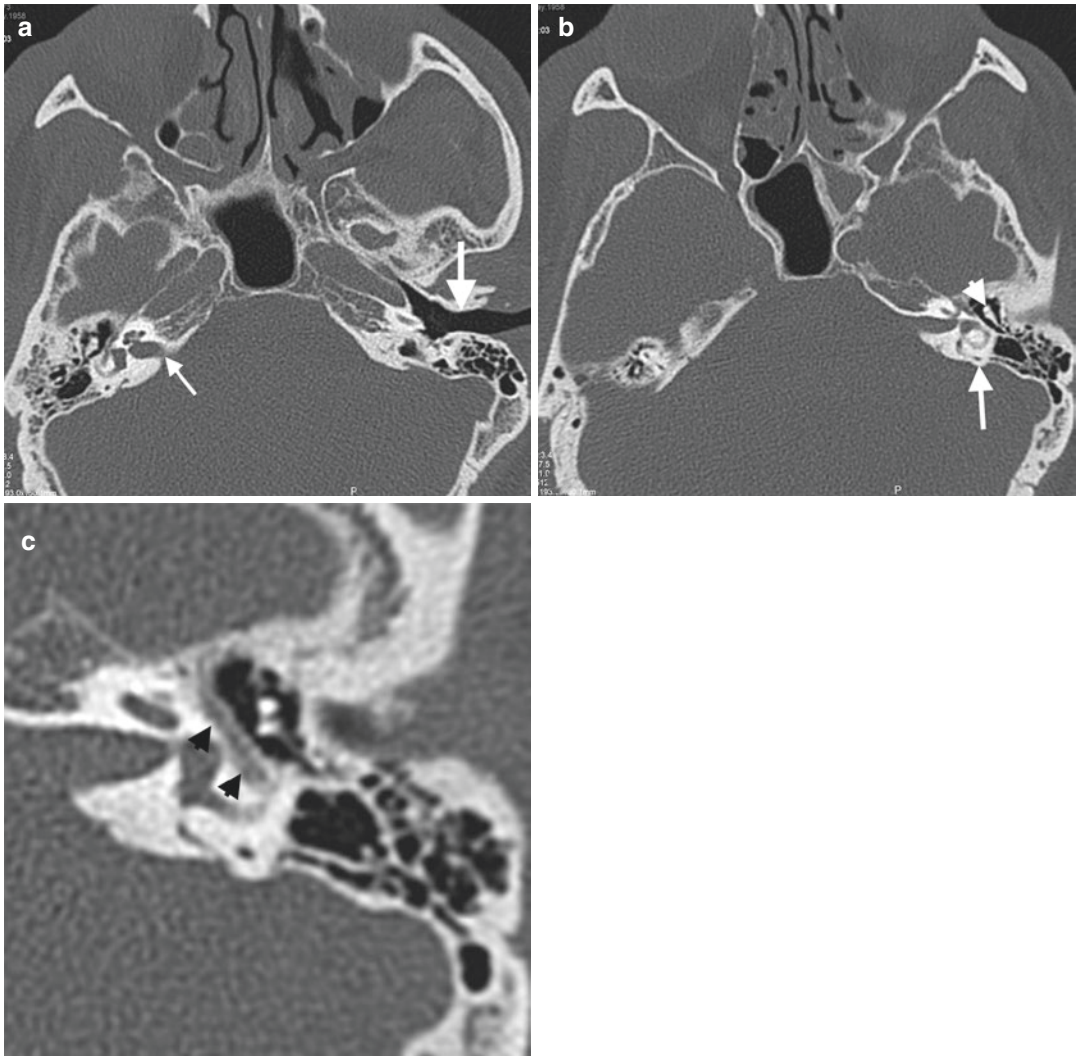
Fig. 11 Temporal bone anatomy. (**a**) Axial CT image at bone window demonstrates left EAC (thick arrow) and right inner ear (thin arrow). (**b**) Ice cream appearance of incudomalleal complex (arrowhead) in tympanic portion and otic capsule (arrow) in the left temporal bone. Ice cream scoop and cone represent malleolar head and short process of the incus, respectively. (**c**) Axial CT image shows tympanic segment of facial canal (black arrowheads) coursing medial to the left middle air

canal is located posteriorly to the petrous ridge of temporal bone.

Facial nerve traverses the temporal bone from its inferolateral portion to the superomedial portion. Integrity of facial nerve can be assessed on CT by visualizing the facial canal. Facial nerve has different portions in the temporal bone called according to temporal bone portions as labyrinthine, mastoid, and tympanic segments (Fig. 11) (Juliano et al. 2013).

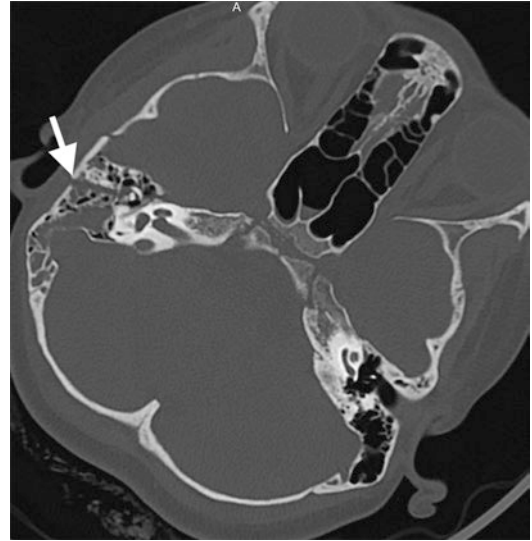## 3.2 Fractures

Temporal bone fractures constitute 18–22% of skull fractures occurred secondary to major head traumas (Cannon and Jahrsdoerfer 1983). A substantial force (at least 1875 lb) is required for fracture of the temporal bone that indicates high probability of concomitant cranial bone fractures (Tress et al. 2014). Clinical signs and symptoms of temporal bone fractures include hemorrhagic
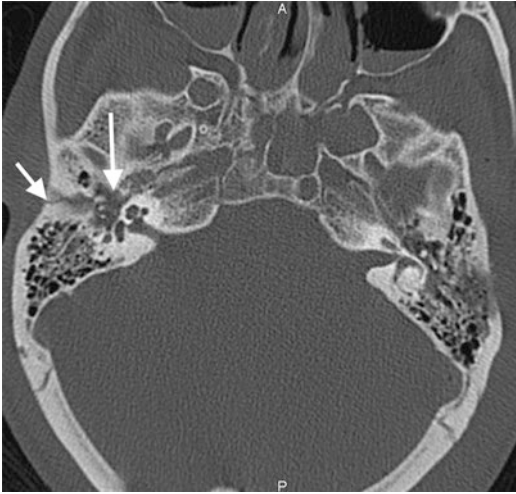
Fig. 12 Hemotympanum. Axial head CT image demonstrates a linear fracture (short arrow) in the right temporal bone with hemotympanum (long arrow)

Fig. 13 Longitudinal temporal bone fracture. Axial CT image of a 10-year-old girl after MVA reveals a longitudinal fracture (arrow) extending parallel to the orientation of petrous ridge of right temporal bone with separated fracture fragments

otorrhea, tympanic membrane perforation, vertigo, hearing loss, and facial nerve palsy (Juliano et al. 2013). Fractures traversing the mastoid portion can result in "Battle sign" (postauricular ecchymosis) due to traumatic rupture of the mastoid emissary vein (Watanabe and Kida 2012). CT examination in temporal bone fractures should be performed with slice thickness ≤1 mm and field of view (FOV) <10 cm. Additional evaluation with MPR images including coronal plane, Stenvers view (oblique coronal orientation parallel to the petrous ridge), and Pöschl view (oblique coronal orientation perpendicular to the petrous ridge) may be helpful for acquisition of CT images parallel to orientation of ossicles and facial nerve. As head trauma is often assessed with head CT, it may be helpful to know imaging findings of temporal bone fractures on head CT. Head CT findings that may be associated with temporal bone fractures include EAC, tympanic cavity and mastoid air cell opacification, air within the temporomandibular joint, intracranial air adjacent to the temporal bone, and pneumolabyrinth (Fig. 12) (Kennedy et al. 2014).

Temporal bone fractures are traditionally classified as longitudinal, transverse, or mixed according to their orientation relative to the long axis of the petrous pyramid. Mixed fractures

refer to fracture types occurring in both transverse and longitudinal planes. Longitudinal fractures constitute 50–80% of temporal bone fractures and extend parallel to the long axis of the petrous pyramid (Fig. 13) (Little and Kesser 2006; Nosan et al. 1997; Ishman and Friedland 2004). This fracture type usually begins from squamosal portion of temporal bone, extends along the posterosuperior border of the EAC bony margin, and exits in middle cranial fossa anterior to the labyrinth (Juliano et al. 2013). Longitudinal fractures may also extend into jugular fossa, carotid canal, and facial canal. Ossicular injuries and tympanic membrane perforation are usually associated with longitudinal fractures. Ossicular dislocation and hemotympanum occur in 32% and 90% of patients, respectively (Meriot et al. 1997). Transverse fractures are oriented perpendicular to the axis of the petrous pyramid and traverse the temporal bone in superoinferior orientation. Transverse fractures usually result from fronto-occipital impacts and may occur laterally through the cochlea or vestibule or medially through the internal acoustic canal (IAC) and petrous pyramid (Collins et al. 2012). Although

transverse fractures occur at a frequency of one third to one fifth to that of longitudinal fractures, the probability of facial nerve injury, which can occur in 7% of patients in this type of injury, increases its clinical importance (Brodie and Thompson 1997). Cochlear nerve injury can also occur secondary to transverse fractures that involve the IAC apex. Oblique fractures that refer to coexistence of both longitudinal and transverse fractures are found approximately 10–75% of patients in previous studies (Dahiya et al. 1999; Ghorayeb and Yeakley 1992; Juliano et al. 2013; Little and Kesser 2006; Nosan et al. 1997; Ishman and Friedland 2004).

Although traditional classification depending on fracture orientation in temporal bone as longitudinal, transverse, or mixed type is widely used, it was shown that there is no satisfying correlation between this classification system with clinical outcomes and further complications. Thereby, several investigators recommended different classification systems that classify temporal bone fractures according to the involved portions of temporal bone such as petrous and non-petrous types or otic capsule-spared or violated type. Petrous fractures involve the petrous apex and otic capsule, while non-petrous fractures involve the middle ear and mastoid portion (Ishman and Friedland 2004). Complications of petrous fracture group include facial nerve injury, CSF leak, and sensorineural hearing loss. Involvement of ossicular chain in non-petrous group causes increased incidence of conductive hearing loss (CHL). Temporal bone fracture classification regarding involvement of otic capsule is mainly focused on clinical outcome. The most common injury type according to this classification system is otic capsule-sparing form that occurs in 94–97% of patients resulting from temporoparietal blow. This form causes CHL due to ossicular injury. The other form, otic capsule-violating fracture, occurs in 3–6% of cases and usually results from occipital blow. This type has a high association with facial nerve injury (30–50%), sensorineural hearing loss, and CSF fistula (Juliano et al. 2013). High spatial resolution CT examinations with MPR images can demonstrate the involvement of vestibule, vestibular aque-

duct, semicircular canals, cochlea, and/or facial canal in otic capsule-violating fractures (Juliano et al. 2013).

Temporal bone fractures may cause various complications including tympanic membrane perforation, ossicular chain derangement, injury of vestibulocochlear apparatus, facial nerve and vessels, CSF leakage, and meningitis. Traumatic CHL, being the most common complication with an occurrence rate of 24–81% following temporal bone trauma, can result from massive hemorrhage in EAC, tympanic membrane perforation, hemotympanum, and derangement of the ossicular chain (Kennedy et al. 2014; Dahiya et al. 1999; Brodie and Thompson 1997; Nosan et al. 1997; Rafferty et al. 2006). Ossicular injuries include fractures of the malleus, incus, or stapes, dislocation or subluxation of incudomalleolar, incudostapedial, and/or stapediovestibular joint, and disruption of the suspensory ligaments of the ossicles (Meriot et al. 1997; Yetiser et al. 2008). Ossicular injuries may be caused by direct traumatic forces or associated with simultaneous contraction of the stapedius and tensor tympani muscles after trauma (Basson and van Lierop 2009; Swartz 2001). Longitudinal fractures that extend into the middle ear more often cause ossicular injury compared to transverse fractures (Kennedy et al. 2014). The most frequently injured ossicle in the middle ear is incus, which has the weakest ligamentous support in the tympanic cavity. Mild separation of ossicles in ossicular joints is named as subluxation, while frank separation is called as dislocation. Total incus dislocation may also occur and presents on CT as absence of incus in its normal position and displacement within the incuidal fossa or not found at all (Swartz 2001). Incudomalleolar joint normally appears as an ice cream configuration on axial CT sections. In this configuration, the ice cream scoop and cone represent malleolar head and short process of incus, respectively (Fig. 11b). Any widening of incudomalleolar joint space or any offset of the malleus head relative to the incus indicate incudomalleolar subluxation since interface between these ossicles should be very thin (Fig. 14) (Collins et al. 2012). Incudomalleolar dislocation is characterized by
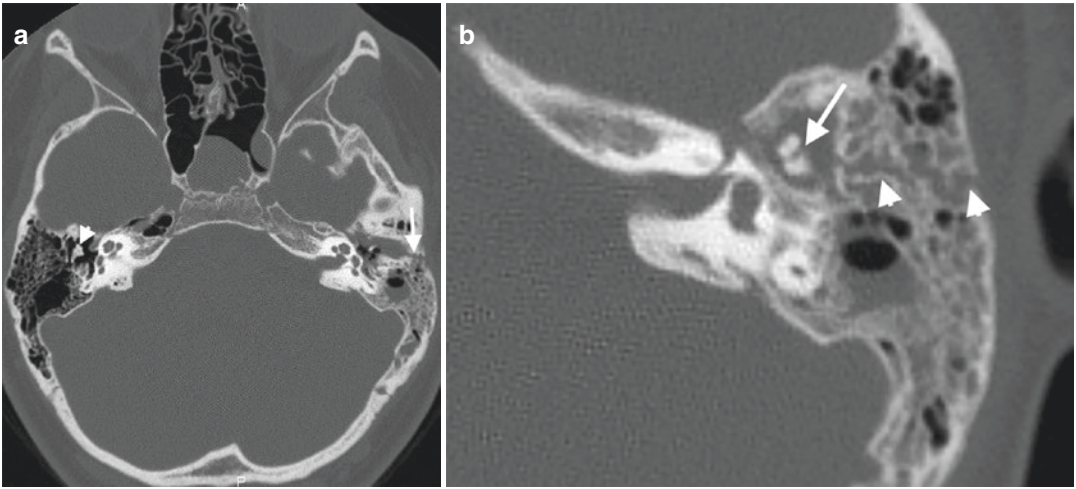
Fig. 14 Incudomalleolar subluxation in a 17-year-old man after MVA. (**a**) Axial CT image shows a longitudinal fracture (arrow) in the left temporal bone. Normal ice cream cone appearance (arrowhead) is shown on the right temporal bone. (**b**) Axial CT image of the same patient demonstrates longitudinal fracture (arrowheads) associated with widening of incudomalleolar joint space (arrow)
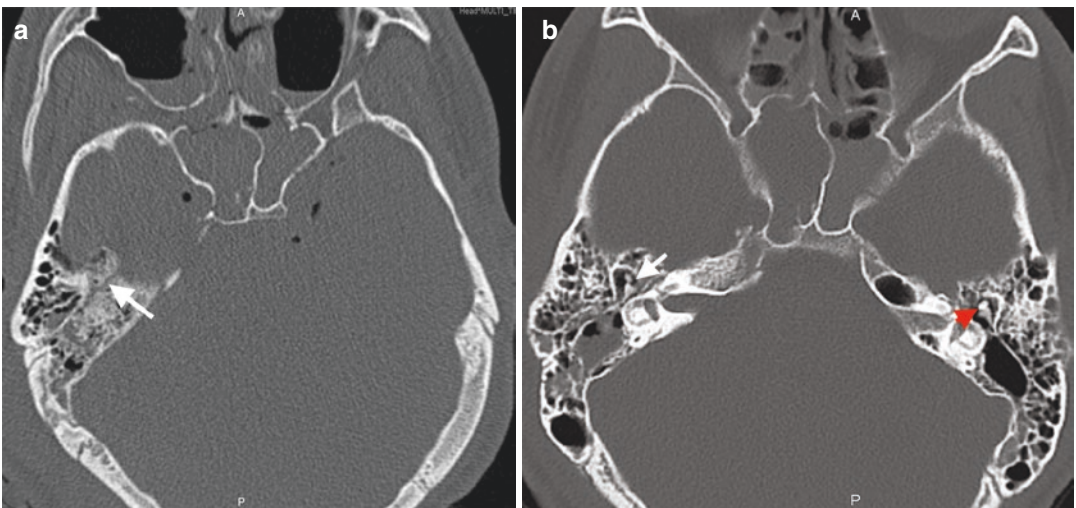
Fig. 15 Incudomalleolar dislocation. (**a**) Axial CT image demonstrates right temporal bone fracture (arrow) with oblique orientation. (**b**) Ice cream cone appearance (red arrowhead) represents normal incudomalleolar joint alignment in the left temporal bone. Incudomalleolar dislocation presents with displacement of head of the malleus (scoop of ice cream) from the body and short process of the incus (cone) (arrow)

falling off ice cream scoop from cone (Fig. 15). The presence of both incus and malleus in the same image on a coronal scan is abnormal and suggestive of incudomalleolar dislocation (Lourenco et al. 1995). Stapediovestibular joint disruption rarely occurs and is being reported in 3% of cases due to the strong attachment of annular ligament of this joint (Meriot et al. 1997). Incudostapedial joint injury may be difficult to assess on CT compared to incudomalleolar joint in the setting of hemotympanum. It is important to define the joint injuries as mild or severe on imaging studies since minor ossicular derangements can be managed conservatively,

while frank dislocations require surgical management to prevent CHL.

Fractures of ossicles may be encountered in 2–11% of patients with temporal bone trauma (Nosan et al. 1997; Meriot et al. 1997). Ossicular fractures appear as a lucent line through the ossicles and/or displaced bone fragment within the tympanic cavity on axial CT images. Vertical position of the manubrium and long process of the incus make the fractures of these incus components more easily detectable on coronal CT images. The fractures of the stapes footplate may be associated with perilymphatic fistula (PLF) (Kennedy et al. 2014).

Sensorineural hearing loss (SNHL) may result from injuries of otic capsule or cochlear nerve. The imaging findings of SNHL and vertigo include injury of the bony labyrinth, injury of the IAC, brainstem/nerve root zone, and pneumolabyrinth. Isolated intralabyrinthine hemorrhage in the absence of fracture may also cause SNHL. Although transverse fractures were reported to be more commonly associated with SNHL, new classification schemes regarding involvement of petrous bone or otic capsule were found to be more correlated with occurrence of SNHL. Otic capsule-violating fractures occur in 2–6% of temporal bone fractures, and SNHL invariably occurs in these fractures (Dahiya et al. 1999; Brodie and Thompson 1997; Little and Kesser 2006). Temporal bone fractures traversing cochlea, vestibule, or semicircular canal on CT strongly suggest otic capsule injury (Fig. 16). In the absence of fracture, hemorrhage within the otic capsule that may not be shown on CT can be depicted on MRI with high signal intensity on T1-weighted images.

Another potential complication of temporal bone fracture is vertigo, which may be caused by violation of vestibule, semicircular canals, vestibular aqueduct, or vestibular nerve. Vertigo may also be caused by labyrinthine concussion, shearing of nerve root entry zone, or brainstem injury (Kennedy et al. 2014). Cochlear concussion refers to injury or disruption of membranous labyrinth due to the traumatic force (Collins et al. 2012). CT images reformatted in the Stenvers and Pöschl views are most beneficial to demonstrate superior and posterior semicircular canals due to the compatibility of orientation of these views with alignment of semicircular canals.

PLF refers to abnormal connection between perilymph and middle ear cavity and should be suspected when CT shows fracture/dislocation of the stapes footplate oval window and the fracture traverses the round or oval window. Secondary signs of PLF include unexplained middle ear fluid and pneumolabyrinth on CT.

CSF leak may be encountered in 13–45% of patients with temporal bone fractures, which increases the risk of meningitis (Brodie and Thompson 1997; Dahiya et al. 1999; Nosan et al. 1997; Rafferty et al. 2006). CSF leaks after temporal bone fractures may present as otorrhea and otorhinorrhea in the setting of tympanic membrane disruption and intact tympanic membrane with Eustachian tube drainage, respectively (Prosser et al. 2011). The determination of CSF leak site on CT or MRI is crucial in surgical management of these patients (Fig. 16). The assessment of CSF leaks on CT necessitates scrutinizing the integrity and position of the tegmen tympani on coronal and sagittal images in terms of bone defects, fracture fragments, and associated encephalocele (Fig. 17). The sensitivity of CT was reported as 92% for detection of the site of bone defect, which may cause dural tear and CSF leak (Lloyd et al. 2008). CSF leak and accompanying multiple osseous defects may necessitate cisternography, which may be performed with CT and MRI to determine the source of active leak. CT cisternography technique should begin with precontrast thin-section CT images to determine the baseline density in sinuses formed by blood or high protein content. This should be followed by a scan performed after introducing intrathecal iodinated contrast agent via lumbar puncture in head-down position with provocative maneuvers. Post-contrast images should be obtained in both prone coronal and supine axial positions. CSF leaks appear as increased density and pooling of contrast in the sinuses and mastoids (Baugnon and Hudgins 2014). MR cisternography technique includes heavily T2-weighted, fat-saturated spin-echo,
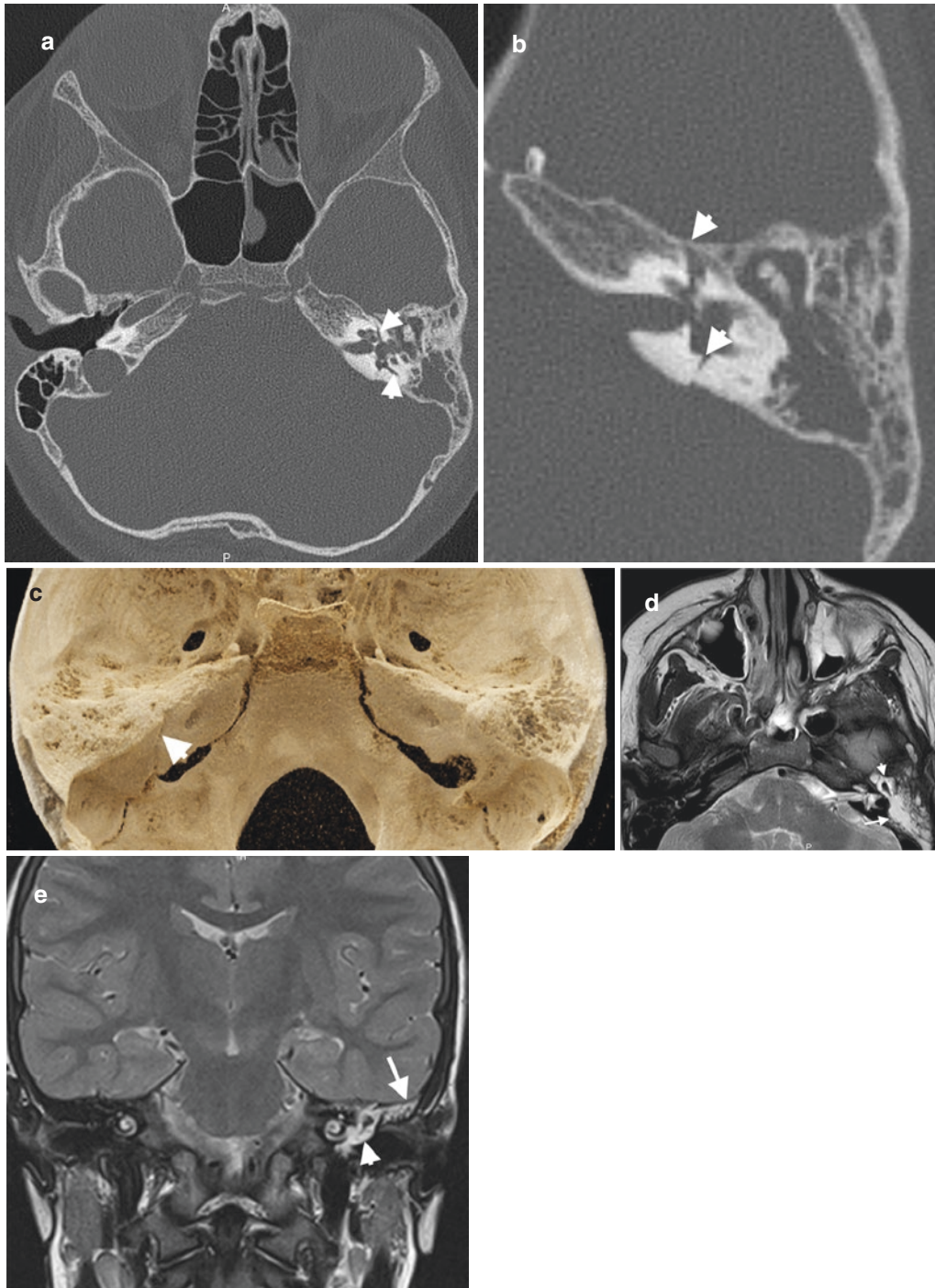
Fig. 16 Otic capsule-violating temporal bone fracture in an 8-year-old male patient with a history of MVA. (**a**) Axial CT image demonstrates a horizontally oriented fracture violating otic capsule (arrowheads) in the left temporal bone. (**b**) Enlarged axial view shows hemotympanum and hemomastoideum with horizontal fracture (arrowheads) traversing petrous portion of the temporal bone with anteroposterior orientation. (**c**) CR image demonstrates the horizontal fracture as a subtle linear fracture line (arrowhead) traversing petrous portion of left temporal bone. Axial (**d**) and coronal (**e**) T2-weighted MR images obtained 15 days after trauma reveal hyperintense fluid in the left mastoid cells (arrows) and tympanic cavity (arrowheads) consistent with CSF leakage
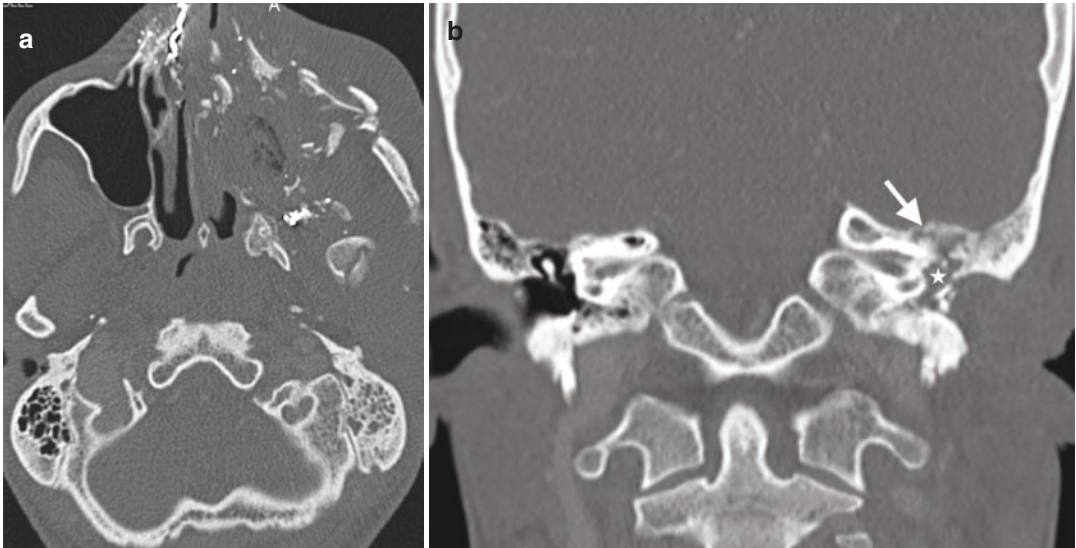
Fig. 17 Tegmen tympani fracture. (**a**) Axial CT image of a 24-year-old man with a history of gunshot injury reveals multiple maxillofacial bone fractures in right side of the face. (**b**) Coronal CT image demonstrates displaced tegmen tympani fracture (arrow) and hemotympanum (*)

high-resolution 3D GRE sequences in addition to precontrast and post-contrast T1-weighted images. CSF leaks present as continuous column of T2 hyperintense material extending from the subarachnoid space. Localization and size of encephaloceles may be better evaluated on T2-weighted MR images. Dural enhancement adjacent to suspected fracture site may indicate dural tear and subsequent CSF leak.

Facial nerve injury may be encountered in 5–10% of patients with temporal bone fractures (Brodie and Thompson 1997; Yetiser et al. 2008). This injury occurs in 48% of otic capsule-violating and 6% of otic capsule-sparing fractures (Brodie and Thompson 1997). Displacement or violation of facial canal boundaries in temporal bone on CT is suggestive of facial nerve injury (Fig. 18). Most common injury site of facial nerve is geniculate ganglion, followed by the second genu of the nerve, and the tympanic and the mastoid portions. Distal facial nerve injury may also occur in styloid process fractures (Collins et al. 2012). Signs and symptoms of facial nerve injury may exist even in the absence of facial canal injury. In this setting, MRI may be helpful, which can demonstrate T1 hyperintensity in the

facial canal suggestive of perineural hematoma. Enhancement of cisternal, canalicular, or labyrinthine segments of facial nerve is always pathologic, while geniculate ganglion and tympanic and mastoid segments may enhance normally after intravenous gadolinium administration (Collins et al. 2012).

Vascular complications of temporal bone fracture include injury to the internal carotid artery (ICA) and jugular vein. As ICA passes through the petrous portion of the temporal bone, the risk of ICA injury increases in temporal bone fractures, especially traversing the petrous portion (Fig. 19). ICA complications after temporal bone fractures include dissection, transection, pseudoaneurysm formation, occlusion, and arteriovenous fistula. The distal transverse and sigmoid sinuses may also be injured in fractures extending into the jugular foramen. Temporal bone CT examinations should be reviewed with soft-tissue algorithms for the depiction of venous sinus thrombosis that appears as hyperdense clot or air within the vein lumen. CT and MR venography can be preferred to assess venous injury more comprehensively (Kennedy et al. 2014) (Fig. 18).
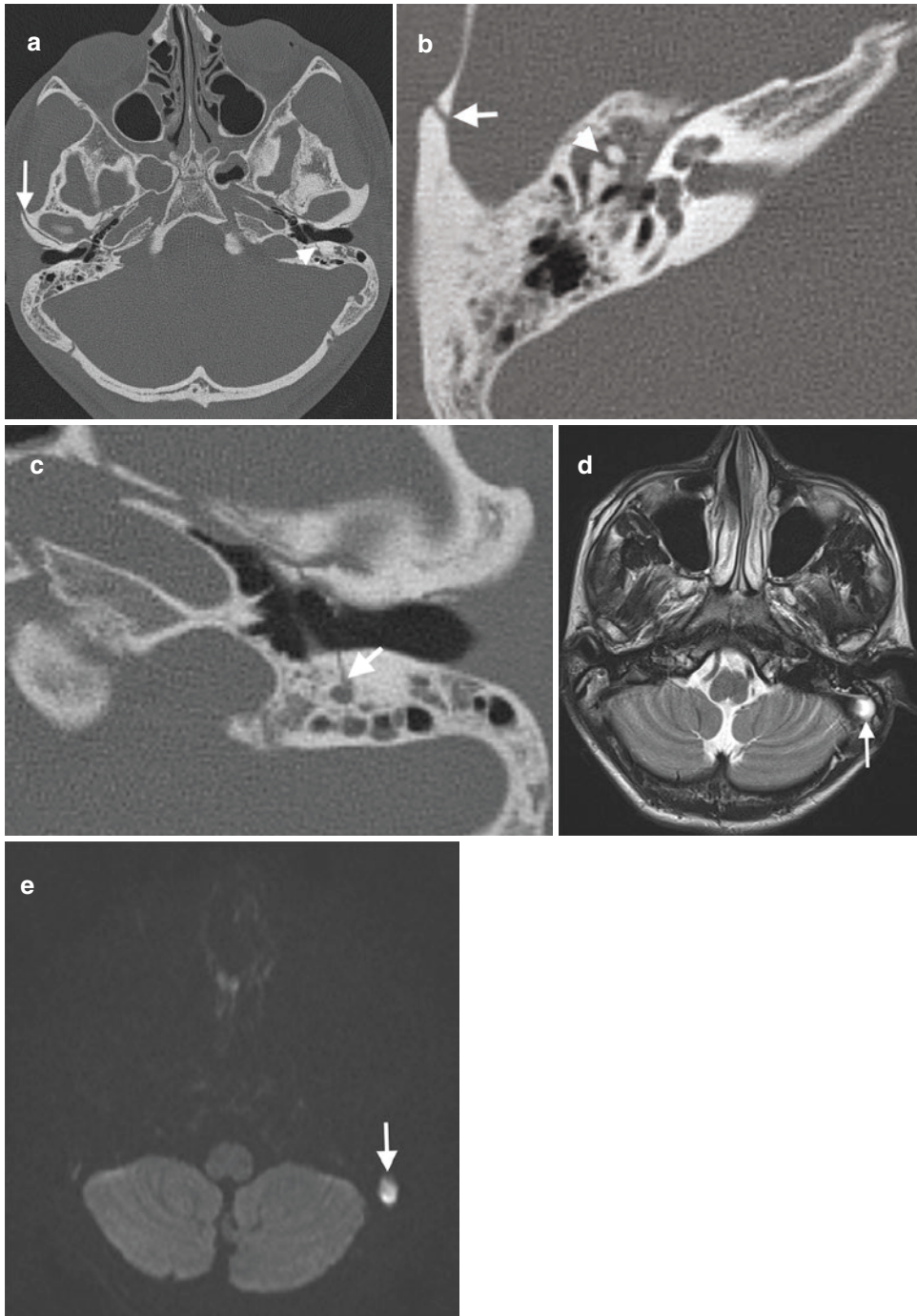
Fig. 18 Bilateral temporal bone fractures in a 16-year-old man with a history of a wall fell on him 10 days ago. (**a**) Axial CT image demonstrates a linear fracture (arrow) oriented longitudinally through anterior wall of the right EAC and horizontally oriented fracture extending through left otic capsule (arrowhead). (**b**) Enlarged view of axial CT image of the same patient reveals fracture in the squamous part of the right temporal bone and dislocation of the incudomalleolar joint (arrowhead). (**c**) Enlarged view of left temporal bone axial CT image depicts extension of fracture through the anterior wall of left facial canal (arrow). (**d**) Axial T2-weighted MR image shows loss of signal void (arrow) in left sigmoid sinus adjacent to the left temporal bone suggestive of sigmoid sinus thrombosis. (**e**) Axial DWI reveals increased signal intensity due to thrombosis of sigmoid sinus
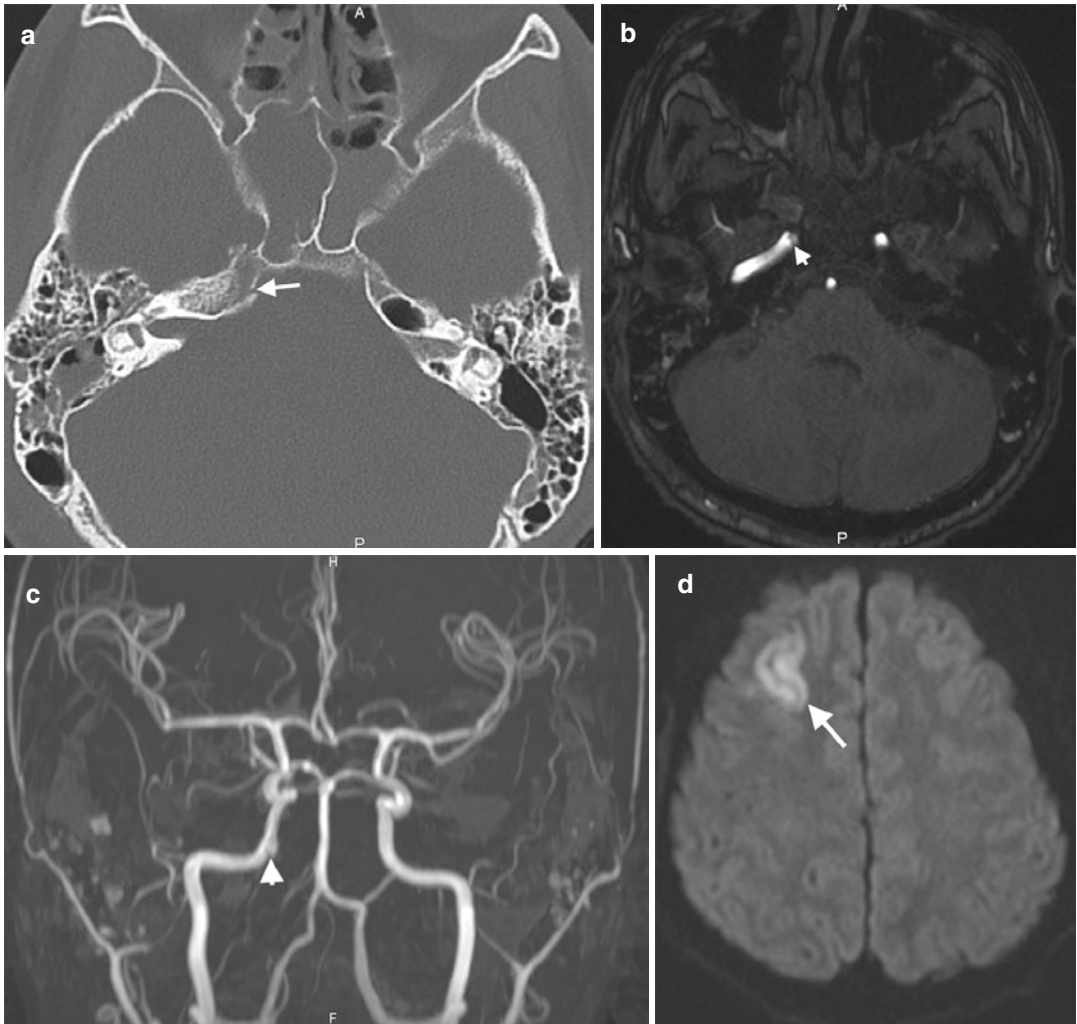
Fig. 19 Temporal bone fracture with carotid artery injury in a 17-year-old man with a history of fall. (**a**) Axial CT image reveals right petrosal ridge fracture (arrow) involving right carotid artery. Axial 2D (**b**) and 3D (**c**) TOF MR angiography images show linear hypointense filling defect (arrowheads) representing dissection at the junction of petrous and cavernous segments of the right ICA. (**d**) DWI of the same patient demonstrates increased signal intensity (arrow) secondary to acute ischemia in the right frontal lobe
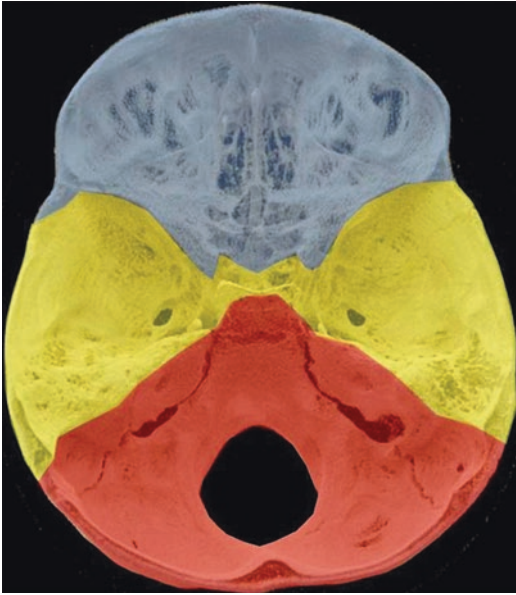
4 Skull Base

4.1 Anatomy

The skull base forms the floor of the intracranial compartment and separates intracranial and extracranial compartments. Skull base is constituted from three components including anterior skull base (ASB), middle skull base (MSB), and posterior skull base (PSB) and made up of seven bones as paired frontal and temporal bones with the unpaired ethmoid, sphenoid, and occipital bones. ASB, MSB, and PSB form the floor of the anterior cranial fossa, middle cranial fossa, and posterior cranial fossa, respectively (Fig. 20). ASB is formed by orbital plates of frontal bone and posterior table of frontal sinus and separates anterior fossa structures from the orbits and sinonasal cavity. Cribriform plate (CP) and roof of the ethmoid sinuses form the floor of ASB. ASB

Fig. 20 Skull base anatomy. Colored axial CR image of SB demonstrates ASB with blue, MSB with yellow, and PSB with red colors

is separated from MSB by the lesser wing of sphenoid bone. Bilateral fovea ethmoidalis as medial extensions of orbital plates is located in the inferomedial wall of the ASB superolaterally to CP. Connection between CP and fovea ethmoidalis is maintained by lateral lamellae (Fig. 21a) (Manson et al. 2009; Madhusudan et al. 2006). MSB is a critical anatomic structure as it contains several foramina that transmit vessels and nerves between intracranial and extracranial compartments. MSB is mainly constituted from sphenoid bone and temporal bone portion anterior to the petrous ridge (Figs. 20 and 21b). Sphenoid bone is a bat-like bone composed of a central body, greater and lesser wings laterally, and pterygoid processes inferiorly. MSB is formed by central skull base (CSB) and lateral skull base. CSB is composed of sphenoid bone and anteromedial aspect of the petrous part of temporal bone (Baugnon and Hudgins 2014). PSB is formed by the occipital bone and posterior aspect of the petrous part of the temporal bone. Occipital condyles and mastoid portion of the temporal bone form the inferior boundaries of PSB (Figs. 20 and 21c). In the midline, basis of the PSB is formed

by clivus, which is constituted from basisphenoid and basioccipitus in sphenoid and occipital bones, respectively. Major anatomical landmarks in PSB are foramen magnum as the largest SB foramen, IAC, jugular foramen, and hypoglossal canal.

4.2 Fracture

Skull base fractures occur due to high-velocity blunt trauma, motorcycle collisions, pedestrian injuries, sport accidents, falls, or assault (Yilmazlar et al. 2006). These fractures are encountered in 7–16% of non-penetrating head injuries (Baugnon and Hudgins 2014). Ten percent of skull base fractures are caused by penetrating injuries most commonly from gunshot wounds (Samii and Tatagiba 2002). Clinical signs suggestive of SB fracture include Battle's sign, unilateral periorbital ecchymosis, bloody otorrhea, and acute cranial nerve deficits. Radiologists should be aware of the normal variant lucencies in pediatric SB to prevent false-positive diagnosis of SB fractures. The assessment of CT with MPR images on bone and soft-tissue windows is mandatory for comprehensive management of patients. It is important to detect SB fractures and displacement of bone fragments since dural tears are usually caused by fracture fragments.

Skull base fractures are frequently associated with complex facial fractures and might lead to important complications such as CSF leak, injury of cranial nerves and vessels, and meningitis. These fractures appear on CT as a non-corticated, non-interdigitating lucencies, with or without adjacent pneumocephalus, sinus or middle ear/mastoid opacification, or intraorbital emphysema (Fig. 22) (Baugnon and Hudgins 2014). Widening and diastasis of suture lines may also be encountered on CT.

Severe trauma to the midface or frontal region may result in ASB fracture. ASB fractures may involve posterior frontal sinus, roof of ethmoid, CP, and orbita (Figs. 23 and 24) (Kienstra and Van Loveren 2005; Manson et al. 2009). This fracture type carries a risk of CSF leak, which
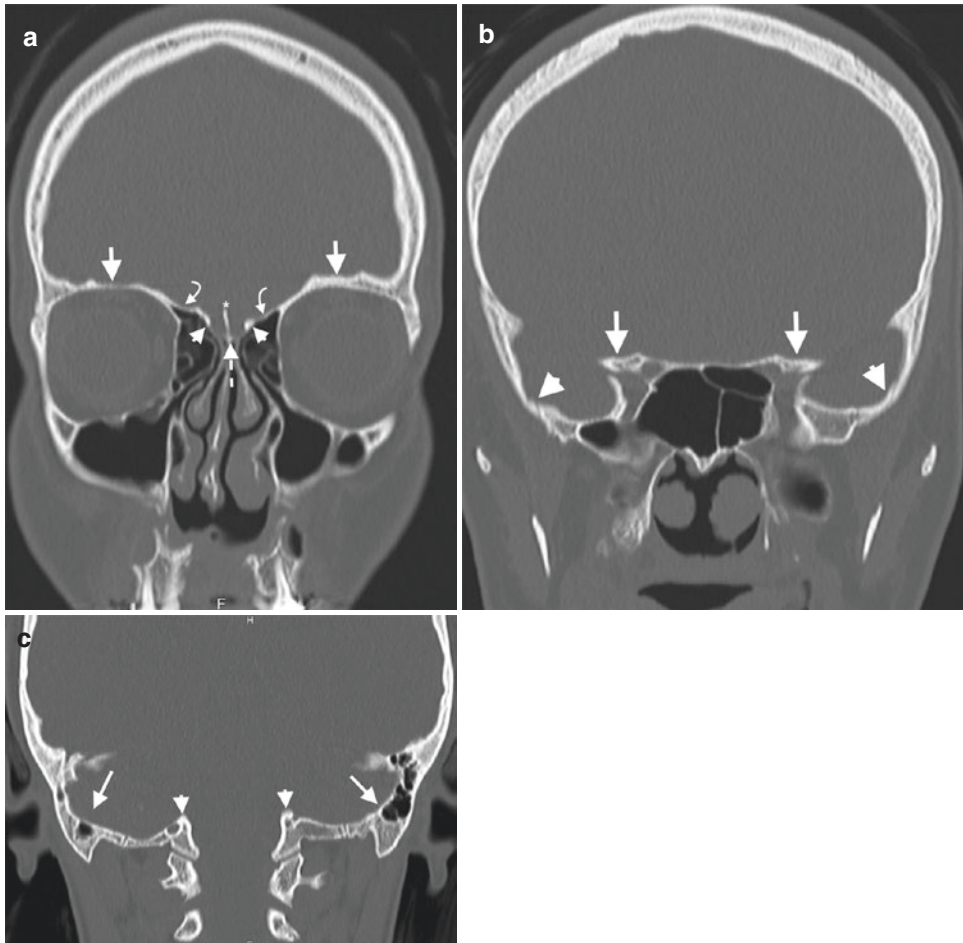
Fig. 21 Coronal CT images revealing anatomic structures in ASB, MSB, and PSB. (**a**)ASB. Coronal CT image of ASB reveals bilateral orbital roofs (arrows), fovea ethmoidalis (curved arrows), lateral lamellae (arrowheads), CP (dashed arrow), and crista galli (*). (**b**) MSB. Coronal CT image shows MSB formed by sphenoid bone (arrows) and petrous parts of the temporal bones (arrowheads). (**c**) PSB. Coronal CT image shows posterior part of the mastoid portion of the temporal bones (arrows) and occipital condyles (arrowheads)

usually presents with unilateral rhinorrhea 1 week after the trauma (Policeni and Smoker 2015). Frontobasal fractures included in ASB fractures are classified according to the localization and severity as type I, type II, and type III fractures (Table 2). CSF leak is associated with frontobasal fractures in 25% of cases (Madhusudan et al. 2006). ASB fractures may cause other complications including intraorbital injury, meningoencephalocele, and anosmia due to cranial nerve (CN) I injury (Baugnon and Hudgins 2014). Anterior and posterior ethmoidal artery grooves located in ASB may mimic frac-

tures. Characteristic location and corticated and tapering nature of margins of these artery boundaries can be helpful in distinguishing grooves from the fracture. Supraorbital canal and sphenofrontal suture may also mimic ASB fractures (Connor et al. 2005).

MSB fractures are most frequently encountered as oblique or sagittal fractures (Bobinski et al. 2016). Transverse fractures of MSB usually result from direct blow to the lateral skull and zygoma. All CSB fractures involve sphenoid sinus (Fig. 25). Cranial nerves traversing neural foramina, fissures, or canals may be injured due

Fig. 22 Axial CT image of a 31-year-old man with MVA reveals a linear fracture (arrows) traversing bilateral lesser sphenoid wings and posterior orbital plate of the frontal bone

to laceration, stretching, or transection, especially in coronally oriented CSB fractures (Feiz-Erfan et al. 2007; Mundinger et al. 2013). Carotid artery injury should be suspected in the setting of intracanalicular air after MSB fracture, especially extending to the clivus (Baugnon and Hudgins 2014). CTA or MRA should be performed in this setting in order to assess carotid artery injury. Involvement of ICA in this fracture type may result in transection, dissection, aneurysm/pseudoaneurysm, carotid-cavernous fistula, and vascular entrapment (Fig. 19) (Feiz-Erfan et al. 2007; Mundinger et al. 2013; Liang et al. 2007). Carotid dissection or occlusion presents on MRI as loss of flow voids and increased T1 and T2 signal around the periphery of the carotid arteries in crescentic shape (Baugnon and Hudgins 2014). Transverse fractures in the sphenoid sinus anteriorly or posteriorly can propagate laterally through the greater sphenoid wing and squamosal temporal bones. Greater sphenoid wing fracture may result in anterior middle cranial fossa epidural

hematomas due to associated sphenoparietal venous sinus injury. Palatovaginal canal that extends from pterygopalatine fossa to the roof of pharynx may mimic CSB fracture on axial CT images (Connor et al. 2005). Spheno-occipital synchondrosis, a transverse clival cleft in children between basisphenoid and basiocciput, and petro-occipital fissure between the clivus and the petrous apex comprise other mimickers of CSB fractures (Fig. 26) (Koch 2014).

PSB fractures include fractures of clivus, basilar part of the occipital bone, and condyles (Figs. 27 and 28). Clivus fractures are very uncommon, but cranial nerve defects involving cranial nerves II, III, IV, V, VI, VII, or VIII almost invariably accompany these fractures (Menku et al. 2004). Brainstem may also be injured in clival fractures, especially in those oriented longitudinally (Bobinski et al. 2016). Longitudinal fractures of clivus may cause vertebrobasilar artery and brainstem injury, while transverse fractures may present with carotid artery injury (Menku et al. 2004). PSB fractures most commonly cause epidural hematoma in posterior fossa due to injury to the transverse or sigmoid dural sinuses or jugular bulb (Lui et al. 1993; Karasu et al. 2008). Occipital condylar fractures are classified into three types as type I, comminuted impaction fracture of occipital condyle caused by axial loading; type II, skull base linear fracture extending into occipital condyle; and type III, avulsion fracture at the attachment site of alar ligament (Bobinski et al. 2016). PSB fractures can be mimicked by emissary vein foramens, occipitomastoid, tympanomastoid, tympanosquamous, and petrosquamous sutures.

5 Orbita

5.1 Anatomy

Bony orbit is pyramidal in shape with a roof, floor, medial wall, lateral wall, orbital opening directed anterolaterally, and an apex directed posteromedially. Orbital roof is mainly formed by orbital plate of frontal bone with contribution of the lesser wing of sphenoid bone. Medial
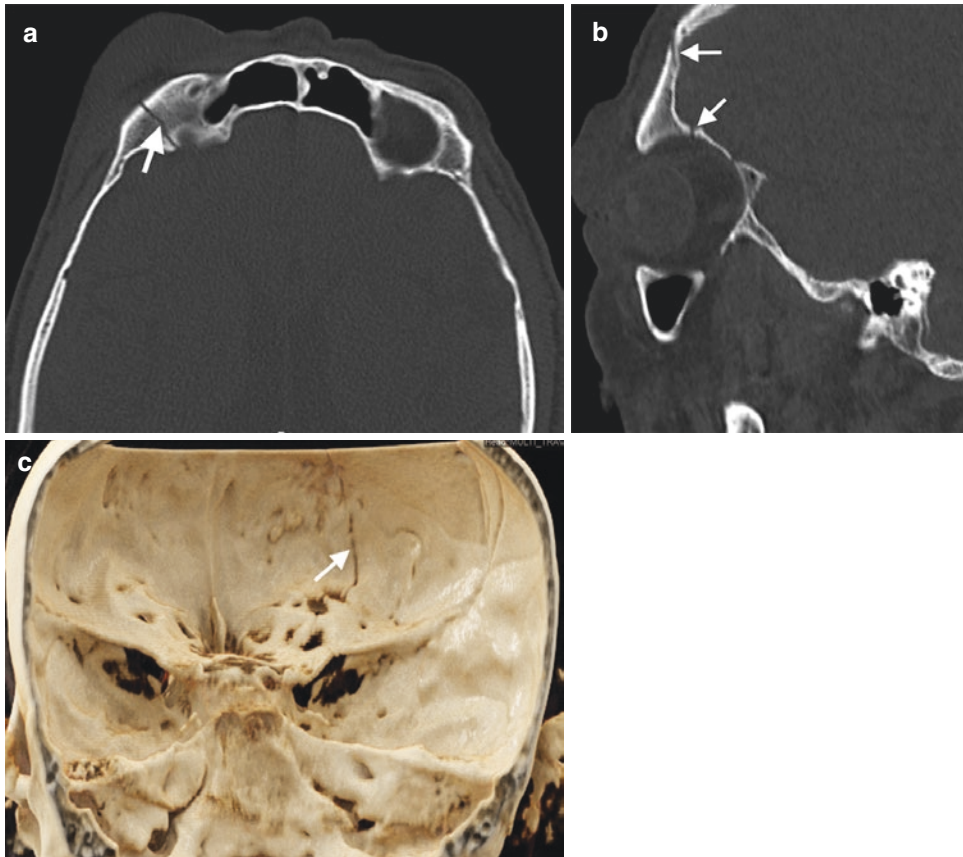
Fig. 23 Linear fracture of ASB. Axial (**a**) and coronal (**b**) CT images present a nondisplaced linear fracture (arrows) of orbital part of the frontal bone (right orbital roof) (**c**) CR image with posteroanterior view reveals that the fracture (arrow) extends from squamosal part of the frontal bone to the right orbita roof
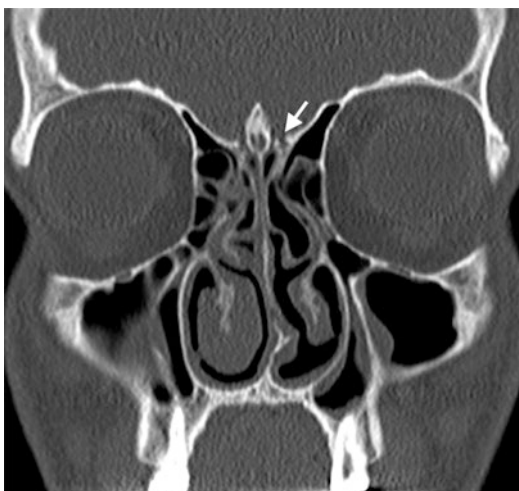

Fig. 24 ASB fracture. Coronal CT image of a 18-year-old man with a history of assault demonstrates a fracture (arrow) involving left lateral lamella

Table 2 Classification of frontobasal fractures (Manson et al. 2009)

Fracture type	Features
Type I	Isolated linear fractures of the cranial base involving the medial third of the supraorbital rim and extending posteriorly along the sella
Type II	Vertical linear fractures involving the lateral two-thirds of the supraorbital rim, orbital roof, and the lateral orbital wall
Type III	Comminuted fractures combining central and lateral frontobasilar fractures involving frontal bone and orbital roof
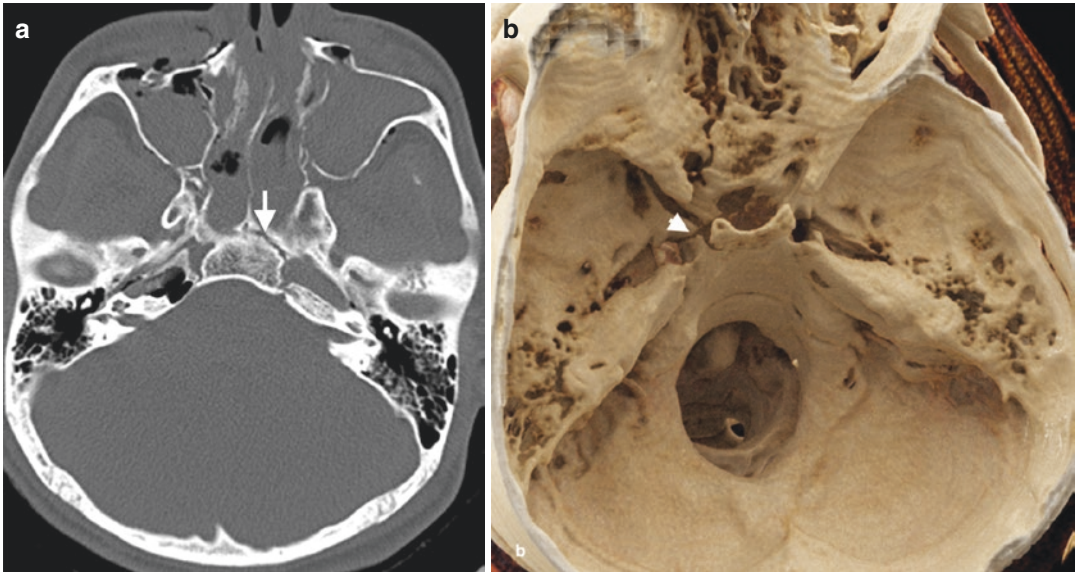
Fig. 25 MSB fracture involving left lateral wall of the sphenoid sinus. (**a**) Axial CT image reveals an obliquely oriented fracture (arrow) through left anterolateral wall of the sella. (**b**) CR image demonstrates fracture (arrowhead) of the left lateral wall of the sphenoid sinus
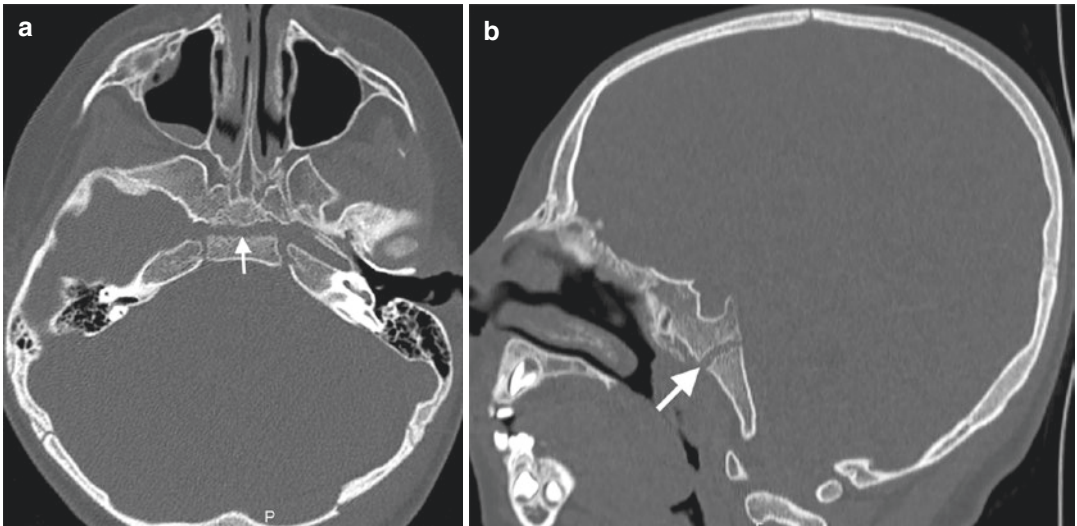
Fig. 26 Sphenooccipital synchondrosis. Axial (**a**) and sagittal (**b**) CT images reveal sphenooccipital synchondrosis (arrows) mimicking clivus fracture

orbital wall consists of ethmoid bone, lacrimal bone, frontal process of maxilla, and body of the sphenoid. Orbital floor is formed by the orbital part of the maxilla, and orbital processes of palatine and zygomatic bones. Lateral wall is comprised of frontal process of zygomatic bone in
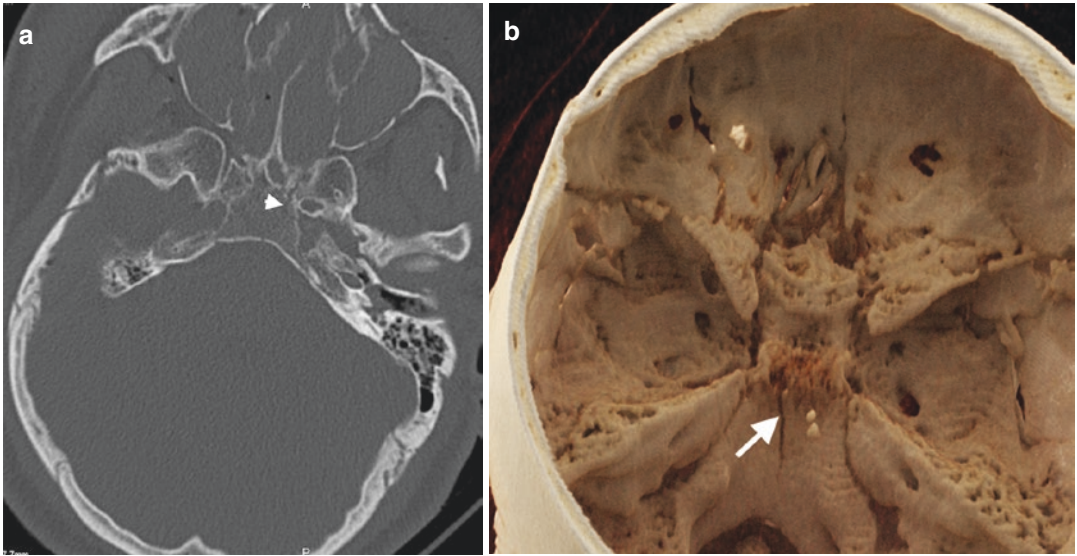
Fig. 27 Linear fracture in clivus. (**a**) Axial CT image on bone window demonstrates a subtle linear fracture (arrowhead) in clivus. (**b**) CR image demonstrates longitudinally oriented linear fracture (arrow) at the cranial aspect of the clivus
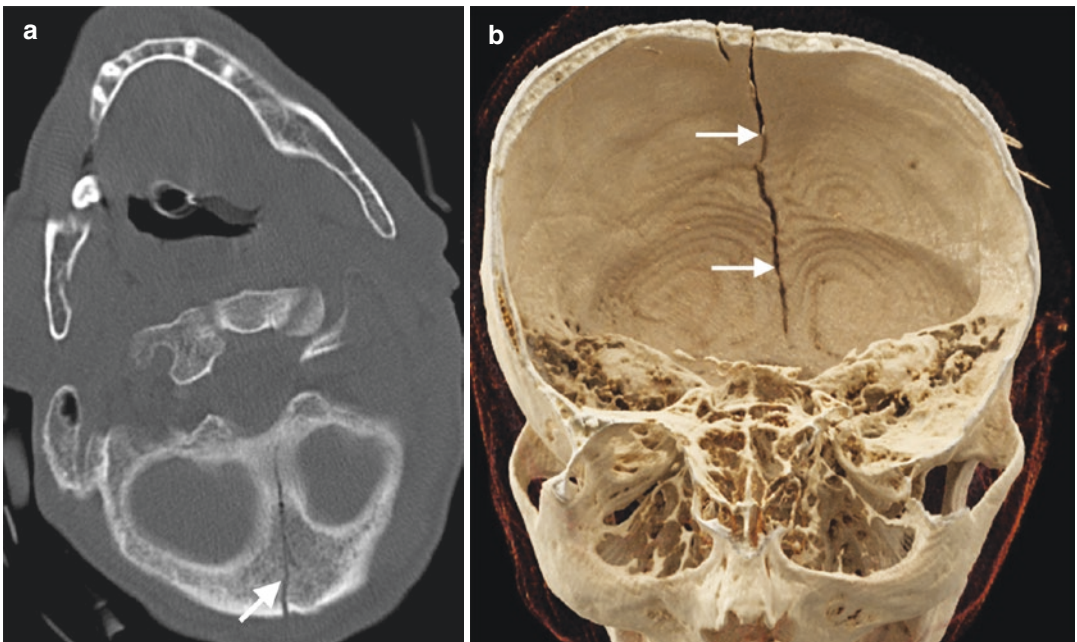
Fig. 28 Occipital bone fracture involving PSB. (**a**) Axial CT image demonstrates a linear fracture (arrow) extending from squamosal part of occipital bone through basilar part. (**b**) Superoinferior view of CR image shows fracture (arrows) involving squamous and basilar parts of occipital bone

front and greater wing of sphenoid in behind. Optic canal and superior orbital fissure form orbital apex. Lateral wall is the thickest orbital wall, whereas medial wall formed by the lamina papyracea is the thinnest wall followed by orbital floor.

5.2 Fracture

Orbital fractures maintain 10–30% of facial fractures (Ellis 2012; Roth et al. 2010). Injury of bony orbit may be seen as isolated fractures such as fracture of the orbital floor, medial wall, lateral wall, and roof or occurs as a part of combined fracture such as zygomaticomaxillary complex (ZMC), naso-orbitoethmoid (NOE), and Le Fort fractures. Although outer rim of the orbits is composed of thick bones, inner orbit bones are susceptible to fractures due to their thin structures.

Orbital fractures should be assessed with MPR CT images. Coronal CT images have the greatest utility to depict the fracture, size of the orbital wall defect, and the change in orbital shape and volume (Roth et al. 2010; Rothman et al. 1998). Posterior extent of orbital floor defects may be depicted on sagittal images, while axial images can show posterior extent of medial wall fractures (Dreizin et al. 2018). Soft-tissue content of orbita including extraocular muscles, globe, and fibrofatty tissue should be assessed by reviewing MPR CT images on soft-tissue window. Majority of orbital fractures is comprised of blow-out and blow-in fractures. Blow-out fractures result from a direct blunt force to the orbit and increased intraorbital pressure. This fracture type mainly affects the medial wall and orbital floor as weakest parts of the bony orbit results in displacement of bone fragments into the ethmoid cells/nasal cavity or maxillary sinus and herniation of orbital fat content with extraocular muscles to these regions (Winegar et al. 2013). An accurate diagnosis of blow-out fracture can be accomplished by reviewing sagittal and coronal CT images to evaluate the size of the wall defect and possible herniation of soft tissues or extraocular muscles. Immobilization of the herniated muscle in the fracture site (entrapment) is a potential complication of blow-out fractures (Fig. 29). Medial rectus and inferior rectus muscles should appear flattened on axial and coronal CT images, respectively (Lo Casto et al. 2012). Entrapment of extraocular muscles manifests on CT and MR images as an abrupt kink or rounding of the muscle characterized by a 1:1 height-to-width ratio with protrusion into the adjacent eth-

moidal or maxillary sinus (Fig. 30) (Lo Casto et al. 2012). Only fat content herniation may also cause entrapment of muscles due to the retractile effect of fibrous septations between herniated fat and extraocular muscles. Orbital emphysema may be encountered on CT in blow-out fractures secondary to wall defect between orbita and maxillary sinus; however, it should be kept in mind that increased intranasal pressure can also cause air passage from nasal cavity to the orbita. In pediatric population, orbital floor fracture may present as trapdoor fracture in which the flexible bone fracture fragment returns to the orbital floor with inferior rectus muscle persisting in the maxillary sinus. This fracture occurs secondary to relatively deficient mineralization of the orbital floor (Koch 2014). Trapdoor fractures may present with silent clinical features with absence of swelling and ecchymosis and are called as "white-eyed blow-out fracture" (Jordan et al. 1998). Coronal CT images demonstrate inferior rectus muscle below orbital floor with or without fracture fragment of the orbital floor (Fig. 31) (Winegar et al. 2013; Grant 3rd et al. 2002). Trapdoor fracture may cause ischemia and necrosis of the entrapped muscle leading to fibrosis, scarring, and persistent diplopia (Koch 2014). Clinically important late enophthalmos can be predicted by the following the initial CT criteria: defect's surface area greater than 2 cm^2, more than 25–50% orbital floor or medial wall involvement, collapse of the junctional bulge and internal orbital buttress, and soft-tissue herniation with volume displacement greater than 1.5 mL (Ellis 3rd 2012; Roth et al. 2010; Burm et al. 1999). It should be noted that small fractures affecting medial wall may manifest just as an opacification of ethmoid cells or herniation of intraorbital fat with no displaced bone fragment. Developmental dehiscence of the lamina papyracea can mimic orbital blow-out fractures with the appearance of bowed medial orbital wall toward the ethmoid complex and herniated medial extraconal fat through the defect (Fig. 32). Orbital blow-out fractures may present with intraorbital hemorrhage, globe injury, and injury of the infraorbital nerve in the setting of orbital floor fracture (Figs. 33, 34 and 35) (Winegar et al. 2013).
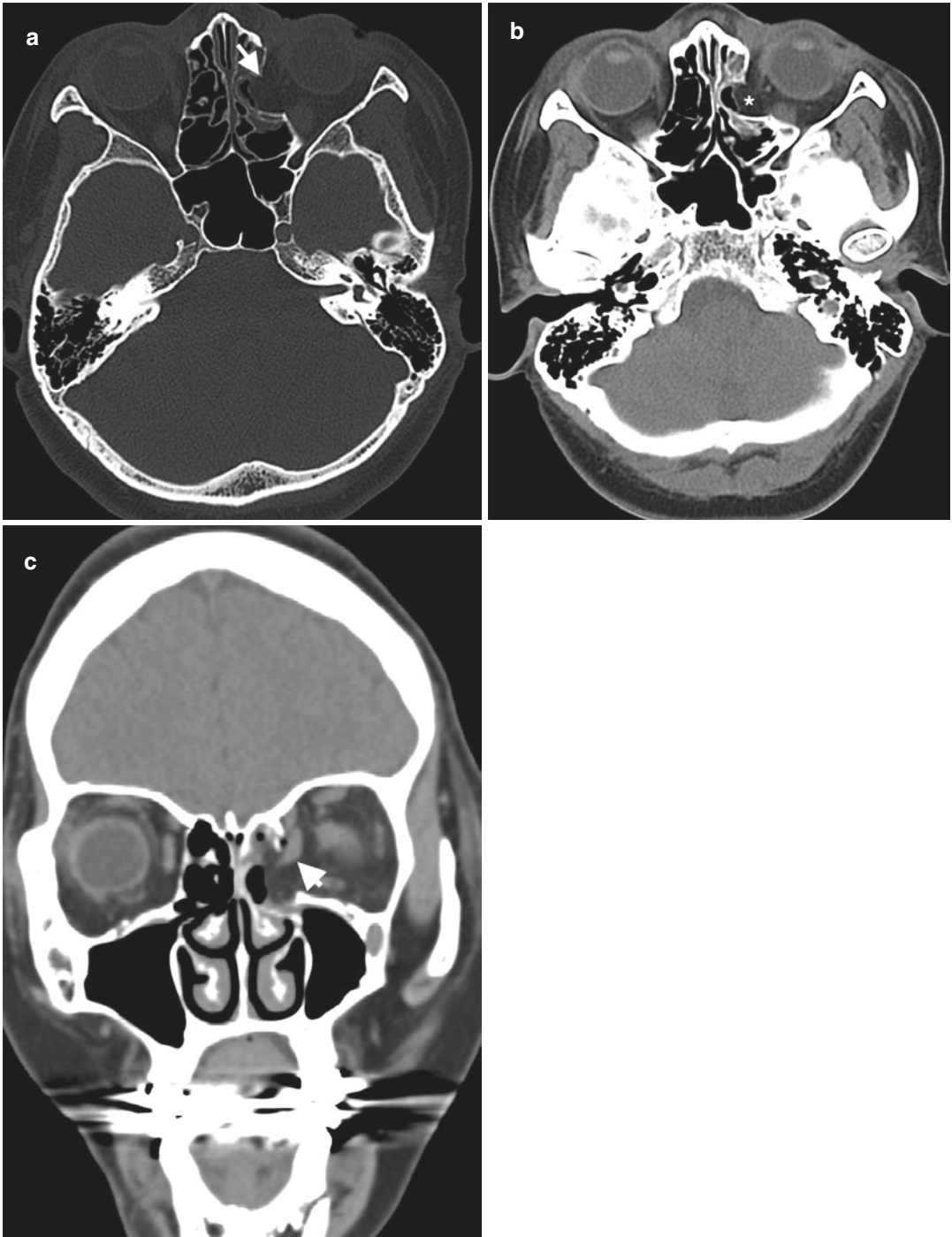
Fig. 29 Blow-out fracture. (**a**) Axial CT image of a 39-year-old woman with a history of fall demonstrates a medial orbital wall defect (arrow). (**b**) Axial CT image on soft-tissue window reveals herniation of extraconal fat (*) through the medial wall defect. (**c**) Coronal CT image on soft-tissue window shows kinking and entrapment of left medial rectus muscle (arrowhead) herniating through the medial orbital wall defect into the ethmoidal cells
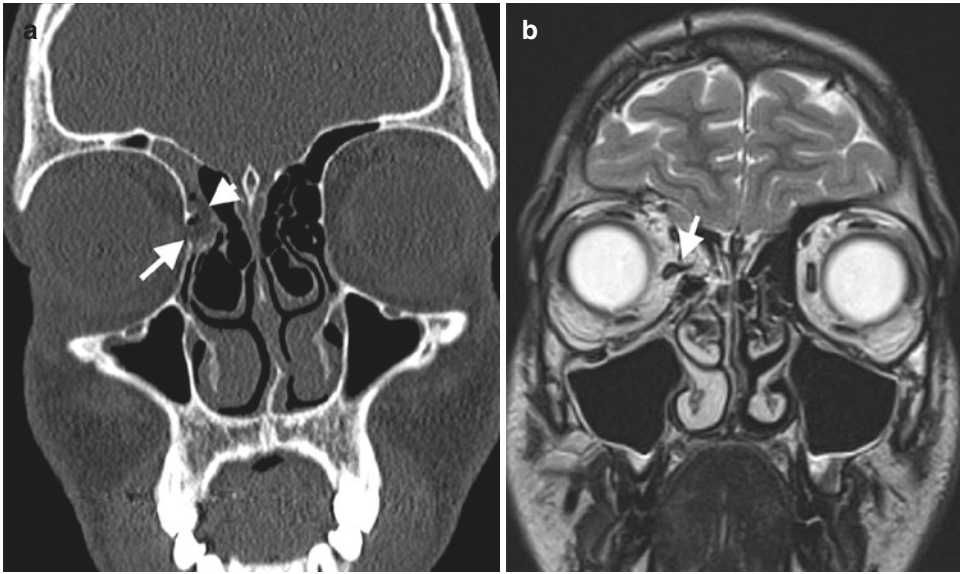
Fig. 30 Blow-out fracture with entrapment of medial rectus muscle in a 14-year-old man with a history of assault. (**a**) Coronal CT image reveals a defect (arrow) in right medial orbital wall with fat herniation to the adjacent ethmoidal sinuses (arrowhead). (**b**) Coronal T2-weighted MR image demonstrates entrapment of right medial rectus muscle (arrow)
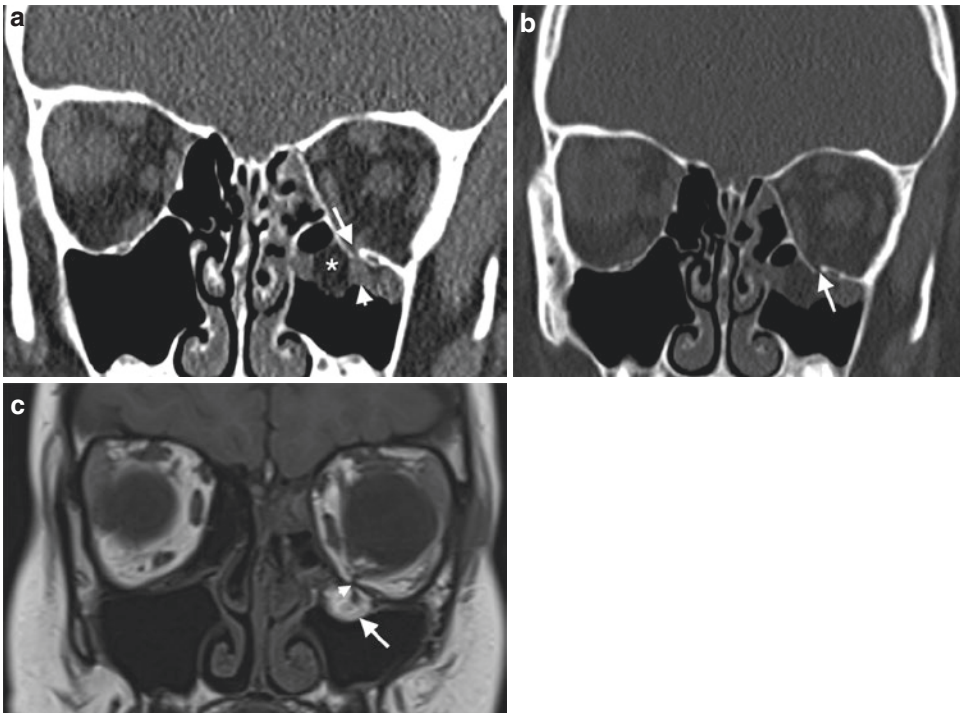
Fig. 31 Trapdoor fracture in a 11-year-old woman with a history of MVA. Coronal CT images on soft (**a**) and bone (**b**) window images reveal left inferior orbital wall fracture (arrows) with fat (*) herniation into the left maxillary sinus. (**c**) Coronal T1-weighted MR image reveals herniation of left orbital extraconal fat (arrow) into the left maxillary sinus. Although fracture defect is almost closed, inferior rectus muscle is entrapped in the left maxillary sinus below the left orbital floor (arrowhead) consistent with trapdoor fracture
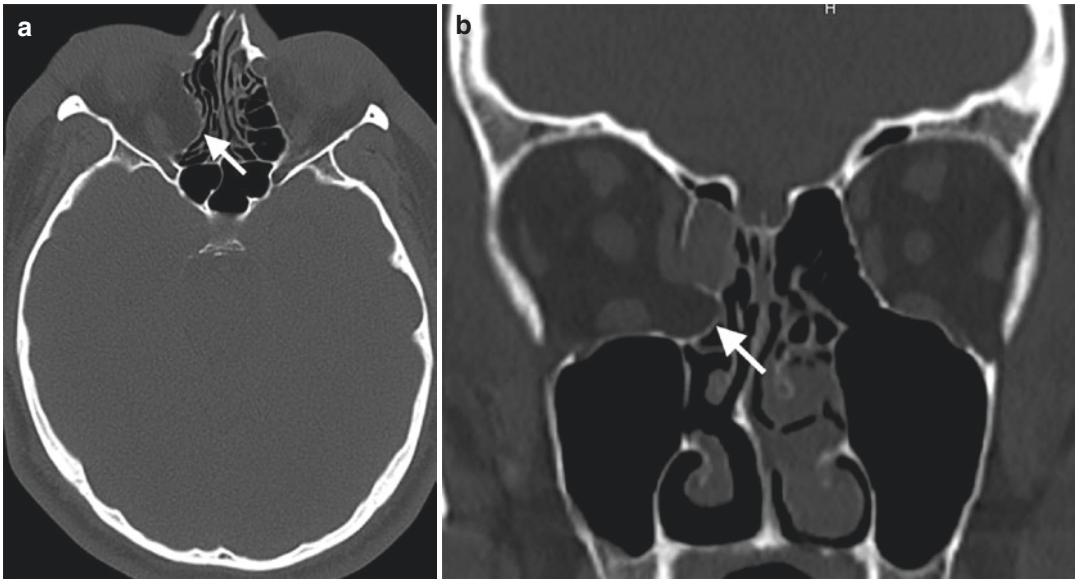
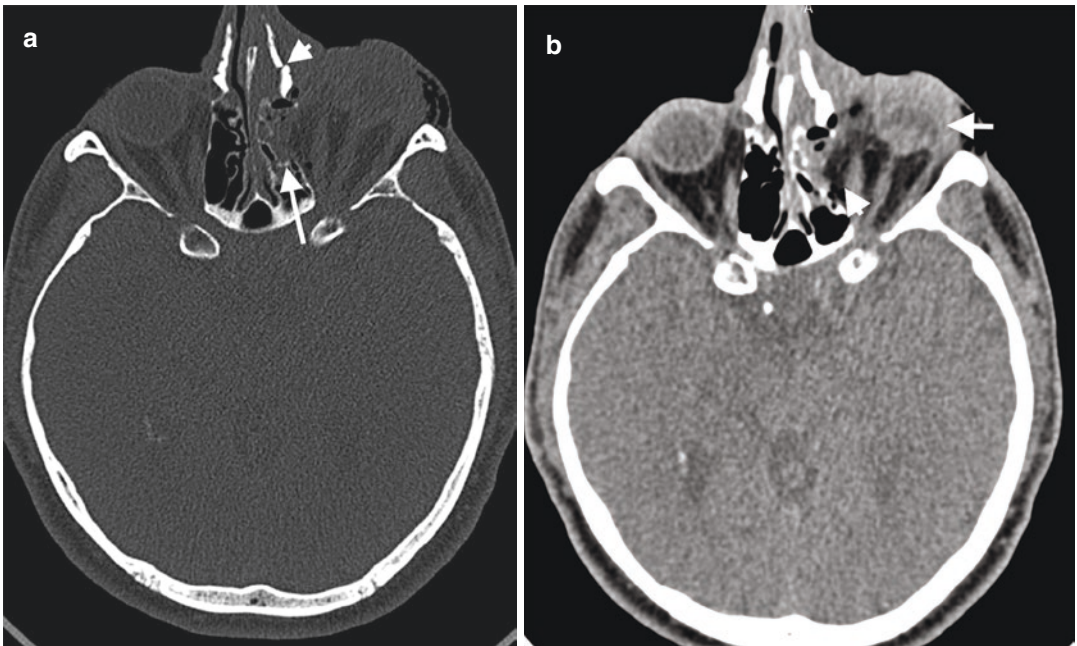**Fig. 32** Axial (**a**) and coronal (**b**) CT images of a patient reveal dehiscence of the right lamina papyracea (arrows) that mimic blow-out fracture of right orbita. No medial wall defect exists as well as accompanying orbital soft-tissue injury suggestive of blow-out fracture

Fig. 33 Blow-out fracture with globe perforation in a 46-year-old man with a history of assault. (**a**) Axial CT image on bone window shows blow-out fracture of left orbital wall (arrow) and left nasal bone fracture (arrowhead). (**b**) Axial CT image on soft-tissue window reveals perforation of left globe with volume loss and intraocular hemorrhage (arrow)
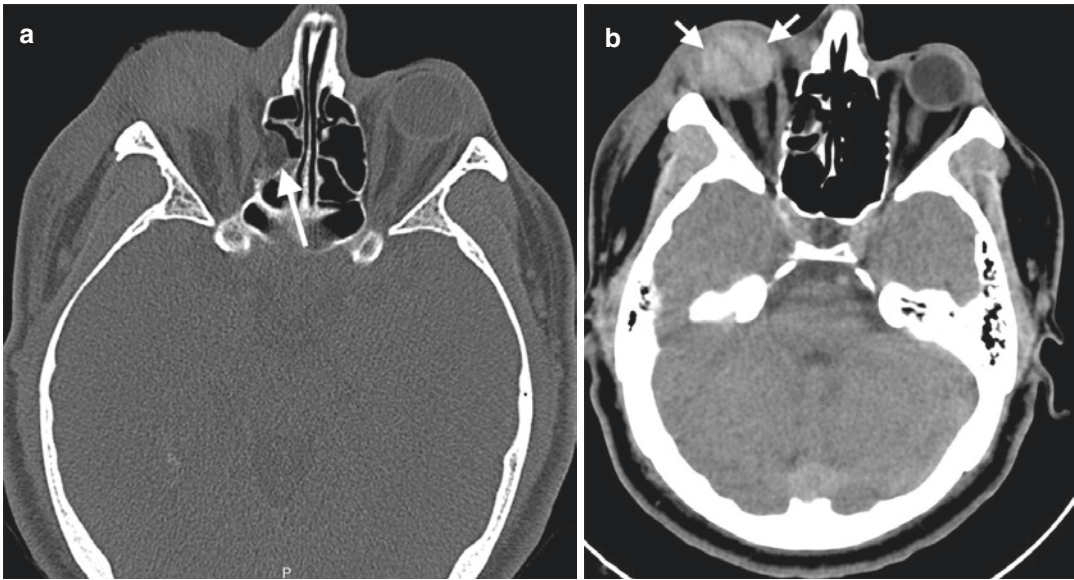
Fig. 34 Blow-out fracture with globe hemorrhage in a 42-year-old man with a history of MVA. (**a**) Axial CT image on bone window shows blow-out fracture of right orbital wall (arrow). (**b**) Axial CT image on soft-tissue window reveals hyperdense hemorrhage within the right globe (arrow)

Penetrating injuries may also cause orbital wall fractures (Fig. 36).

Blow-in fractures are characterized by displacement of bony fragments of frontal bone into the intraorbital soft tissues through the orbital roof. This fracture type occurs due to direct impact to the supraorbital rim or frontal bone with the transmitting force directed toward the orbital roof (Fig. 37) (Uzelac and Gean 2014). Free bone fragments may cause orbital muscle or globe laceration. Orbital roof fractures are more common in pediatric population (Koch 2014). Posterior extension of the orbital roof fractures should also be evaluated for a possible orbital apex injury that has a potential for optic nerve and oculomotor nerve injury. The presence of orbital apex fractures necessitates exclusion of retrobulbar hematoma and bony impingement on the optic nerve (Koch 2014). Orbital roof fractures may be associated with CSF leak, pneumocephalus, and intracranial complications.

Orbital rim fractures occur due to high-energy trauma and may involve superior, lateral, and inferior orbital rims. Superior orbital rim fracture, being the most common, may result in inferior and anterior displacement of the globe. Subperiosteal hematoma may accompany orbital rim fractures. Extension of orbital floor fractures to the superior orbital fissure may cause superior orbital fissure syndrome, which occurs due to injury of cranial nerve III, IV, VI, and ophthalmic branch of the V nerve (Winegar et al. 2013). Extension of fracture through orbita apex may result in orbital apex syndrome, which is characterized by optic nerve impingement resulting in decreased vision clinically. Fractures of lateral orbital wall are usually associated with ZMC fractures (Fig. 38) (Dreizin et al. 2018). Inferior orbital rim fractures may involve inferior orbital foramen, thereby inferior orbital nerve resulting in anesthesia of cheek and upper lip. Orbital rim fractures may be complicated with other ocular injuries including globe rupture, retrobulbar hematoma, optic nerve injury, and lens dislocation. The assessment of globe in the setting of orbita fracture may be crucial.
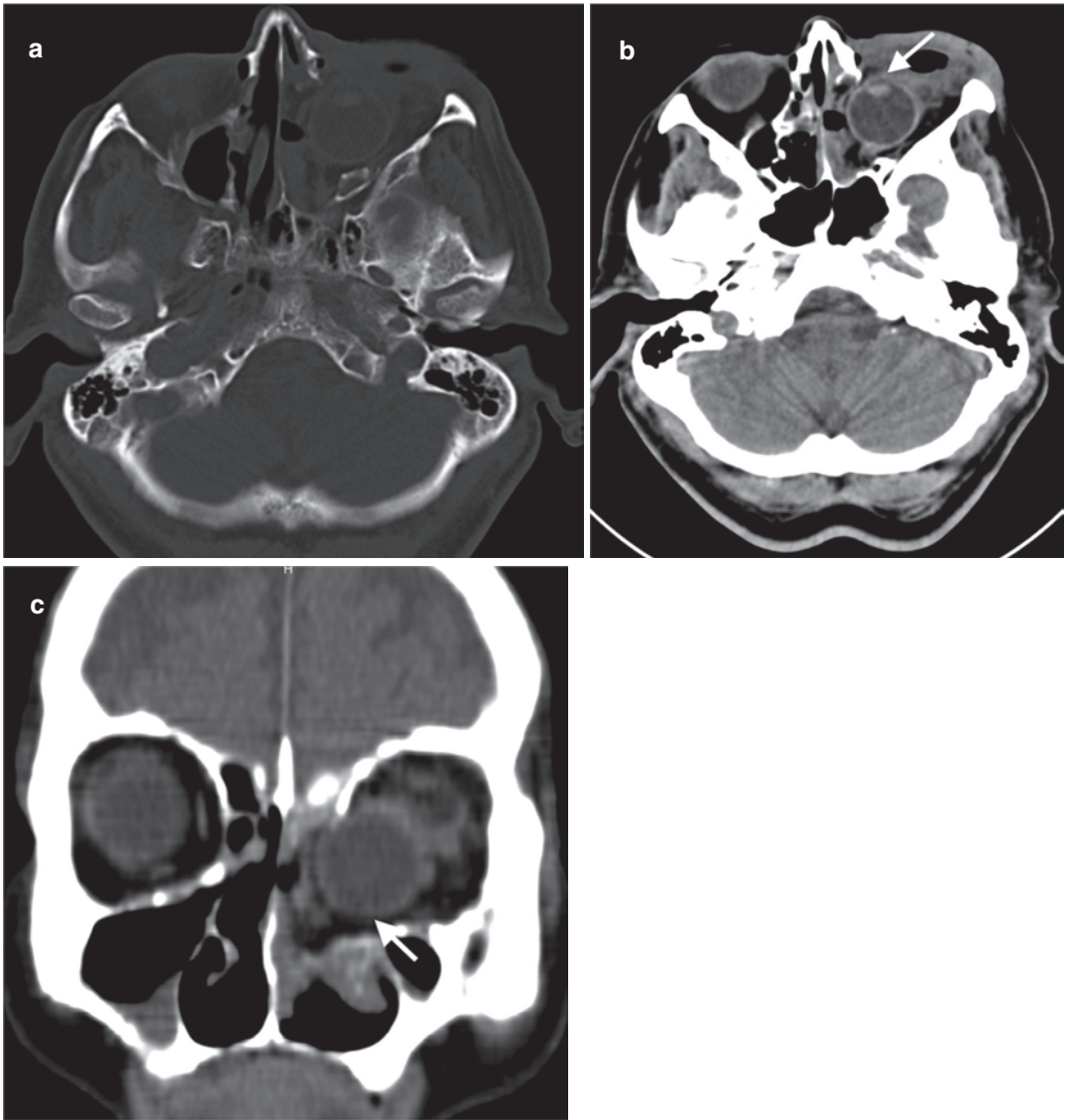
Fig. 35 Internal globe herniation secondary to blow-out fracture in a 75-year-old man. (**a**) A blow-out fracture with a large defect of left orbital wall is seen at bone window axial CT image. Axial (**b**) and coronal (**c**) CT images at soft-tissue window demonstrate inferomedial herniation of the left globe (arrows) into the ethmoidal cells through the inferomedial wall defect

Anterior chamber of globe can be evaluated by volume change. Volume decrease in anterior chamber may indicate corneal laceration or anterior displacement of the lens. Increase in the anterior chamber volume may indicate posterior chamber rupture (Uzelac and Gean 2014). Lens should be assessed in terms of dislocation. Posterior chamber should be interrogated in terms of globe rupture, retinal detachment, and hemorrhage.
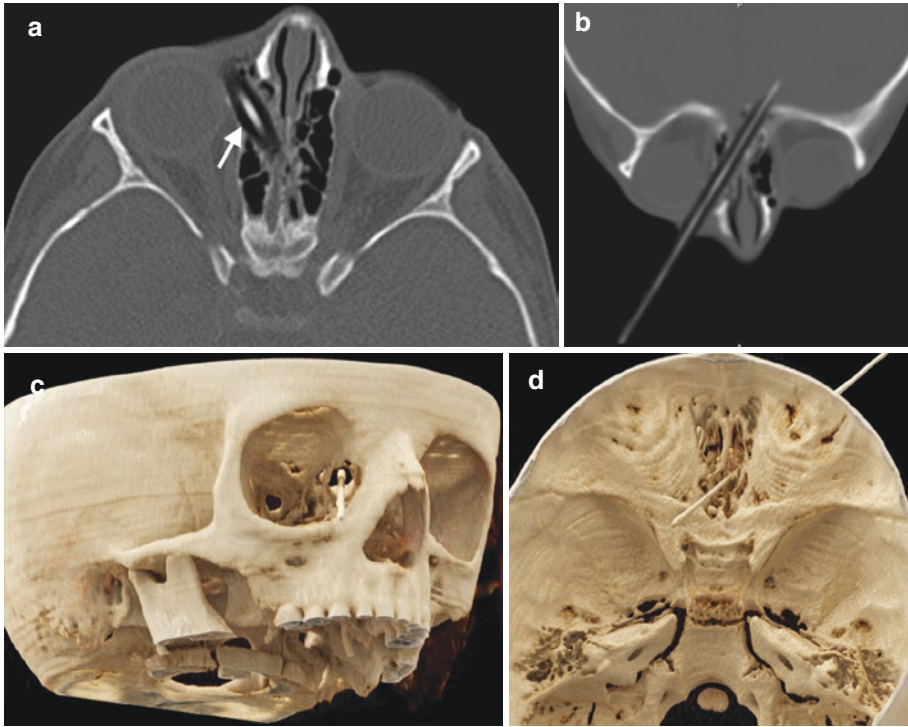
Fig. 36 Penetrating trauma of orbital wall in a 4-year-old man with a history of pencil stuck. Axial bone window CT (**a**), coronal MPR image (**b**), and CR (**c**, **d**) images dem-onstrate a penetrating pencil passing through right medial orbital wall and stucking into the frontal lobe crossing the CP
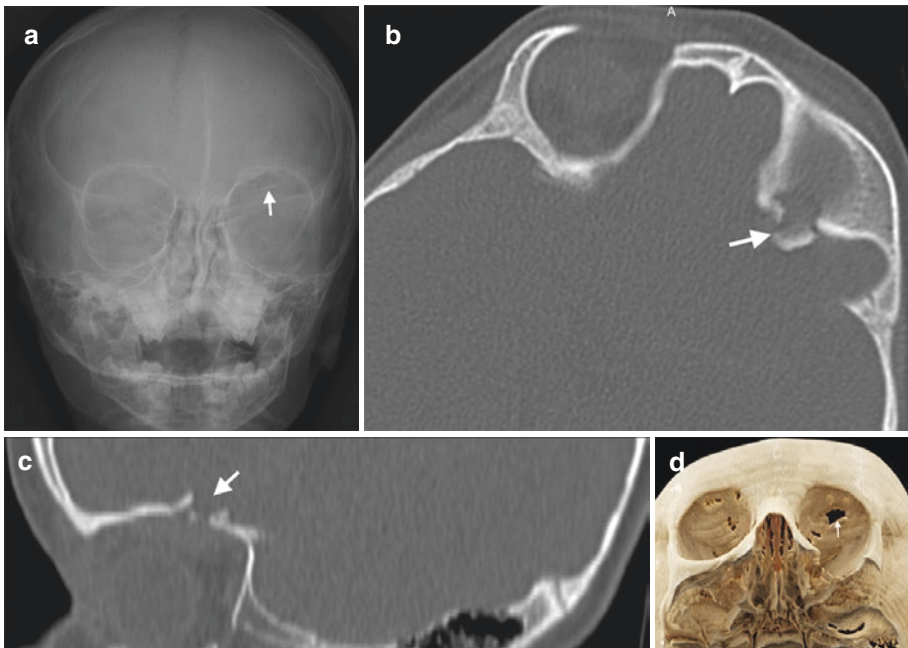
Fig. 37 Orbital roof fracture. (**a**) Skull radiograph in A-P position demonstrates an oval shape radiolucency (arrow) representing a defect in the left orbital roof. Axial (**b**) and sagittal (**c**) bone window CT images demonstrate the frac-ture (arrows) in the left orbital roof. (**d**) CR image shows the bone defect (arrow) in the orbital roof

Fig. 38 Lateral wall fracture of the orbita. Axial (**a**) and coronal (**b**) CT images of a 52-year-old male patient with MVA show lateral wall fracture (arrows) of left orbita

6 Maxillofacial Bones

6.1 General Information

Maxillofacial skeleton is composed of zygomatic, maxillary, nasal, lacrimal, palatine, and mandible bones. Facial skeleton is considered as a network of horizontally and vertically aligned bony buttresses, which refer to bony structures of substantial thickness and lines of osseous thickening formed by articulating facial bones. Facial buttresses increase the resistance of facial skeleton to trauma and provide a rigid framework for orbital contents, sinuses, teeth, and nasal cavity (Winegar et al. 2013). Maxillofacial buttress network distributes mechanical energy resulting in propagation of fractures through facial bones. Importance of facial buttresses is based on the fact that disruption of these buttresses results in change in facial dimensions. Horizontal buttresses of facial skeleton are comprised of superior orbital rim, upper transverse maxillary, lower transverse maxillary, upper transverse mandibular, and lower transverse mandibular buttresses. Vertical buttresses of facial skeleton consist of medial maxillary (nasomaxillary), lateral maxillary (zygomaticomaxillary), posterior maxillary (pterygomaxillary), and posterior vertical mandibular (mandibular) buttresses (Table 3 and Fig. 39).

Maxillofacial fracture patterns may differ in children due to flexible suture lines, greater flexibility of osseous structures of the face, and a thicker subcutaneous fat as a protective layer that makes facial skeleton of children more resistant to fractures (Zimmermann et al. 2005; Alcala-Galiano et al. 2008). Incomplete development of paranasal sinuses in children increases the stability and decreases the incidence of midface fractures (Koch 2014).

6.2 Imaging Techniques

6.2.1 Radiography

Plain film radiography has a very limited role in evaluation of facial skeleton fractures due to overlap of maxillofacial bones on 2D imaging. Patient positioning for radiography may be difficult and potentially dangerous in the setting of trauma. Caldwell (P-A) or axial view radiographies may be helpful for delineation of the zygomatic arch. Occipitomental or Waters view can delineate inferior and lateral orbital walls and the

Table 3 Vertical and horizontal facial buttresses network (Fig. 39) (Winegar et al. 2013; Lo Casto et al. 2012)

Vertical buttress system	Localization
Medial maxillary buttress (nasomaxillary)	Extends from the nasofrontal suture inferiorly along the lateral margin of the pyriform aperture to the maxillary alveolar process
Lateral maxillary buttress (zygomaticomaxillary)	Extends from zygomaticofrontal suture inferomedially along the lateral orbital rim across the zygomaticomaxillary suture to terminate in the maxillary alveolar process
Posterior maxillary buttress (pterygomaxillary)	Between the posterior maxillary alveolus and pterygoid processes of the sphenoid bone
Posterior mandibular buttress (mandibular)	Portions of angle, ramus, and condyle, along the posterior border of the mandible
Horizontal buttress system	
Superior orbital rim	Includes orbital roofs, CP, and fovea ethmoidalis
Upper transverse maxillary buttress (inferior orbital rim)	Extends inferiorly from the level of the nasofrontal suture, proceeds along the inferior edge of the orbit, and ends in zygomaticotemporal suture
Lower transverse maxillary buttress (maxillary alveolar rim)	Oriented horizontally along the maxillary alveolar process. Extends posteriorly to include the hard palate
Upper transverse mandibular buttress (mandibular alveolar rim)	Encompasses the mandibular alveolar process
Lower transverse mandibular buttress (inferior mandible border)	Inferior margin of the mandible

zygomatico-alveolar arch. Craniofacial fractures may manifest on radiographs as interruption in bony continuity, abnormal bony overlap with double density of bone appearance and abnormal linear densities secondary to rotated fracture fragments, and air density in adjacent soft tissues.

6.2.2   CT

Maxillofacial CT scanning area should extend from the top of the frontal sinus to the bottom of the hyoid bone to include the entire maxillofacial skeleton. Axial CT images should be acquired at submillimeter thickness (<1 mm) or 1.25 mm thickness with overlap to acquire high spatial resolution images with 3D images. CT images may be reviewed at 1.5–2-mm-thick reformatted images in the axial, coronal, and sagittal planes on soft tissue and bone window settings. Complex fractures involving multiple planes should be assessed with 3D images. 3D imaging is also preferred by surgeons owing to 360° rotation facility to simulate facial alignment for preoperative planning (Lo Casto et al. 2012). 3D imaging has limitations due to relevant artifacts during the reformation process, which may result in decreased

ability to visualize nondisplaced fractures (Saigal et al. 2005). Additional oblique or curved reformations may be helpful to delineate the fracture.

MR imaging, thanks to high soft-tissue contrast, can be used to demonstrate soft-tissue injury and cranial nerve deficits associated with facial skeleton injury. MRI cannot be used in evaluation of craniofacial fractures due to signal loss in cortical bones.

6.3   Frontal Sinus

6.3.1   Anatomy

Frontal sinus is located inferiorly to the squamous part of the frontal bone and represents superior portion of the facial skeleton. Frontal sinus consists of air between a thick anterior and thin and relatively delicate posterior walls (Mehta et al. 2012). The dura and frontal lobes lie just behind the posterior wall of frontal sinus. Drainage of the frontal sinus is maintained by nasofrontal duct, also known as frontal recess, located at the inferomedial aspect of frontal sinus and extends into the middle meatus of nasal cavity (Fig. 40) (Mehta et al. 2012).
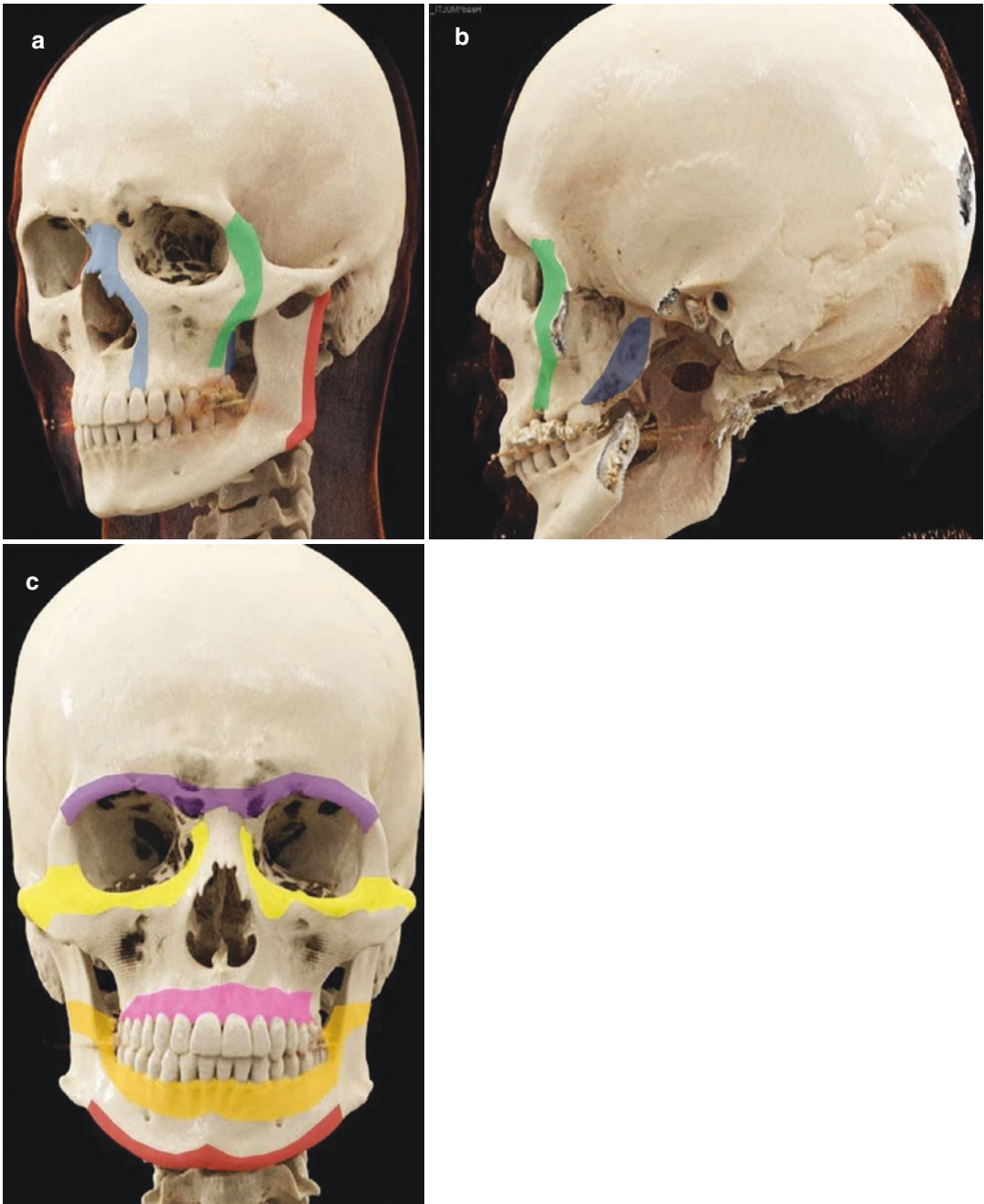
Fig. 39 Facial buttresses are shown as colored regions on CR images. Left oblique (**a**) and lateral (**b**) views reveal vertical facial buttresses. Medial maxillary buttress (blue), lateral maxillary buttress (green), posterior maxillary buttress (dark blue), and posterior mandibular buttress (red). (**c**) Horizontal facial buttresses. Superior orbital rim (purple), upper transverse maxillary buttress (yellow), lower transverse maxillary buttress (pink), upper transverse mandibular buttress (orange), and lower transverse mandibular buttress (red)
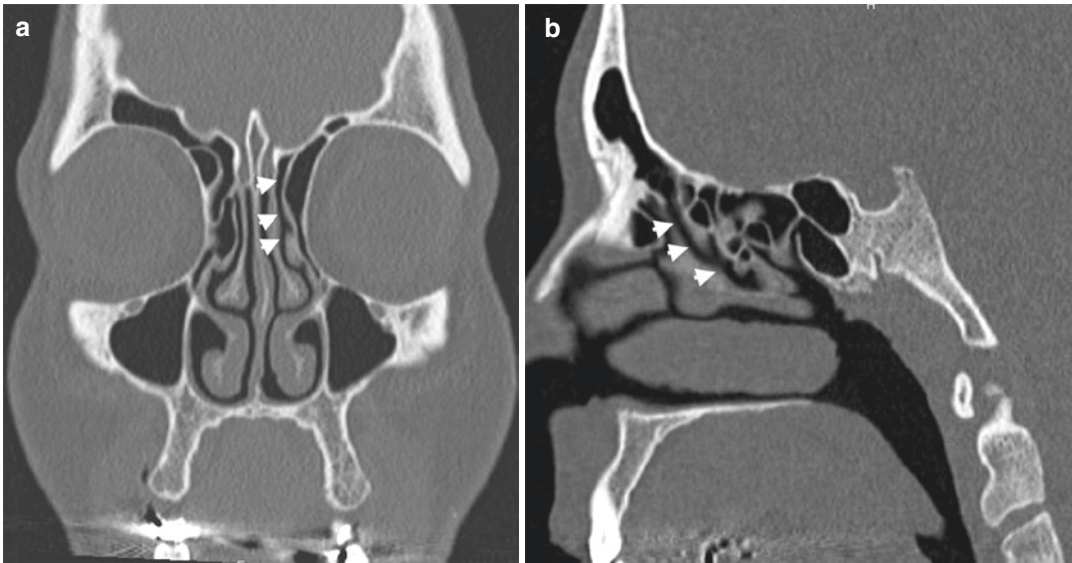
Fig. 40 Coronal (**a**) and sagittal (**b**) CT images demonstrate nasofrontal duct (arrowheads) extending from frontal sinus to the middle meatus

6.3.2 Fracture

Frontal sinus fractures may occur in patients with direct trauma to the sinus part or extension of a calvarial bone fracture into the sinus (Metzinger et al. 2005). Considerable force is required to cause frontal sinus fractures, which were found to be accompanied by another facial fracture in 83% of patients and intracranial injury in 54% of patients (McRae et al. 2008).

Axial CT images have the greatest utility in assessment of frontal sinus. Opacification of frontal sinus with air–fluid level highly indicates traumatic hemorrhage in the frontal sinus.

Involvement of anterior and/or posterior frontal sinus walls and presence or absence of displacement constitute the mainstay issues to be mentioned in assessment of frontal sinus fractures. Displaced frontal sinus fracture refers to displacement of involved bone segment higher than 2 mm or thicker than the width of the sinus wall. Two-thirds of cases with frontal sinus fracture present with involvement of only anterior wall (Fig. 41). Internal mucosal lining is invariably teared after anterior wall fractures, which present almost always with hemorrhage in the sinus. In these patients, cosmetic treatment is only needed if a displaced fracture is observed.

Isolated fracture of posterior wall occurs uncommonly (5% of patients) (Schmitt et al. 2014). Fractures involving posterior wall frequently tear adjacent dura mater and may result in CSF leaks, pneumocephalus, meningitis, encephalitis, posttraumatic encephalocele, and abscess. Intracranial hemorrhage and direct traumatic brain injury may be caused by posteriorly projected fracture fragments. Fracture of posterior wall results in communication with the anterior cranial fossa and necessitates to interrogate intracranial air (pneumocephalus) and bone fragments on bone window CT images (Fig. 42). Another potential complication of frontal sinus fracture is intracranial spread of a pre-existing sinus infection through the fractured sinus wall. Frontal sinus fractures also may rarely cause orbital emphysema and CSF leakage into the orbit. Comminuted fractures present with multiple fracture fragments (Fig. 43).

Association of frontal sinus fractures with NOE injuries is not infrequent (Kienstra and Van Loveren 2005). Involvement of the base of frontal sinus, anterior ethmoids, or both in the setting of frontal sinus fracture may cause nasofrontal duct injury. Imaging findings suggestive of nasofrontal duct injury include fracture
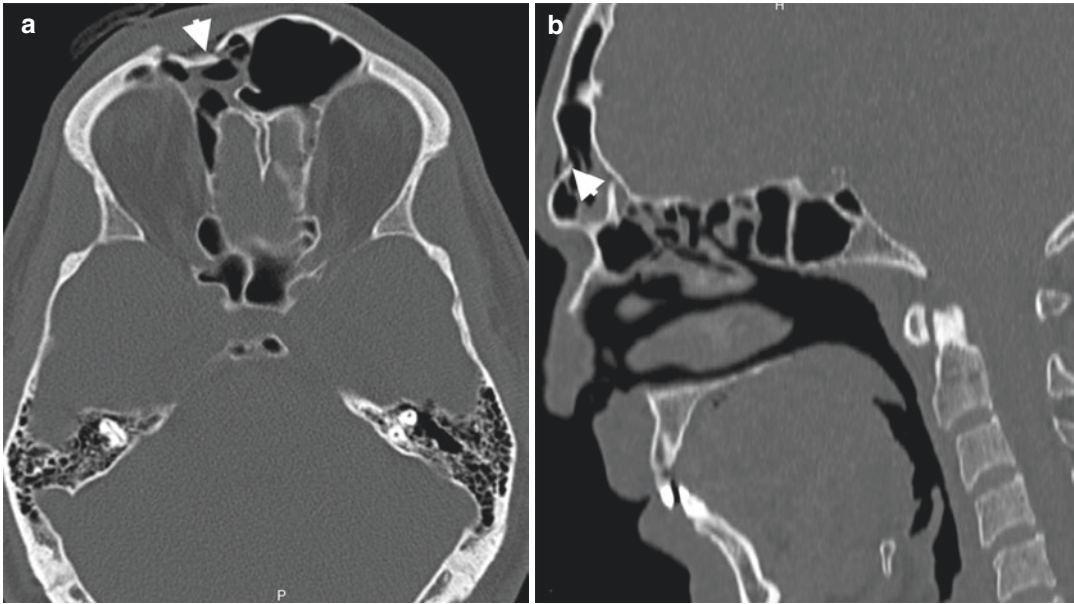
Fig. 41 Anterior frontal sinus wall fracture. Axial (**a**) and sagittal (**b**) CT images reveal depressed fracture (arrowheads) of the anterior wall of the frontal sinus

fragments within the nasofrontal outflow tract and frontal sinus floor fracture oriented anteromedially (Rodriguez et al. 2008). Nasofrontal duct injury in frontal sinus fractures may be complicated with formation of mucocele, mucopyocele, osteomyelitis, and abscess secondary to impaired frontal sinus drainage (Fig. 44) (Patel et al. 2012). Medial wall fracture of frontal sinus may result in propagation of the fracture through CP and the roof of ethmoidal cells leading to dural tear (Schmitt et al. 2014). Fractures through the lateral aspect of frontal sinus can extend to the orbital roof depending on lateral extent of frontal sinus pneumatization (Schmitt et al. 2014).

Key imaging findings that influence surgical management of frontal sinus fractures include involvement of frontal sinus walls, presence of displacement, involvement of nasofrontal duct, and presence of a dural tear. Anterior wall fractures of frontal sinus can be managed observed if nondisplaced. Displaced fractures may necessitate surgical repair in terms of cosmetic considerations. Posterior wall fractures, if nondisplaced, can be treated conservatively with close imaging follow-up. Displaced posterior wall fractures with pneumocephalus need to be repaired by surgery.

6.4 Nasal Bone

6.4.1 Anatomy

The nasal skeleton, also called as bony nasal pyramid, is comprised of two nasal bones that articulate with each other in the midline forming the nasal bridge. Nasal bones articulate with nasal process of frontal bone superiorly at the frontonasal suture and the frontal process of maxilla laterally at the nasomaxillary sutures (Dreizin et al. 2018). Nasal septum is formed by vomer inferiorly and perpendicular plate of the ethmoid superiorly, nasal crest of maxilla, and nasal crest of palatine bone posteriorly. The upper portion of nasal bone is the thicker and more resistant to fractures than the lower and thinner portion.

6.4.2 Fracture

Nasal bone fractures are encountered in approximately 50% of all facial fractures and are usually caused by blunt forces applied from anterior and lateral directions
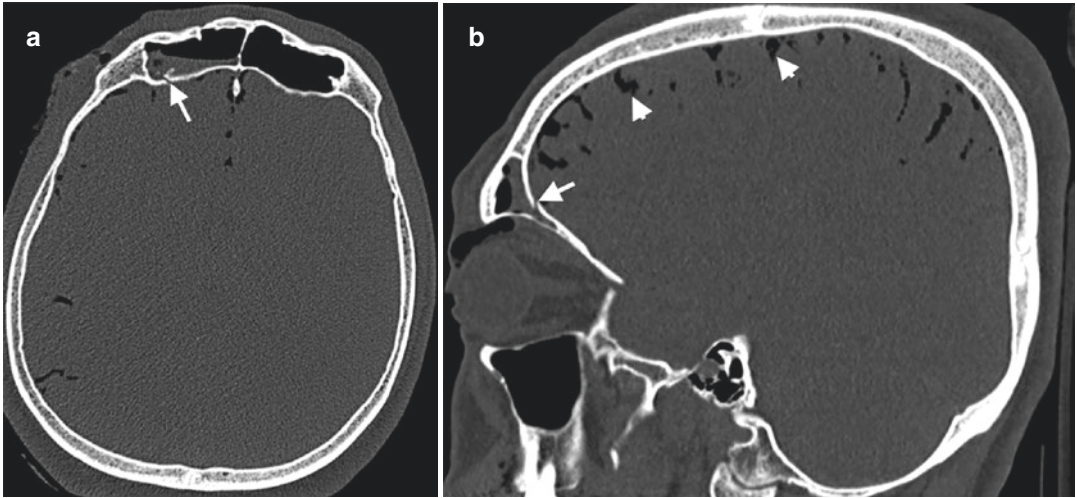
**Fig. 42** Posterior frontal sinus wall fracture. Axial (**a**) and sagittal (**b**) CT images demonstrate depressed fracture of posterior wall of the frontal sinus (arrows) and resultant pneumocephalus (arrowheads)
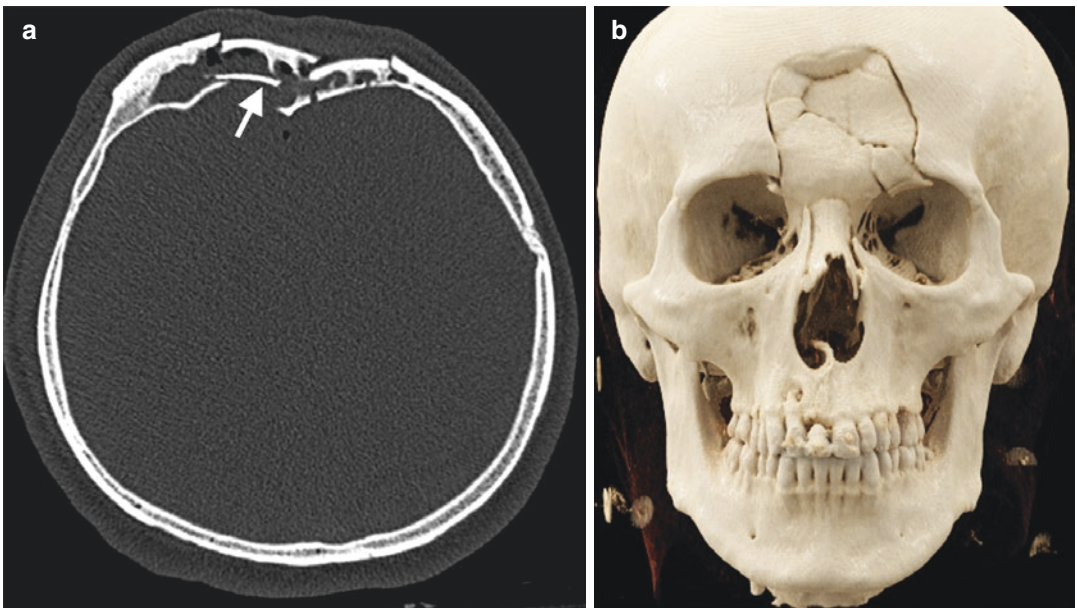
Fig. 43 Comminuted fracture of frontal sinus. Axial CT (**a**) and (**b**) CR image demonstrate comminuted fracture of frontal sinus with multiple fracture fragments (arrow)

(Mehta et al. 2012). Most of the nasal bone fractures occur in transverse plane, and fractures can be differentiated from nasociliary groove and sutures by the midline crossing nature of fracture (Koch 2014). Nasal bone fractures can be classified as simple, comminuted, and complex fractures. Complex nasal fracture is characterized by involvement of nasal bone with associated nasal septal hematoma or open nasal laceration (Table 4) (Rohrich and Adams Jr. 2000). Most nasal fractures are managed by closed reduction, while nasal bone fractures with septal fracture or dislocation with severe soft-tissue injury may necessitate
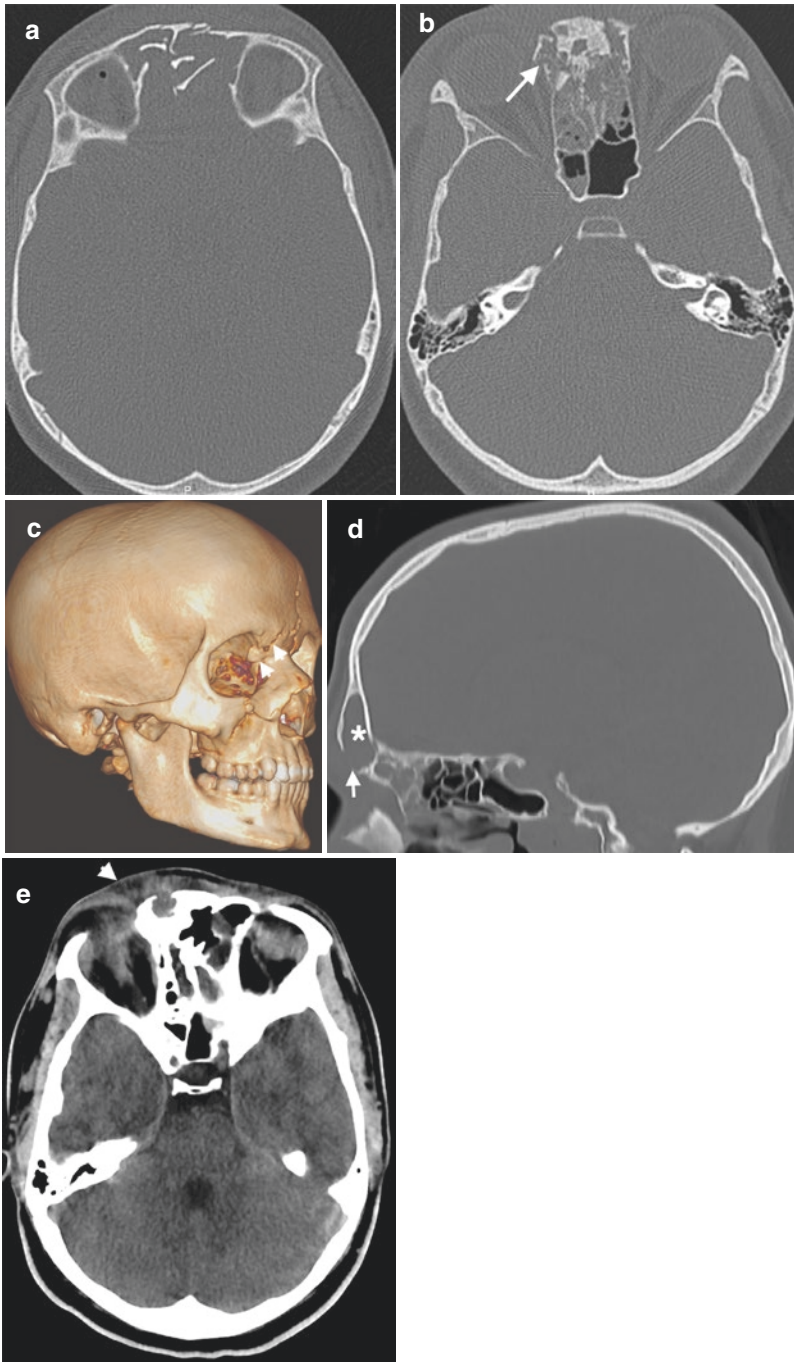
Fig. 44 Mucopyocele formation secondary to nasofrontal duct injury. (**a**) Axial CT image reveals comminuted fracture of frontal sinus. (**b**) CT image at the level of nasofrontal recess reveals extension of fracture (arrow) along anterior and middle ethmoid air cells and nasofrontal duct region. (**c**) VR image demonstrates fracture (arrowheads) involving inferomedial part of the right frontal sinus. (**d**) Sagittal image of follow-up CT examination obtained 1 month after the trauma shows defect in the anterior wall of frontal sinus (arrow). Expansion of frontal sinus with high-density content is consistent with mucocele/mucopyocele (*) formation. (**e**) Axial CT image on soft-tissue window reveals propagation of inflammation to the subcutaneous tissue (arrowhead) through wall defect that indicates mucopyocele formation

Table 4 Classification of nasal fractures (Rohrich and Adams Jr. 2000)

| Type	Category	Characteristics
I	Simple	Unilateral
II	Simple	Bilateral
III	Comminuted	Unilateral
		Bilateral
IV	Complex	Associated with septal hematoma
		Associated with open nasal laceration
V		Associated with NOE fracture/midface fracture
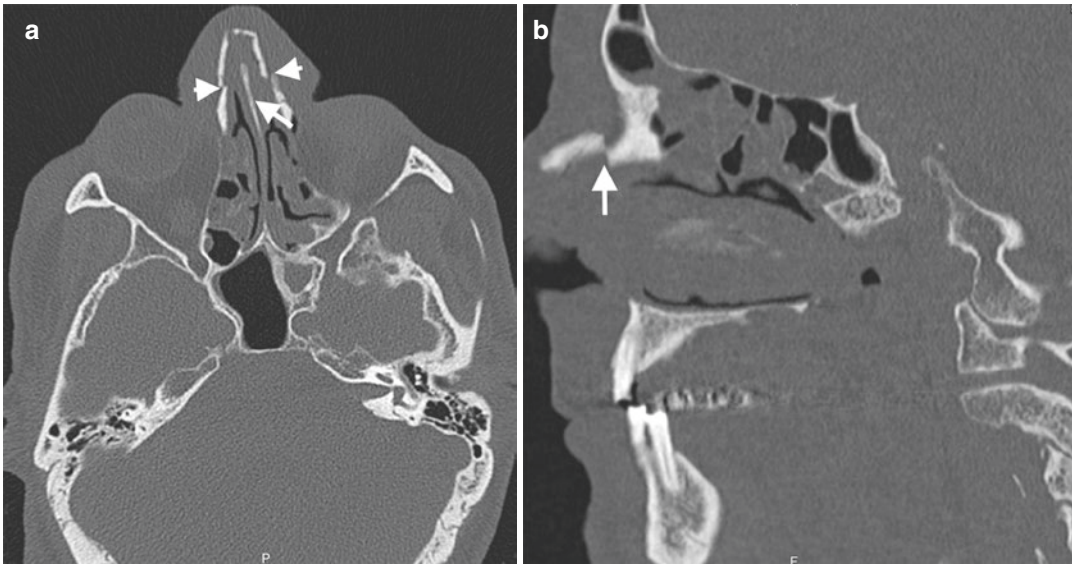
Fig. 45 Simple nasal fracture in a 60-year-old man with a history of assault. (**a**) Axial CT image demonstrates bilateral nasal bone fractures (arrowheads). The nasal sep-tum is spared (arrow). (**b**) Sagittal CT image reveals displacement of fracture fragment (arrow)

open repair (Ondik et al. 2009). Radiographic position preferred in nasal bone fracture is lateral nasal view. However, the sensitivity of lateral view radiography in nasal bone fracture ranges between 53% and 90% (Lo Casto et al. 2012). Nasal bone and septum injuries should be assessed with MPR CT images since 25% of nasal pyramid fractures may be missed on axial CT images, while sagittal reformatted images can demonstrate these fractures with a sensitivity of 85–99% (Figs. 45 and 46) (Kim et al. 2010). Missed nasal fractures may result in bony malunion, and further osteotomy can be required to reduce fracture fragments. Axial CT images are especially helpful to demonstrate

telescoping and/or comminution of nasal bone and septum. Bowing of the bony nasal septum should also be assessed on coronal CT images. Septal fractures and dislocations may cause deforming forces on fractured nasal bones during healing by exerting force on upper lateral cartilages. This may result in malunion of nasal bones after rhinoplasty (Dreizin et al. 2018). Anterior nasal spine fractures may be detected on axial and sagittal CT images (Fig. 47). Nasal fractures usually extend in transverse orientation and can cross the midline in contrast to sutures and nasociliary grooves in nasal region, which are vertically oriented and cannot cross the midline (Schmitt et al. 2014).
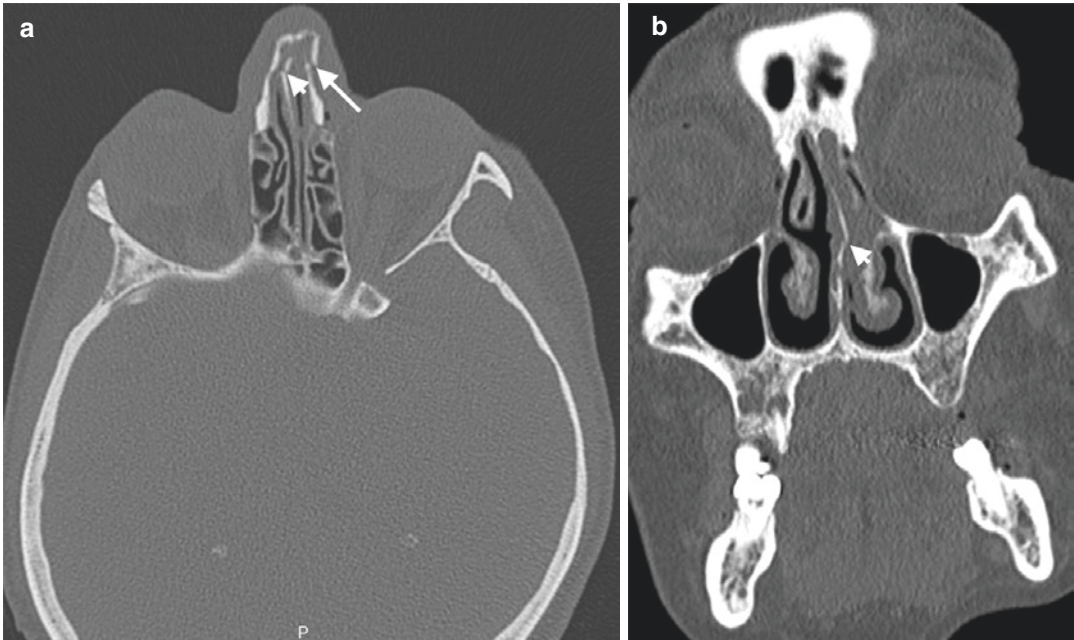
Fig. 46 Nasal bone and septum fracture in a 50-year-old woman with a history of assault. Axial (**a**) and coronal (**b**) CT images demonstrate fracture of nasal bone (arrow) and nasal septum (arrowheads)
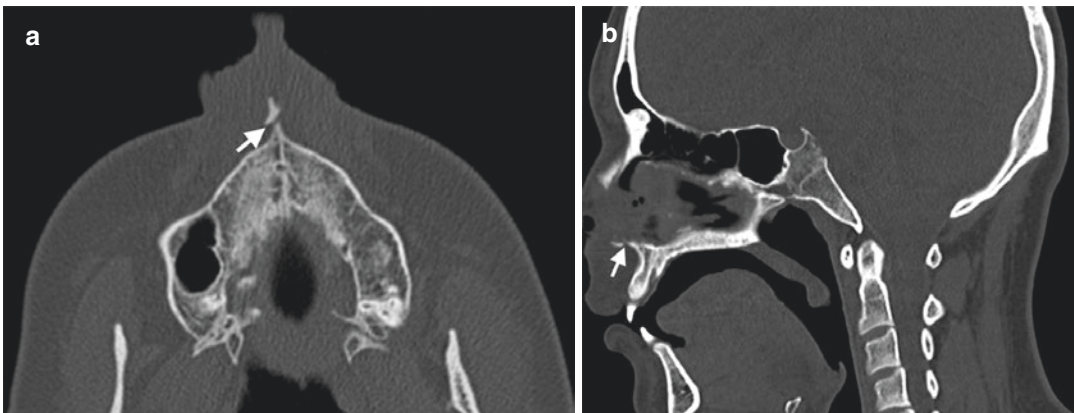
Fig. 47 Anterior nasal spine fracture in a 21-year-old woman after MVA. Axial (**a**) and sagittal (**b**) CT images demonstrate anterior nasal spine fracture (arrows)

Injury of the nasal cartilage may result in disruption of the perichondrium and formation of septal hematoma, abscess, and necrosis leading to perforation and collapse of nasal septum (Fig. 48) (Rohrich and Adams Jr. 2000). Early and prompt diagnosis of nasal bone fracture is crucial for avoiding clinical complications and cosmetic deformities such as saddle nose.

Radiation exposure and high cost of CT increase the controversies about the utility of CT for isolated nasal bone fractures since isolated bones may be detected and even reduced with manual palpation. Cone-beam tomography has been introduced as an alternative technique as an alternative with the advantages of lower radiation dose and submillimetric resolution (Bremke et al. 2009).
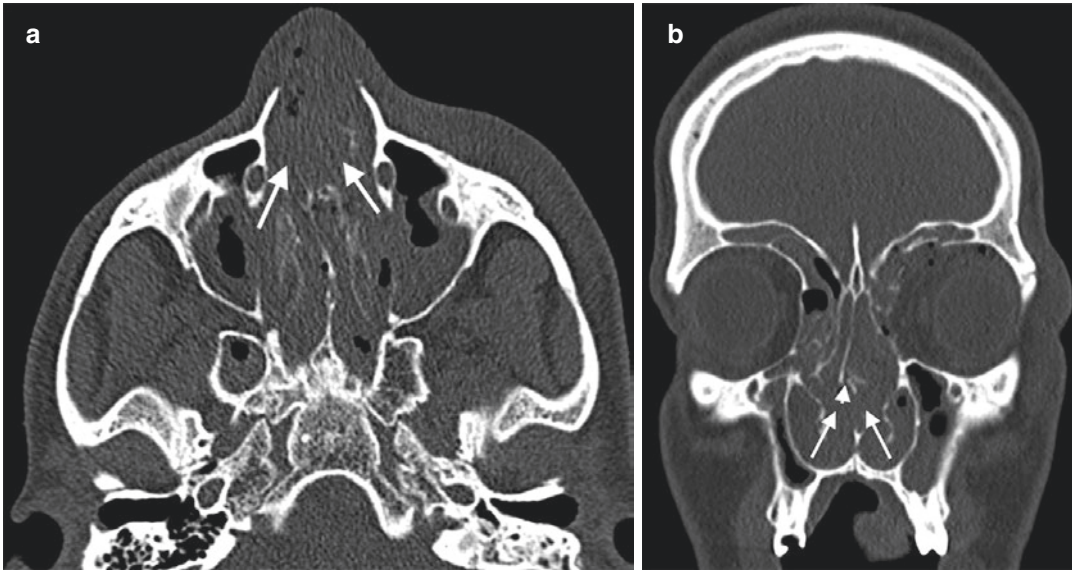
Fig. 48 Septal hematoma in a 21-year-old man after MVA. Axial (**a**) and coronal (**b**) CT images reveal abundant hemorrhage (arrows) resulted from nasal fracture

## 6.5 Naso-Orbital-Ethmoid Fractures

6.5.1 Anatomy

Naso-orbitoethmoid (NOE) region is the junction point where nose, orbita, maxilla, and ethmoid bones meet. This area is bordered superiorly by CP, laterally by thin medial orbital walls, anteriorly by bony pillar (proximal part of nasal bone, nasal process of frontal bone, and frontal process of maxilla) and posteriorly by sphenoid sinus. NOE region contains important anatomical structures including olfactory nerves, lacrimal sac, frontonasal and nasolacrimal duct, medial canthal tendon (MCT), and ethmoidal vessels (Mehta et al. 2012). MCT inserts on the lacrimal crest bordering lacrimal fossa (Ellis 3rd 2012; Elbarbary and Ali 2014). MCT supports canthus (palpebral commissures), approaches eyelid to bulbus, and maintains drainage of the lacrimal sac.

6.5.2 Fracture

Fracture of NOE complex results from high-impact force applied anteriorly to the nose. NOE fractures disrupt the confluence of medial maxillary buttress and upper transverse maxillary buttress with involvement of ethmoid bone, nasal bone, medial orbital wall, frontal process of maxilla, and inferior orbital rim (Sargent 2007; Koch 2014). Telescoping of involved bones that is characterized by posterior displacement of anterior nasal structures into the medial orbital rim, nasal septum, nasofrontal junction, and ethmoid sinuses may occur in NOE fractures (Avery et al. 2011). Diagnosis of NOE fracture is difficult compared to other midface fractures due to camouflaging effect of facial swelling in NOE area during physical examination. NOE fractures are classified according to the Markowitz and Manson classification system that is based on a central bone fragment in medial orbital rim that contains attachment of MCT (Markowitz et al. 1991). Type I NOE fracture refers to a single large segment fracture fragment of the medial orbital rim without comminution and MCT injury. In type II fractures, there is a comminuted fracture with small pieces of bones in medial orbital rim and MCT is attached to the single bone fragment. Type III NOE fracture is characterized by comminution of central fragment and disruption or avulsion of MCT from the bone (Fig. 49) (Markowitz et al. 1991). CT assessment of NOE fractures should include the type of
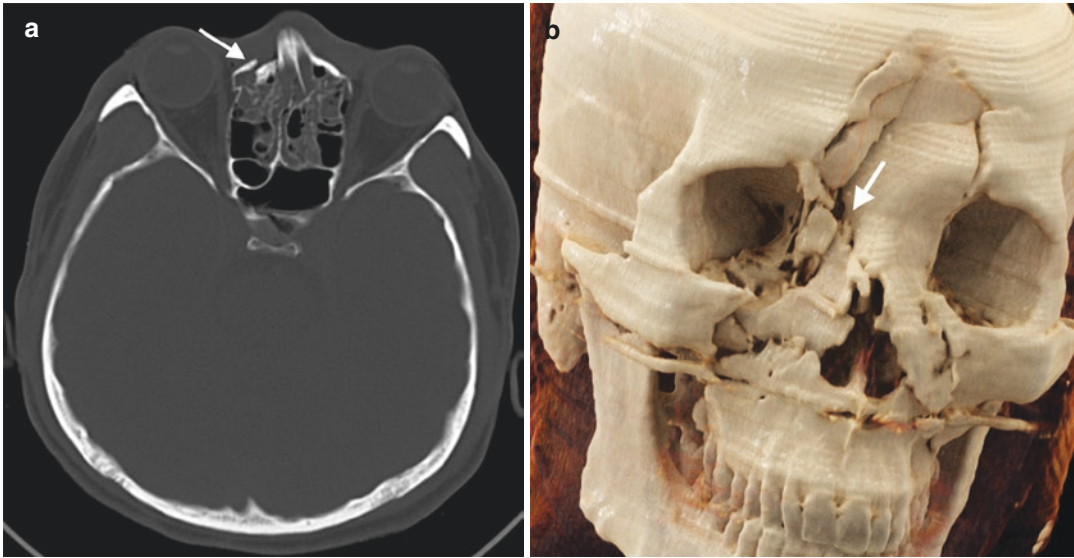
Fig. 49 Type III NOE fracture in a 19-year-old man with a history of MVA. (**a**) Axial CT image reveals right NOE fracture involving nasolacrimal duct (arrow). (**b**) CR image demonstrates type III NOE fracture (arrow) with multiple bone fragments

injury, degree of comminution and displacement, associated fractures, and soft-tissue injury. In addition to MPR images, NOE fractures necessitate assessment with 3D VR or CR images to visualize multiple curving planes of NOE region (Dreizin et al. 2018).

Injuries of NOE region are usually anteriorly directed and affect the thick nasal bone portions known as nasal bridge. Fracture of nasal bones usually presents with ethmoidal air cell fractures since ethmoidal air cells have low resistance to the impacting force compared to the nasal bone. Injury or occlusion of frontonasal duct should be suspected when axial CT images demonstrate intrusion of nasal dorsum into the anterior ethmoid complex (Potter et al. 2006; Jain et al. 2010). NOE fractures may cause impaction of nasal saddle and buckling of nasal septum resulting in the appearance of nose pushed back between the eyes. Complications of NOE fractures include CSF rhinorrhea secondary to fracture of CP, obstruction of the lacrimal system, telecanthus (increased intercanthal and interpupillary distance) due to MCT injury, facial deformity, and exophthalmos caused by decreased orbital volume (Winegar et al. 2013).

Since fractures of NOE are encountered following high-energy traumas, isolated NOE fractures uncommonly occur and Le Fort 2 and Le Fort 3 fractures usually accompany the NOE fractures (Ellis 3rd 2012). Involvement of CP should be interrogated on CT in NOE fractures due to potential complications including olfactory nerve disruption, CSF leak, pneumocephalus, or tension pneumocephalus resulting from resuscitation efforts through airways (Mehta et al. 2012).

6.6 Zygomatic Bone

6.6.1 Anatomy

Zygomatic bone, also called malar bone, contributes to the anterolateral aspect of superior face and inferior orbital rim. Zygomatic bone is an integral part of facial buttress system by articulating with frontal, maxillary bones, arch of the temporal bone, and greater wing of the sphenoid bone with the following sutures as zygomaticofrontal, zygomaticomaxillary, zygomaticotemporal, and zygomaticosphenoid suture. Zygomatic bone provides support to the orbital soft tissue

with contribution to formation of lateral and inferior orbital walls (Schmitt et al. 2014). Weakest portion of zygomatic bone is zygomaticosphenoid joint.

6.6.2 Fracture

Zygomatic bone has a tendency to fracture in maxillofacial trauma due to its superficial position and convex alignment. Zygomatic fractures occur most frequently in the form of zygomaticomaxillary complex (ZMC) fractures that result from anterolateral impact to the cheek and are characterized by separation of the zygomatic bone along its sutural attachments with spectrum of fractures with varying displacements (Mehta et al. 2012). ZMC fractures are defined as quadripod fractures since four surrounding sutures across the zygomatic bone are involved in these fractures. The four breakpoints involved in ZMC fractures are zygomaticomaxillary buttress in the inferior orbital rim, zygomaticosphenoid suture along the lateral orbital wall, zygomaticofrontal suture of the lateral orbital rim, and zygomaticotemporal suture (Sung et al. 2012).

ZMC fractures are classified with Zingg classification. Zingg type A ZMC fracture is isolated incomplete fracture involving only one limb of the zygoma (Fig. 50); type B fracture refers to classic tetrapod fracture characterized by liberated zygomatic mono-fragment (Fig. 51); and type C fracture is defined as comminuted fracture. Zingg type A fractures are subdivided into three subtypes as type A1 involving zygomatic arch, type A2 involving lateral orbital rim or wall, and type A3 involving inferior orbital rim (Dreizin et al. 2018; Zingg et al. 1992).

Zygomatic bone fractures may present on axial CT images as malar retrusion, rotation of zygomaticosphenoid suture and zygomaticomaxillary buttress, and depressed or comminuted zygomatic arch. MPR images can reveal overall ZMC malalignment and orbital volume changes (Ellis 3rd 2012; Marinho and Freire-Maia 2013). Depressed ZMC fractures usually result from rotational forces applied by masseter muscle on zygomatic bone. Severe depression or impinge-ment of depressed zygoma fracture fragments on the coronoid process of mandible and/or temporalis muscle may cause inclosure of the jaw and trismus (Marinho and Freire-Maia 2013; Dreizin et al. 2018). ZMC fractures involving lateral orbital wall may cause enophthalmos due to increased orbital volume. Frank zygomatic arch fractures may present as zygomaticotemporal suture diastasis.

Nondisplaced fractures of zygomatic bones do not require surgical treatment; however, in the setting of comminuted fractures, displacement of bone fragments and comminution degree determine the surgery planning.

6.7 Maxilla Fractures

6.7.1 Anatomy

Maxillary bones form the skeleton of face between the mouth and eye as being the projectory of midface in anteroposterior plane. Each maxillary bone consists of body, containing maxillary sinus, zygomatic, frontal, palatine, and alveolar processes. Two maxillary bones unite in the midline with intermaxillary suture and form the entire upper jaw. Maxillary bones contribute to the facial buttress system, lateral wall of the nasal cavity, orbital floor, and anterior wall of the infratemporal fossa.

6.7.2 Fracture

Fractures of maxillary bones are usually associated with the injury to the midface bony structures. Classification of maxillary fractures was made by René Le Fort in 1901 as Le Fort I, II, and III fractures. Le Fort classification mainly depends on the level of fracture line in posterior maxilla. Common imaging feature of Le Fort fractures is pterygoid plate fracture. Le Fort fractures usually present asymmetrically, and different combinations of Le Fort fractures may coexist in the same side. Le Fort I, II, and III fractures represent palatofacial dysjunction, midfacial separation, and craniofacial separation, respectively.
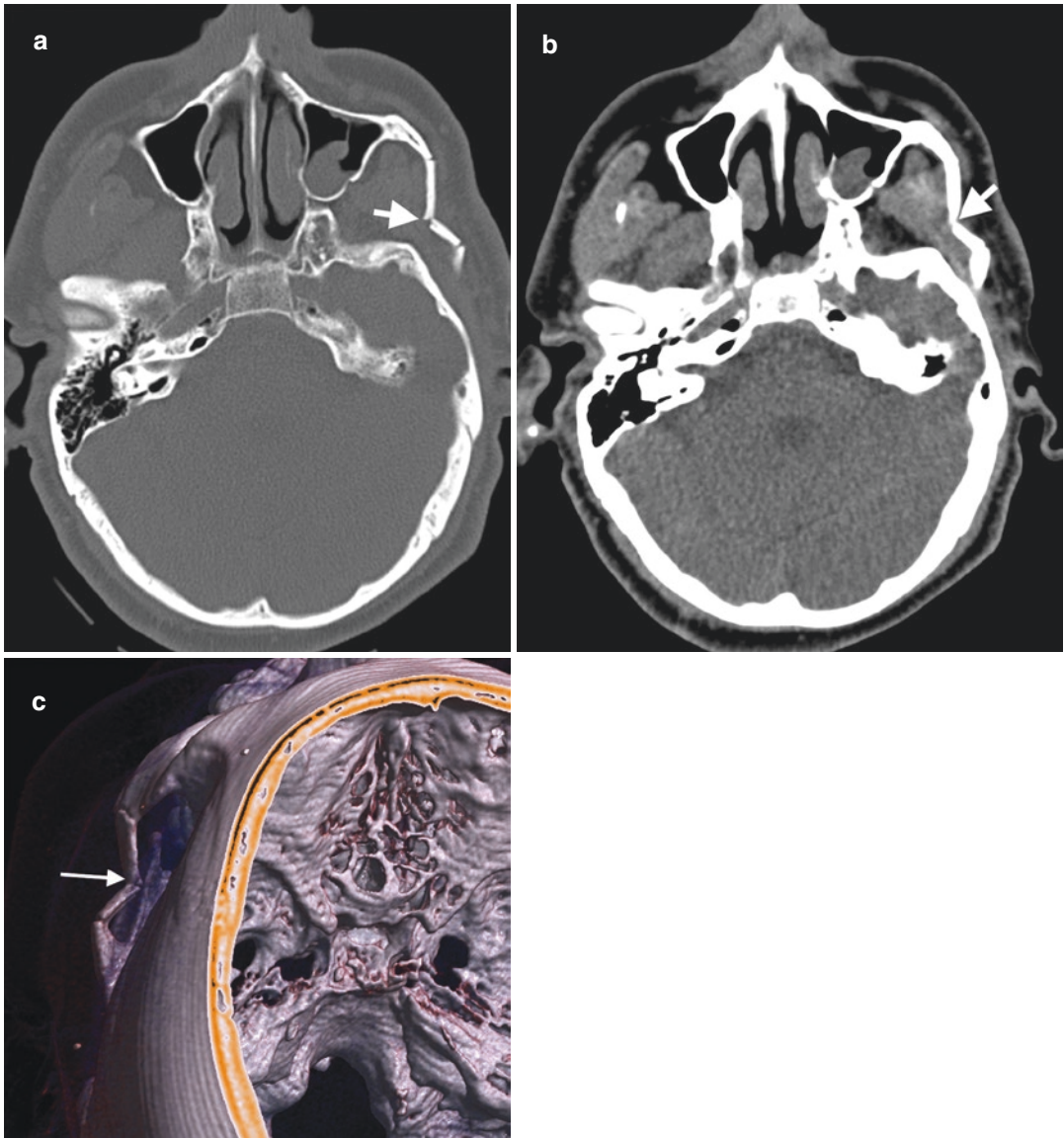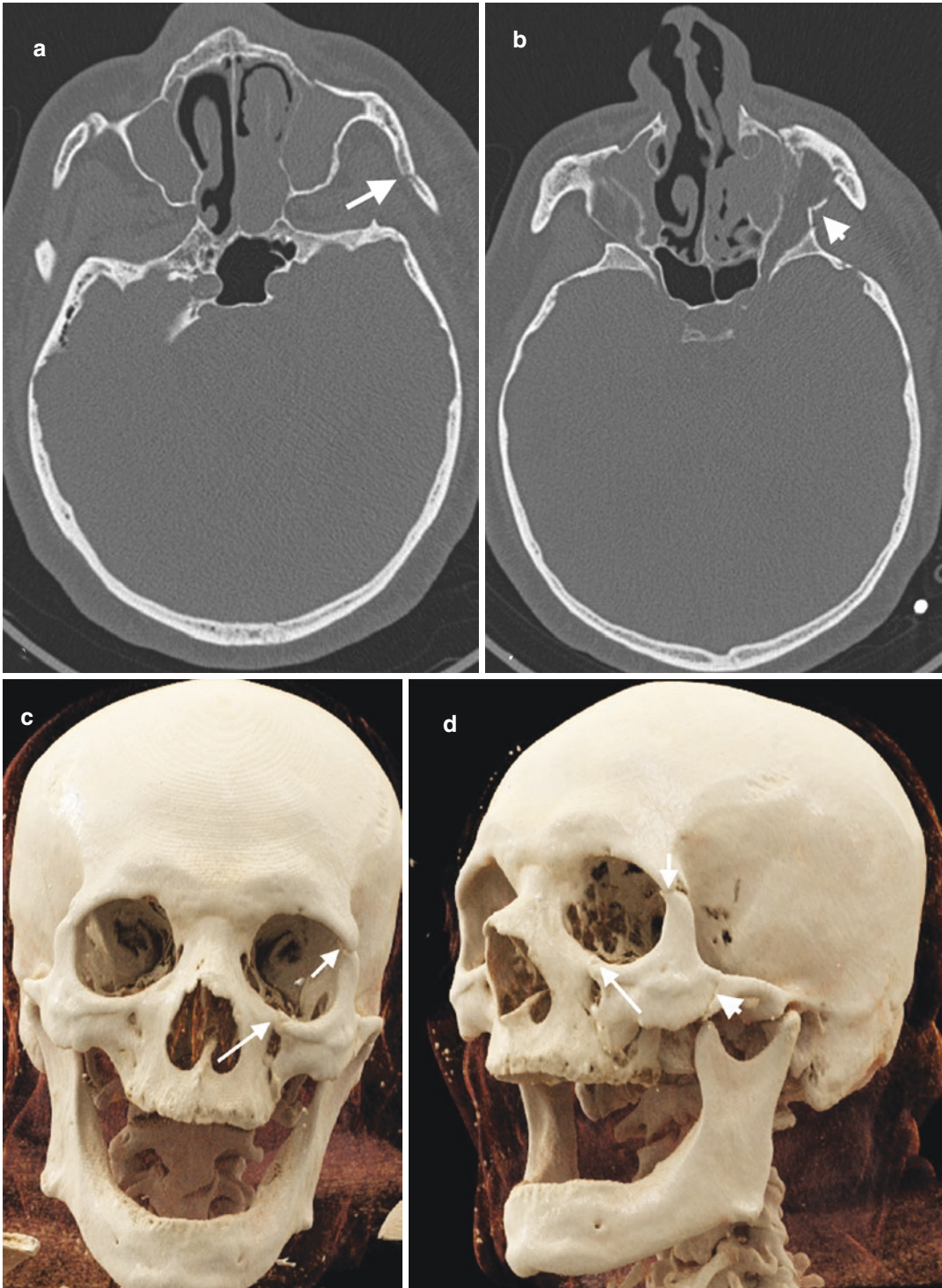
Fig. 50 Zygomatic arch fracture in a 51-year-old man presented to emergency service with malar pain and malocclusion after MVA. (**a**) Axial CT image on bone window shows depressed fracture of left zygomatic bone (arrow) with medial angulation. (**b**) Axial CT image on soft-tissue window reveals impingement of the left temporalis muscle (arrow). (**c**) VR image demonstrates depressed fracture (arrow) of left zygomatic bone

Le Fort I fracture results from horizontal impact to the upper jaw and is characterized by a transverse fracture immediately superior to the maxillary alveolar process. This fracture type crosses the floor of the maxillary sinus and lower nasal septum, anterior, medial, and lateral maxillary walls, and inferior margin of pyriform aperture and extends posteriorly into the pterygoid plates (Fig. 52). Le Fort I fracture results in separation of maxillary alveolus and/or hard palate from upper face creating malocclusion with a free-floating alveolus and hard palate

Fig. 51 Fracture of ZMC complex in a 56-year-old man after MVA. (**a**) Axial CT image shows left zygomatic arch (arrow) fracture. (**b**) Axial CT image of the same patient reveals a fracture (arrowhead) involving zygomaticosphe-noid suture. CR images with AP (**c**) and left oblique (**d**) views reveal ZMC fracture with involvement of zygomati-comaxillary suture (long arrows) and zygomaticofrontal sutures (short arrows) consistent with quadripod fracture
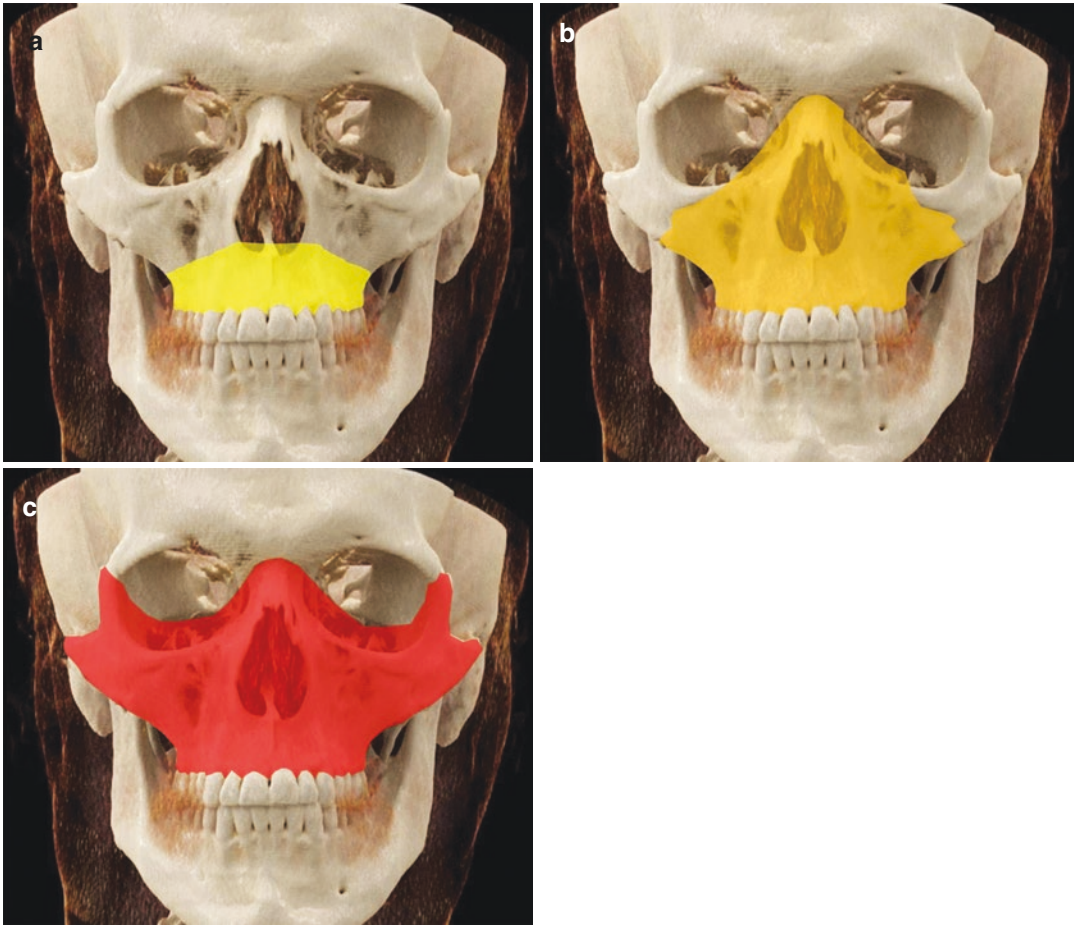
Fig. 52 Involvement areas of Le Fort fractures. (**a**) Le Fort I fracture area (yellow). (**b**) Le Fort II fracture area (orange). (**c**) Le Fort III fracture area (red)

(Mehta et al. 2012; Lo Casto et al. 2012). Infraorbital rims are spared in Le Fort I fracture. Le Fort I fractures can be best depicted on coronal and 3D CT images due to anteroposterior orientation of these fractures (Fig. 53) (Winegar et al. 2013). Fracture of pterygoid plates can be best assessed on axial CT images.

Le Fort II fracture, also called as pyramidal shape fracture, is defined as a fracture involving frontonasal suture, bilateral zygomaticomaxillary sutures, inferior orbital rim and floor, maxillary sinuses, medial orbital walls, and posteriorly pterygoid plates (Fig. 52) (Dreizin et al. 2018). Nasal bridge may be involved or spared. Le Fort II fracture creates a pyramid-shaped maxillary

fragment and separates the nasal region from the cranium. This fracture type is conceptualized as a floating maxilla. Characteristic finding of the Le Fort II fractures includes involvement of inferior orbital rim and floor. Zygomatic bone is spared in Le Fort II fractures although zygomaticomaxillary suture may be involved. Superior parts of medial maxillary, inferior part of lateral maxillary, upper transverse maxillary, and posterior maxillary buttresses are involved in Le Fort II fractures (Fig. 54).

Le Fort III fracture refers to complete craniofacial dissociation caused by suprazygomatic fracture extending horizontally from the frontonasal suture to the frontozygomatic sutures and
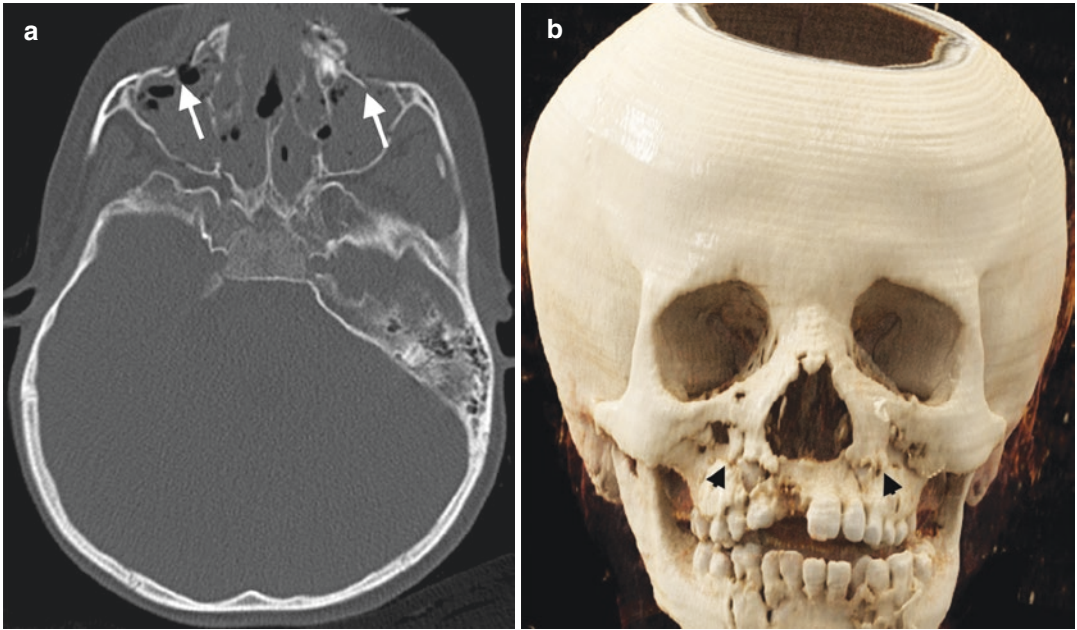
Fig. 53 Le Fort I fracture. (**a**) Axial CT image shows bilateral anterior maxillary sinus wall fractures (arrow). (**b**) CR image demonstrates Le Fort I fracture (black arrowheads) extending through superior to the maxillary alveolar process
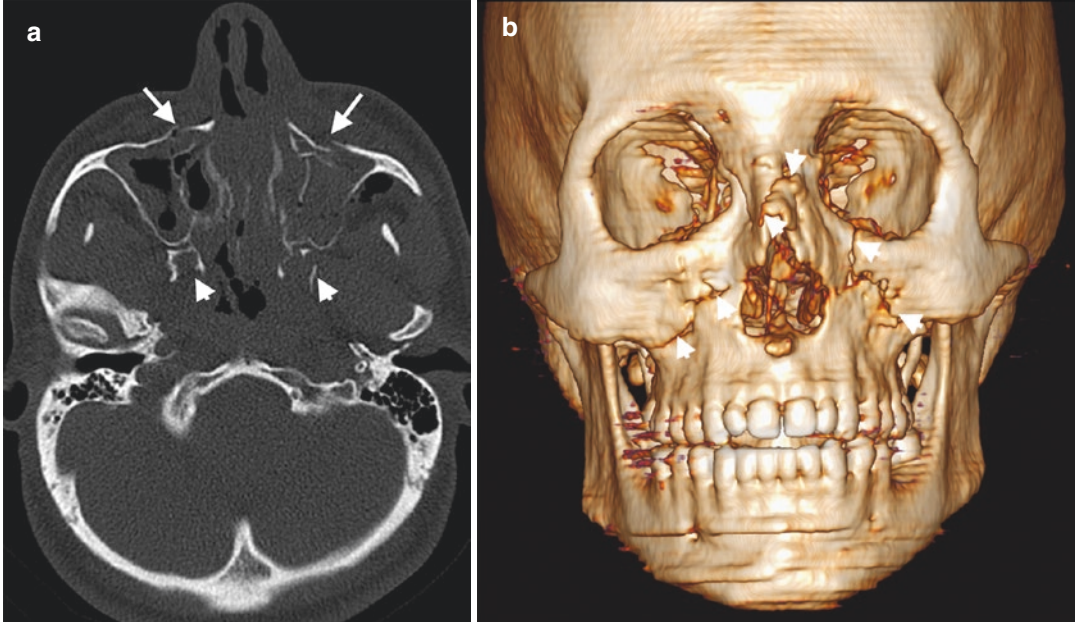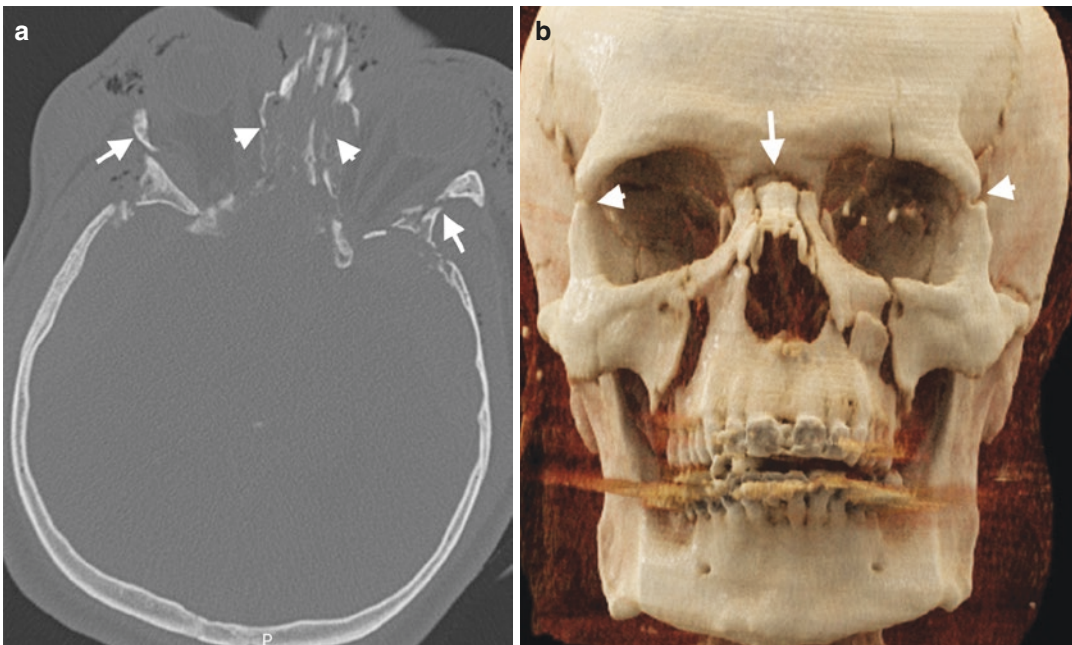

Fig. 54 Le Fort II fracture. (**a**) Axial CT image demonstrates bilateral maxillary sinus fractures (arrows) and pterygoid process fractures (arrowheads). (**b**) VR image reveals Le Fort II fracture (arrowheads) with pyramidal shape

zygomatic arches in the line traversing medial and lateral orbital walls. This fracture type separates the zygomaticofrontal sutures and zygomatic arches and terminates through the pterygoid plates resulting in separation of face from the skull base (Fig. 55) (Mehta et al. 2012). Le Fort III fractures present frequently as combinations of ZMC and NOE fractures (Dreizin et al. 2018). Superior portions of the medial maxillary and lateral maxillary, upper transverse maxillary, and posterior maxillary buttresses are involved in Le Fort III fractures (Winegar et al. 2013). Unique imaging finding of Le Fort III fracture is involvement of lateral orbital rim and zygomatic arch.

There are distinguishing imaging key points that can be used in differentiation of Le Fort fractures. Anterolateral margin of the nasal fossa is involved in only Le Fort I fracture. Le Fort II fracture differs from others by involvement of the inferior orbital rim. Le Fort III fracture is characterized as the only type that involves the zygo-

matic arch (Sung et al. 2012). Although nasofrontal suture and medial orbital wall are involved in Le Fort II and III fractures, these two fracture types can be distinguished by involvement of lateral orbital wall and zygomatic arch in Le Fort III fracture (Fig. 56) (Winegar et al. 2013). Le Fort fractures may cause significant functional and cosmetic problems and complications such as rhinorrhea, otorrhea, pneumocephalus, and intracranial complications with potential extension to carotid canal and orbital apex (Bellamy et al. 2013).

Isolated alveolar process fracture in maxillary bone involves lower transverse maxillary buttress and results from direct force applied to the alveolar process or indirect force transmitted from the underlying teeth via the base of dental crown (Winegar et al. 2013). Alveolar process fracture may cause dental root avulsion, crown or root fracture, dental intrusion or extrusion, and malocclusion (Fig. 57) (Lieger et al. 2009).

Fig. 55 Le Fort III fracture. (**a**) Axial CT image demonstrates medial (arrowheads) and lateral walls (arrows) fractures of bilateral orbita. (**b**) CR image shows Le fort III fracture extending through bilateral zygomaticofrontal suture (arrowheads) and nasal bridge (arrow). CR image also reveals bilateral Le Fort II fracture with involvement of bilateral maxillary bones extending into inferior orbital rims
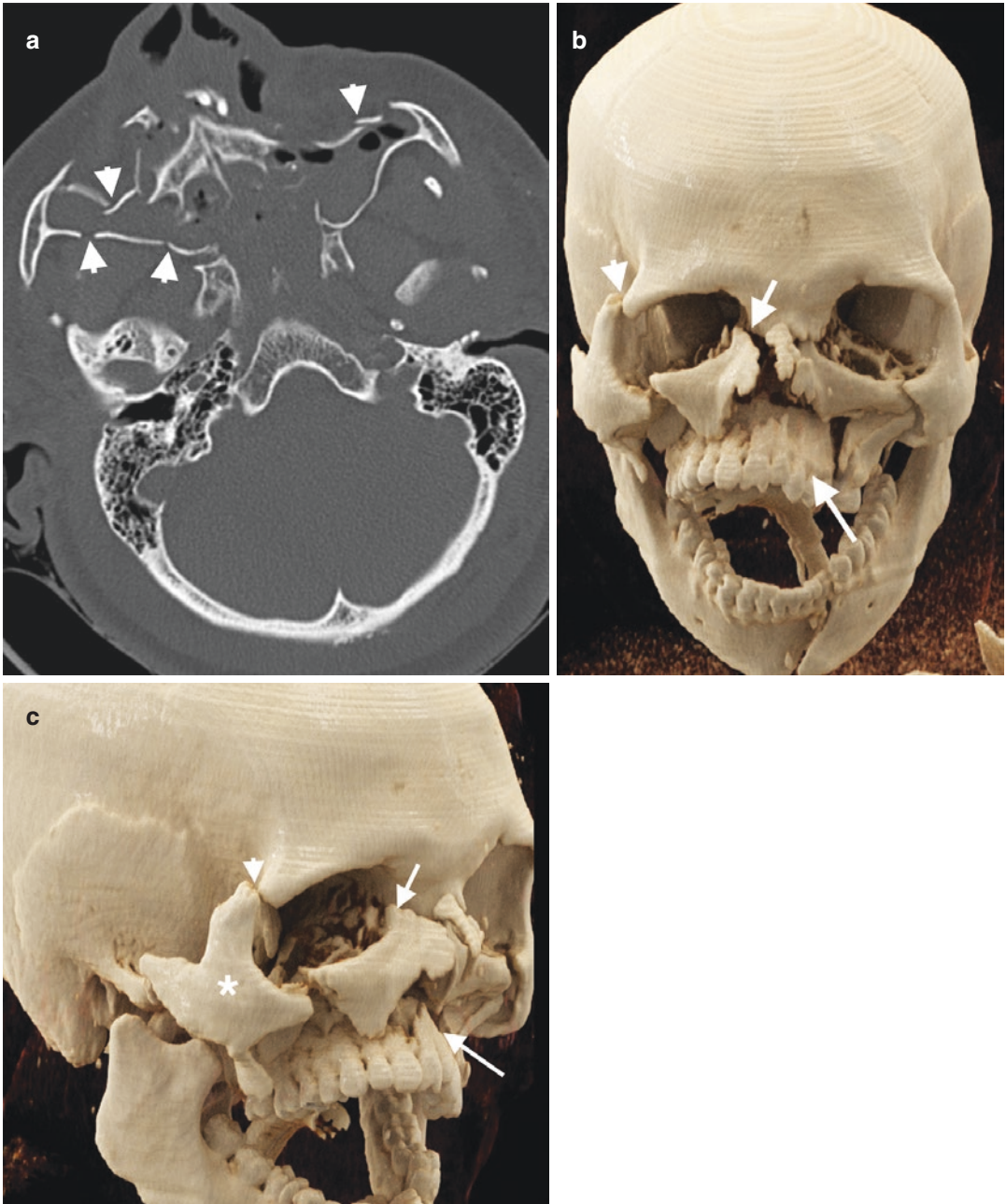
Fig. 56 Concurrent Le Fort I, II, and III fracture. (**a**) Axial CT image demonstrates multiple maxillofacial fractures (arrowheads) with telescoping. CR images at AP (**b**) and right oblique (**c**) views demonstrate Le Fort I fracture as floating palate (long arrows), Le Fort II fracture (short arrow), and Le Fort III fracture with right ZMC fracture (arrowheads). Zygomatic bone is seen as a liberated fragment (*) secondary to quadripod fracture
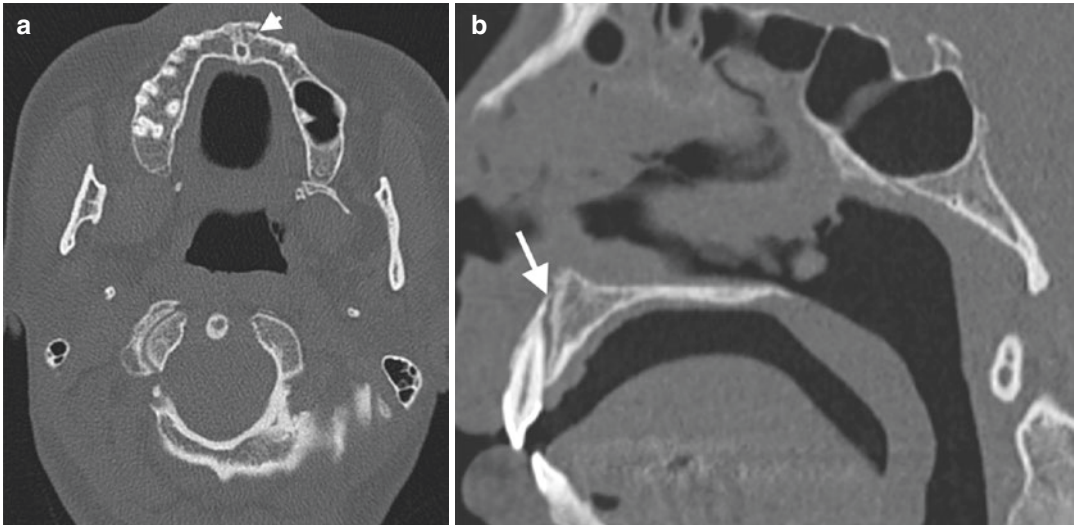
Fig. 57 Alveolar process fracture. (**a**) Axial CT image reveals a fracture (arrowhead) of left first incisive root. (**b**) Sagittal CT image demonstrates fracture (arrow) oriented in oblique position involving tooth root

6.8 Palatine Bone

6.8.1 Anatomy

The palatine bone is an L-shaped, paired bone located between the maxilla and sphenoid bone. Palatine bone is formed by a horizontal and perpendicular plate and the pyramidal process. Horizontal plate forms the posterior 1/3 portion of the hard palate, while perpendicular plate contributes to the lateral wall of the nasal cavity neighboring the pterygoid process of sphenoid bone.
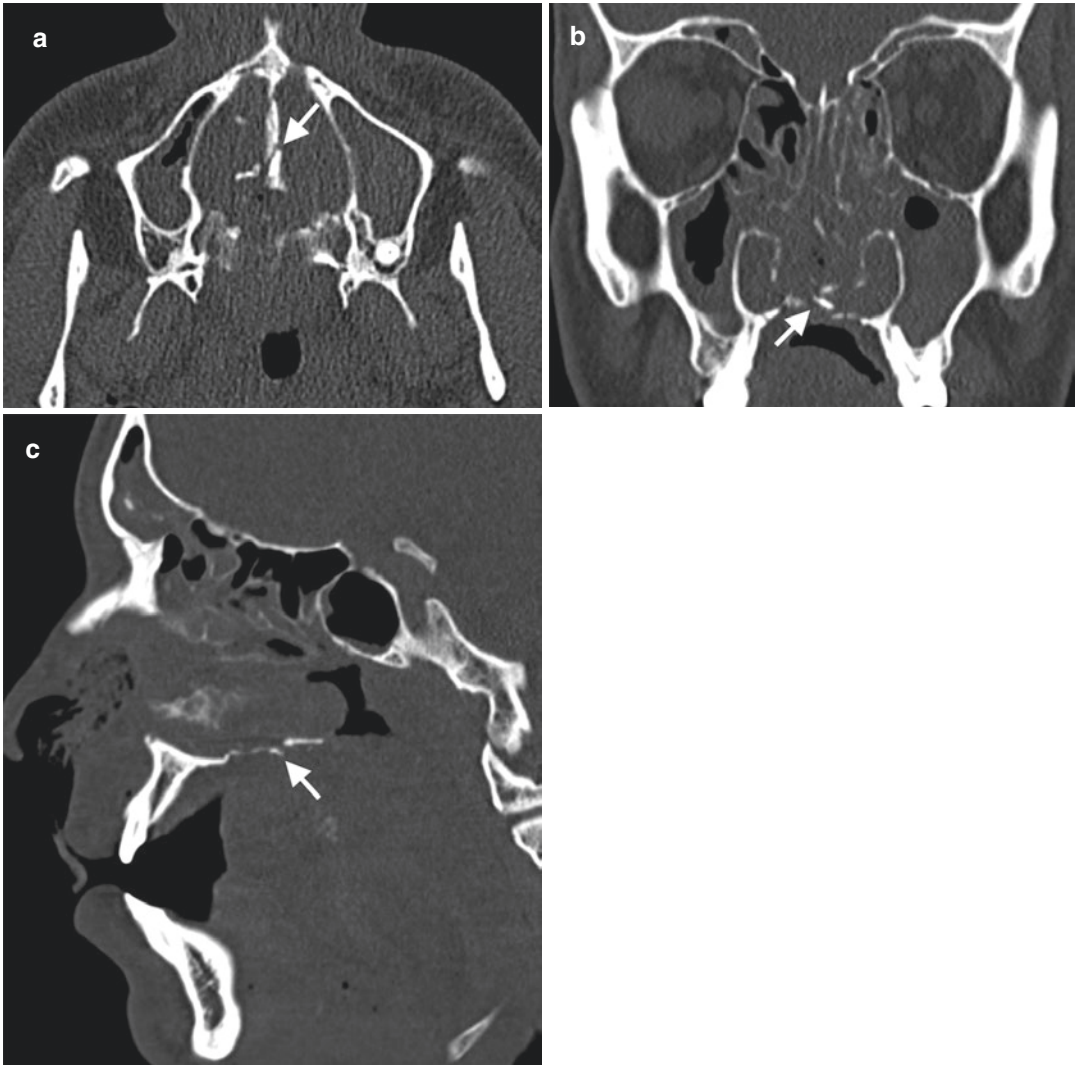
6.8.2 Fracture

Palatal fractures are encountered in up to one-half of Le Fort fractures (Chen et al. 2008). These fractures should be assessed on MPR CT images. Palatal fractures separate maxilla into left and right symmetric or asymmetric pairs (Avery et al. 2011). Classification of palatal fractures is based on direction of fractures. Type 1 palatal fractures account for 90% of fractures and oriented sagittally beginning at the maxillary alveolus and

propagating to paramedian or para-alveolar locations (Fig. 58). Type 2 fractures extend horizontally dividing the hard palate in the coronal plane. Type 3 fractures refer to complex and comminuted fractures (Chen et al. 2008).

6.9 Mandibular Fractures

6.9.1 Anatomy

The mandible is the only mobile bone in face with attachment to the skull base via two temporomandibular joints. It has a central anterior unit containing symphyseal and parasymphyseal region with bilateral horizontal body, angle, and vertical units as ramus containing condylar neck, head, subcondylar region, coronoid process, and finally alveolar process (Dreizin et al. 2016; Morrow et al. 2014). The upper border of mandibular body is the alveolar part, and the lower part is the base of the mandible. A vertical line drawn from the lower canine tooth separates parasymphysis and mandibular body,

Fig. 58 Palatine bone fracture. Axial (**a**), coronal (**b**), and sagittal (**c**) CT images demonstrate displaced fracture (arrows) of the hard palate

whereas a vertical line drawn from third molar tooth socket superiorly and masseter muscle insertion inferiorly separates angle from the body. Condyle and glenoid fossa form the synovial temporomandibular joint (Dreizin et al. 2016; Avery et al. 2011).

6.9.2 Fracture

Mandibular fractures are the second most common facial fractures with high complication rates. Motor vehicle collisions, falls, and assaults are the leading causes of mandibular fractures. Mandibular fractures tend to involve multiple places due to curved or ring-like shape of the bone. Unifocal fractures occur in 30–40% of cases, and unilateral fractures are more likely in childhood than their adult counterparts (Koch 2014; Escott and Branstetter 2008). Mandibular fractures can be classified according to the localization of fracture, which depends on the type of

Fig. 59 Mandible body fracture. (**a**) Axial CT image reveals displaced fracture (arrows) involving right side of the body. CR images with AP (**b**) and right oblique view (**c**) reveal body fracture with superoinferior course

impact, the degree of comminution, and the presence of displaced fragments (Winegar et al. 2013). An anterior impact causes symphyseal, parasymphyseal, or condylar fractures, whereas a lateral impact ends up with an angle or body fracture (King et al. 2004).

The most common mandibular fracture region is mandibular condyle and body fol-

lowed by the mandibular angle and parasymphyseal region (Patel et al. 2012). Both body and angle fractures are unfavorable fractures since masseter, temporalis, and medial pterygoid muscles may distract the proximal segment of the fractured bone superomedially (Figs. 59 and 60) (Alimohammadi 2018). Complex fracture of the mandible is observed
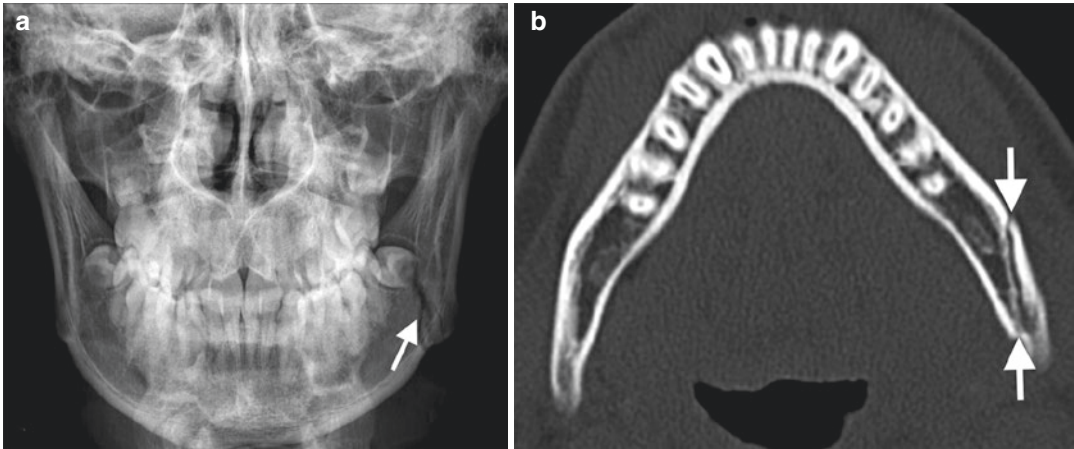
Fig. 60 Mandible angle fracture. (**a**) AP skull radiograph reveals radiolucent line (arrow) representing fracture across the left mandible angle. (**b**) Axial CT image demonstrates linear fracture (arrows) in the left mandible angle

approximately in 50% of cases, meaning that a second fracture should always be searched in a patient with mandible fracture, which is generally located contralateral side of the mandible (Fig. 61) (Alimohammadi 2018). Flail mandible is characterized by floating mandibular segment resulted from multiple fracture sites such as bilateral angle, bilateral body, or parasymphyseal and bicondylar fractures (Fig. 62). Mandible fractures with associated soft-tissue injuries may cause airway compromise and have a greater risk of malocclusion. Mandible fractures may extend to the tooth socket resulting in tooth avulsions or luxations, which is common in symphysis, body, and angle fractures. Radiologists should evaluate the airway for a possible tooth aspiration in the case of a radiolucent socket, which indicates acute tooth loss or a fragmented tooth (Raval and Rashiduddin 2011). Involvement of teeth roots in mandibular fractures should be scrutinized in radiology reports due to increased risk of subsequent osteomyelitis (Dreizin et al. 2016). Fractures involving mandibular canal by traversing the mandibular ramus, angle, and body may cause inferior alveolar nerve injury. A high association rate was also reported with mandibular fractures and cervical spine injury, which necessitates performing CT of the cervical spine in the set-ting of mandible fractures after high-speed trauma (Roccia et al. 2007). Subcondylar fractures may present with greenstick fracture of mandibular neck in children (Koch 2014).

It may be valuable for radiologists to know the indications for open surgery in mandibular fractures. Classic indications of mandibular condyle fractures include displacement of condyle into the middle cranial fossa, lateral extracapsular displacement, failure to achieve good reduction and occlusion with closed reduction techniques, bilateral subcondylar fractures, and intraarticular foreign body (Zide and Kent 1983; Montazem and Anastassov 2009). Fractures limited to condylar head, defined as intracapsular fractures, are treated conservatively or with maxillomandibular fixation. However, condylar neck fractures are defined as extracapsular fractures and generally need open surgical treatment.

Temporomandibular joint (TMJ) dislocation usually accompanies mandible fractures due to its ring-like shape. CT images demonstrate empty glenoid fossa secondary to the force of traction by lateral pterygoid muscle on condylar fracture fragments toward medially and anteriorly (Koch 2014). Fractures of mandible involving temporomandibular joint may present with otorrhea or otorrhagia secondary to the injury of EAC (Avrahami et al. 1994).
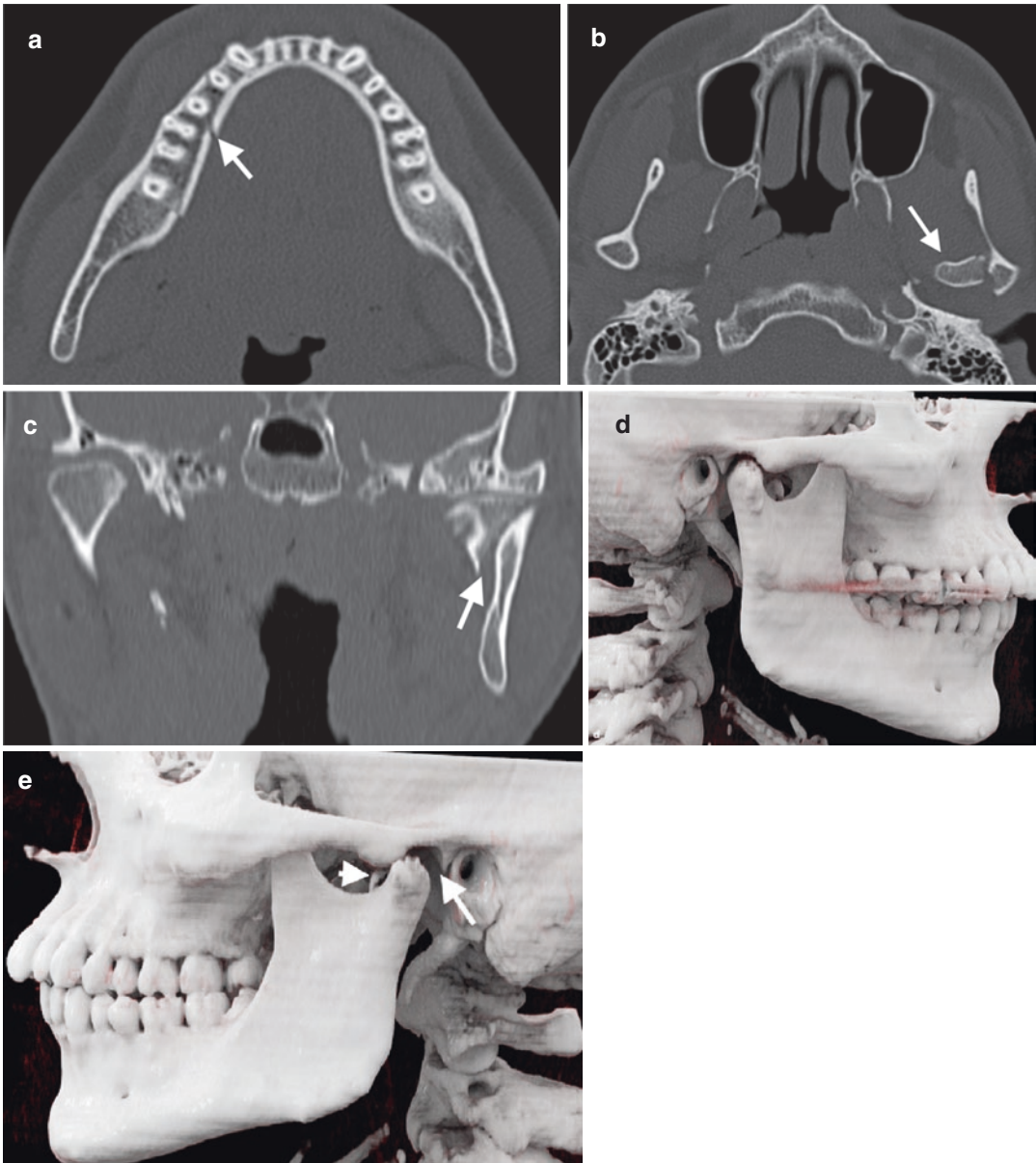
Fig. 61 Complex mandible fracture. (**a**) Axial CT image reveals a linear right mandible corpus fracture (arrow). Axial (**b**) and coronal (**c**) CT image of the same patient demonstrates left condylar fracture (arrows). (**d**) CR image demonstrates normal appearance of right mandible condyle and temporomandibular joint. (**e**) CR image reveals condylar fracture (arrow) with liberated condyle from the temporomandibular joint (arrowhead)

Dental fractures may be encountered in mandible fractures. Dental root fractures after trauma are usually horizontal and involve the single-rooted teeth. The majority of these fractures are encountered at the level of the midheight of the root (Alimohammadi 2018).
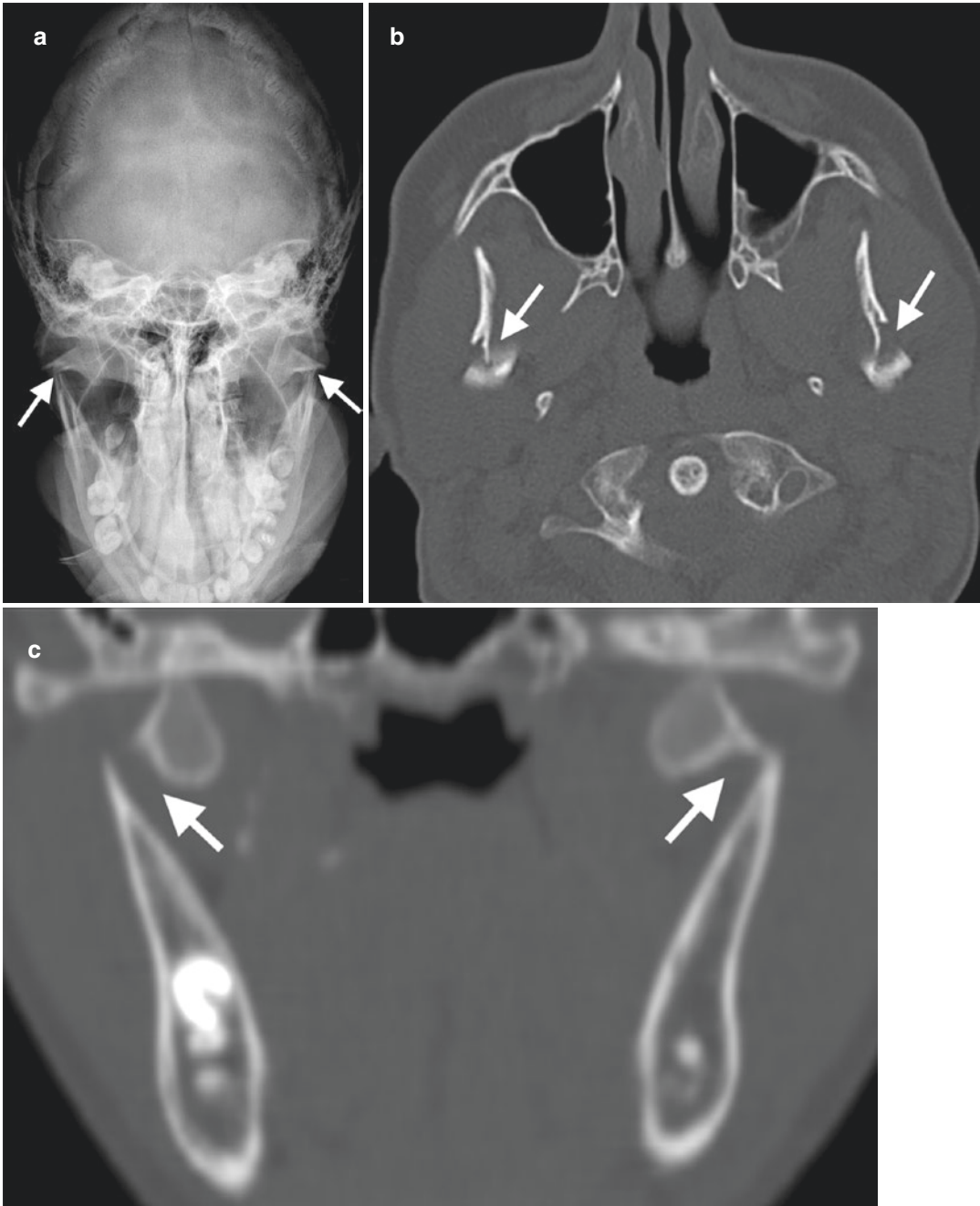
Fig. 62 Bicondylar fracture. (**a**) Towne radiography reveals bilateral condylar fractures (arrows). Axial (**b**) and coronal (**c**) CT images show bilateral condylar fractures (arrows)

7 Conclusion

Craniofacial fractures may present with simple or complex imaging findings in emergency service. A comprehensive approach with thorough knowl-edge of anatomy and mechanisms of traumatic craniofacial injury are necessary for comprehen-sive imaging assessment and management of patients. CT is a mainstay imaging technique in craniofacial fractures, which demonstrates the

Table 5 Complications of maxillofacial fractures

Fracture type	Complication
Cranium	Extra-axial hemorrhage Parenchymal injuries Sinus thrombosis Dural tears
Temporal Bone	CHL SNHL Facial and cochlear nerve injury CSF leak PLF Vascular injury
Skull base	CSF leak CN injury Vascular injury Meningitis Brainstem injury (PSB)
Orbita	Entrapment of extraocular muscles CN injury CSF leak Glob hemorrhage, perforation Lens dislocation
Frontal sinus	CSF leakage Intracranial infection Mucocele, mucopyocele
Nasal bone	Saddle nose
Naso-orbitoethmoid complex fracture	MCT injury, telecanthus CSF rhinorrhea Obstruction of the lacrimal system Facial deformity and exophthalmos
ZMC	Enophthalmos Trismus
Maxilla (Le Fort fractures)	Rhinorrhea Otorrhea Pneumocephalus Intracranial infection
Mandibular	Flail mandibular Tooth avulsions TMJ dislocation Otorrhea or otorrhagia

presence, localization, and pattern of fractures with highlighting further complications (Table 5). Multiplanar and 3D images are mandatory for delineating for complex fractures and for preoperative planning. Craniofacial fractures may present with different patterns in children due to the incomplete skeletal development. Imaging assessment of maxillofacial fractures might be more helpful for clinicians whether fractures are classified according to well-known classification schemes. Management of patients with craniofacial fractures mainly depends on imaging findings depicted on CT.

References

Alcala-Galiano A, Arribas-Garcia IJ, Martin-Perez MA, Romance A, Montalvo-Moreno JJ, Juncos JM (2008) Pediatric facial fractures: children are not just small adults. Radiographics 28(2):441–461.; quiz 618. https://doi.org/10.1148/rg.282075060

Alimohammadi R (2018) Imaging of dentoalveolar and jaw trauma. Radiol Clin N Am 56(1):105–124. https://doi.org/10.1016/j.rcl.2017.08.008

Avery LL, Susarla SM, Novelline RA (2011) Multidetector and three-dimensional CT evaluation of the patient with maxillofacial injury. Radiol Clin N Am 49(1):183–203. https://doi.org/10.1016/j.rcl.2010.07.014

Avrahami E, Frishman E, Katz R (1994) CT evaluation of otorrhagia associated with condylar fractures. Clin Radiol 49(12):877–878

Basson OJ, van Lierop AC (2009) Conductive hearing loss after head trauma: review of ossicular pathology, management and outcomes. J Laryngol Otol 123(2):177–181. https://doi.org/10.1017/S0022215108002454

Baugnon KL, Hudgins PA (2014) Skull base fractures and their complications. Neuroimaging Clin N Am 24(3):439–465., vii-viii. https://doi.org/10.1016/j.nic.2014.03.001

Bellamy JL, Mundinger GS, Reddy SK, Flores JM, Rodriguez ED, Dorafshar AH (2013) Le Fort II fractures are associated with death: a comparison of simple and complex midface fractures. J Oral Maxillofac Surg 71(9):1556–1562. https://doi.org/10.1016/j.joms.2013.04.007

Bobinski M, Shen PY, Dublin AB (2016) Basic imaging of skull base trauma. J Neurol Surg B Skull Base 77(5):381–387. https://doi.org/10.1055/s-0036-1583540

Bremke M, Wiegand S, Sesterhenn AM, Eken M, Bien S, Werner JA (2009) Digital volume tomography in the diagnosis of nasal bone fractures. Rhinology 47(2):126–131

Brodie HA, Thompson TC (1997) Management of complications from 820 temporal bone fractures. Am J Otol 18(2):188–197

Burm JS, Chung CH, Oh SJ (1999) Pure orbital blowout fracture: new concepts and importance of medial orbital blowout fracture. Plast Reconstr Surg 103(7):1839–1849

Cannon CR, Jahrsdoerfer RA (1983) Temporal bone fractures. Review of 90 cases. Arch Otolaryngol 109(5):285–288

Carter R, Anslow P (2009) Imaging of the calvarium. Semin Ultrasound CT MR 30(6):465–491

Chen CH, Wang TY, Tsay PK, Lai JB, Chen CT, Liao HT, Lin CH, Chen YR (2008) A 162-case review of palatal fracture: management strategy from a 10-year experience. Plast Reconstr Surg 121(6):2065–2073. https://doi.org/10.1097/PRS.0b013e3181706edc

Collins JM, Krishnamoorthy AK, Kubal WS, Johnson MH, Poon CS (2012) Multidetector CT of temporal

bone fractures. Semin Ultrasound CT MR 33(5):418–431. https://doi.org/10.1053/j.sult.2012.06.006

Connor SE, Tan G, Fernando R, Chaudhury N (2005) Computed tomography pseudofractures of the mid face and skull base. Clin Radiol 60(12):1268–1279. https://doi.org/10.1016/j.crad.2005.05.016

Dahiya R, Keller JD, Litofsky NS, Bankey PE, Bonassar LJ, Megerian CA (1999) Temporal bone fractures: otic capsule sparing versus otic capsule violating clinical and radiographic considerations. J Trauma 47(6):1079–1083

Dappa E, Higashigaito K, Fornaro J, Leschka S, Wildermuth S, Alkadhi H (2016) Cinematic rendering - an alternative to volume rendering for 3D computed tomography imaging. Insights Imaging 7(6):849–856. https://doi.org/10.1007/s13244-016-0518-1

Dreizin D, Nam AJ, Tirada N, Levin MD, Stein DM, Bodanapally UK, Mirvis SE, Munera F (2016) Multidetector CT of mandibular fractures, reductions, and complications: a clinically relevant primer for the radiologist. Radiographics 36(5):1539–1564. https://doi.org/10.1148/rg.2016150218

Dreizin D, Nam AJ, Diaconu SC, Bernstein MP, Bodanapally UK, Munera F (2018) Multidetector CT of midfacial fractures: classification systems, principles of reduction, and common complications. Radiographics 38(1):248–274. https://doi.org/10.1148/rg.2018170074

Elbarbary AS, Ali A (2014) Medial canthopexy of old unrepaired naso-orbito-ethmoidal (noe) traumatic telecanthus. J Craniomaxillofac Surg 42(2):106–112. https://doi.org/10.1016/j.jcms.2013.03.003

Ellis E 3rd (2012) Orbital trauma. Oral Maxillofac Surg Clin North Am 24(4):629–648. https://doi.org/10.1016/j.coms.2012.07.006

Escott EJ, Branstetter BF (2008) Incidence and characterization of unifocal mandible fractures on CT. AJNR Am J Neuroradiol 29(5):890–894. https://doi.org/10.3174/ajnr.A0973

Feiz-Erfan I, Horn EM, Theodore N, Zabramski JM, Klopfenstein JD, Lekovic GP, Albuquerque FC, Partovi S, Goslar PW, Petersen SR (2007) Incidence and pattern of direct blunt neurovascular injury associated with trauma to the skull base. J Neurosurg 107(2):364–369. https://doi.org/10.3171/JNS-07/08/0364

Ghorayeb BY, Yeakley JW (1992) Temporal bone fractures: longitudinal or oblique? The case for oblique temporal bone fractures. Laryngoscope 102(2):129–134. https://doi.org/10.1288/00005537-199202000-00005

Grant JH 3rd, Patrinely JR, Weiss AH, Kierney PC, Gruss JS (2002) Trapdoor fracture of the orbit in a pediatric population. Plast Reconstr Surg 109(2):482–489. discussion 490-485

Hijaz TA, Cento EA, Walker MT (2011) Imaging of head trauma. Radiol Clin N Am 49(1):81–103. https://doi.org/10.1016/j.rcl.2010.07.012

Ishman SL, Friedland DR (2004) Temporal bone fractures: traditional classification and clinical relevance. Laryngoscope 114(10):1734–1741. https://doi.org/10.1097/00005537-200410000-00011

Jain SA, Manchio JV, Weinzweig J (2010) Role of the sagittal view of computed tomography in evaluation of the nasofrontal ducts in frontal sinus fractures. J Craniofac Surg 21(6):1670–1673. https://doi.org/10.1097/SCS.0b013e3181f3c5f1

Jordan DR, Allen LH, White J, Harvey J, Pashby R, Esmaeli B (1998) Intervention within days for some orbital floor fractures: the white-eyed blowout. Ophthalmic Plast Reconstr Surg 14(6):379–390

Juliano AF, Ginat DT, Moonis G (2013) Imaging review of the temporal bone: part I. anatomy and inflammatory and neoplastic processes. Radiology 269(1):16–32. https://doi.org/10.1148/radiol.13120733

Karasu A, Sabanci PA, Izgi N, Imer M, Sencer A, Cansever T, Canbolat A (2008) Traumatic epidural hematomas of the posterior cranial fossa. Surg Neurol 69(3):247–251.; discussion 251-242. https://doi.org/10.1016/j.surneu.2007.02.024

Kennedy TA, Avey GD, Gentry LR (2014) Imaging of Temporal Bone Trauma. Neuroimag Clin N Am 24(3):467–486. https://doi.org/10.1016/j.nic.2014.03.003

Kienstra MA, Van Loveren H (2005) Anterior skull base fractures. Facial Plast Surg 21(3):180–186. https://doi.org/10.1055/s-2005-922857

Kim BH, Seo HS, Kim AY, Lee YS, Lee YH, Suh SI, Lee DH (2010) The diagnostic value of the sagittal multiplanar reconstruction CT images for nasal bone fractures. Clin Radiol 65(4):308–314. https://doi.org/10.1016/j.crad.2009.12.006

King RE, Scianna JM, Petruzzelli GJ (2004) Mandible fracture patterns: a suburban trauma center experience. Am J Otolaryngol 25(5):301–307

Koch BL (2014) Pediatric considerations in craniofacial trauma. Neuroimaging Clin N Am 24(3):513–529., viii. https://doi.org/10.1016/j.nic.2014.03.002

Liang W, Xiaofeng Y, Weiguo L, Wusi Q, Gang S, Xuesheng Z (2007) Traumatic carotid cavernous fistula accompanying basilar skull fracture: a study on the incidence of traumatic carotid cavernous fistula in the patients with basilar skull fracture and the prognostic analysis about traumatic carotid cavernous fistula. J Trauma 63(5):1014–1020.; discussion 1020. https://doi.org/10.1097/TA.0b013e318154c9fb

Lieger O, Zix J, Kruse A, Iizuka T (2009) Dental injuries in association with facial fractures. J Oral Maxillofac Surg 67(8):1680–1684. https://doi.org/10.1016/j.joms.2009.03.052

Little SC, Kesser BW (2006) Radiographic classification of temporal bone fractures - clinical predictability using a new system. Arch Otolaryngol Head Neck Surg 132(12):1300–1304. https://doi.org/10.1001/archotol.132.12.1300

Lloyd KM, DelGaudio JM, Hudgins PA (2008) Imaging of skull base cerebrospinal fluid leaks in adults. Radiology 248(3):725–736. https://doi.org/10.1148/radiol.2483070362

Lo Casto A, Priolo GD, Garufi A, Purpura P, Salerno S, La Tona G, Coppolino F (2012) Imaging evaluation of facial complex strut fractures. Semin Ultrasound

CT MR 33(5):396–409. https://doi.org/10.1053/j.
sult.2012.06.003

Lourenco MT, Yeakley JW, Ghorayeb BY (1995) The
"Y" sign of lateral dislocation of the incus. Am J Otol
16(3):387–392

Lui TN, Lee ST, Chang CN, Cheng WC (1993) Epidural
hematomas in the posterior cranial fossa. J Trauma
34(2):211–215

Madhusudan G, Sharma RK, Khandelwal N, Tewari MK
(2006) Nomenclature of frontobasal trauma: a new
clinicoradiographic classification. Plast Reconstr
Surg 117(7):2382–2388. https://doi.org/10.1097/01.
prs.0000218794.28670.07

Manson PN, Stanwix MG, Yaremchuk MJ, Nam AJ, Hui-
Chou H, Rodriguez ED (2009) Frontobasal fractures:
anatomical classification and clinical significance.
Plast Reconstr Surg 124(6):2096–2106. https://doi.
org/10.1097/PRS.0b013e3181bf8394

Marinho RO, Freire-Maia B (2013) Management of
fractures of the zygomaticomaxillary complex. Oral
Maxillofac Surg Clin North Am 25(4):617–636.
https://doi.org/10.1016/j.coms.2013.07.011

Markowitz BL, Manson PN, Sargent L, Vander Kolk CA,
Yaremchuk M, Glassman D, Crawley WA (1991)
Management of the medial canthal tendon in naso-
ethmoid orbital fractures: the importance of the cen-
tral fragment in classification and treatment. Plast
Reconstr Surg 87(5):843–853

McRae M, Momeni R, Narayan D (2008) Frontal sinus
fractures: a review of trends, diagnosis, treatment, and
outcomes at a level 1 trauma center in Connecticut.
Conn Med 72(3):133–138

Mehta N, Butala P, Bernstein MP (2012) The imaging
of maxillofacial trauma and its pertinence to surgical
intervention. Radiol Clin N Am 50(1):43–57. https://
doi.org/10.1016/j.rcl.2011.08.005

Menku A, Koc RK, Tucer B, Durak AC, Akdemir H
(2004) Clivus fractures: clinical presentations and
courses. Neurosurg Rev 27(3):194–198. https://doi.
org/10.1007/s10143-004-0320-2

Meriot P, Veillon F, Garcia JF, Nonent M, Jezequel J,
Bourjat P, Bellet M (1997) CT appearances of ossicu-
lar injuries. Radiographics 17(6):1445–1454. https://
doi.org/10.1148/radiographics.17.6.9397457

Metzinger SE, Guerra AB, Garcia RE (2005)
Frontal sinus fractures: management guidelines.
Facial Plast Surg 21(3):199–206. https://doi.
org/10.1055/s-2005-922860

Montazem AH, Anastassov G (2009) Management of
condylar fractures. Atlas Oral Maxillofac Surg Clin
North Am 17(1):55–69. https://doi.org/10.1016/j.
cxom.2008.11.002

Morrow BT, Samson TD, Schubert W, Mackay DR
(2014) Evidence-based medicine: mandible fractures.
Plast Reconstr Surg 134(6):1381–1390. https://doi.
org/10.1097/PRS.0000000000000717

Mulroy MH, Loyd AM, Frush DP, Verla TG, Myers BS,
Bass CR (2012) Evaluation of pediatric skull fracture
imaging techniques. Forensic Sci Int 214(1–3):167–
172. https://doi.org/10.1016/j.forsciint.2011.07.050

Mundinger GS, Dorafshar AH, Gilson MM, Mithani SK,
Manson PN, Rodriguez ED (2013) Blunt-mechanism
facial fracture patterns associated with internal carotid
artery injuries: recommendations for additional
screening criteria based on analysis of 4,398 patients.
J Oral Maxillofac Surg 71(12):2092–2100. https://doi.
org/10.1016/j.joms.2013.07.005

Nosan DK, Benecke JE Jr, Murr AH (1997) Current per-
spective on temporal bone trauma. Otolaryngol Head
Neck Surg 117(1):67–71. https://doi.org/10.1016/
S0194-59989770209-2

Ondik MP, Lipinski L, Dezfoli S, Fedok FG (2009) The
treatment of nasal fractures: a changing paradigm.
Arch Facial Plast Surg 11(5):296–302. https://doi.
org/10.1001/archfacial.2009.65

Pappachan B, Alexander M (2006) Correlating facial
fractures and cranial injuries. J Oral Maxillofac
Surg 64(7):1023–1029. https://doi.org/10.1016/j.
joms.2006.03.021

Patel R, Reid RR, Poon CS (2012) Multidetector com-
puted tomography of maxillofacial fractures: the key to
high-impact radiological reporting. Semin Ultrasound
CT MR 33(5):410–417. https://doi.org/10.1053/j.
sult.2012.06.005

Policeni BA, Smoker WR (2015) Imaging of the skull
base: anatomy and pathology. Radiol Clin N Am
53(1):1–14. https://doi.org/10.1016/j.rcl.2014.09.005

Potter JK, Muzaffar AR, Ellis E, Rohrich RJ, Hackney FL
(2006) Aesthetic management of the nasal component
of naso-orbital ethmoid fractures. Plast Reconstr Surg
117(1):10e–18e

Prosser JD, Vender JR, Solares CA (2011) Traumatic
cerebrospinal fluid leaks. Otolaryngol Clin N Am
44(4):857–873., vii. https://doi.org/10.1016/j.
otc.2011.06.007

Rafferty MA, Mc Conn Walsh R, Walsh MA (2006) A
comparison of temporal bone fracture classification
systems. Clin Otolaryngol 31(4):287–291. https://doi.
org/10.1111/j.1749-4486.2006.01267.x

Raval CB, Rashiduddin M (2011) Airway management
in patients with maxillofacial trauma - A retrospective
study of 177 cases. Saudi J Anaesth 5(1):9–14. https://
doi.org/10.4103/1658-354X.76476

Roccia F, Cassarino E, Boccaletti R, Stura G (2007)
Cervical spine fractures associated with maxil-
lofacial trauma: an 11-year review. J Craniofac
Surg 18(6):1259–1263. https://doi.org/10.1097/
scs.0b013e31814e0581

Rodriguez ED, Stanwix MG, Nam AJ, St Hilaire H,
Simmons OP, Christy MR, Grant MP, Manson PN
(2008) Twenty-six-year experience treating frontal
sinus fractures: a novel algorithm based on anatomical
fracture pattern and failure of conventional techniques.
Plast Reconstr Surg 122(6):1850–1866. https://doi.
org/10.1097/PRS.0b013e31818d58ba

Rohrich RJ, Adams WP Jr (2000) Nasal fracture manage-
ment: minimizing secondary nasal deformities. Plast
Reconstr Surg 106(2):266–273

Roth FS, Koshy JC, Goldberg JS, Soparkar CN
(2010) Pearls of orbital trauma management.

Semin Plast Surg 24(4):398–410. https://doi.org/10.1055/s-0030-1269769

Rothman MI, Simon EM, Zoarski GH, Zagardo MT (1998) Superior blowout fracture of the orbit: the blowup fracture. AJNR Am J Neuroradiol 19(8):1448–1449

Saigal K, Winokur RS, Finden S, Taub D, Pribitkin E (2005) Use of three-dimensional computerized tomography reconstruction in complex facial trauma. Facial Plast Surg 21(3):214–220. https://doi.org/10.1055/s-2005-922862

Samii M, Tatagiba M (2002) Skull base trauma: diagnosis and management. Neurol Res 24(2):147–156. https://doi.org/10.1179/016164102101199693

Sanchez T, Stewart D, Walvick M, Swischuk L (2010) Skull fracture vs. accessory sutures: how can we tell the difference? Emerg Radiol 17(5):413–418. https://doi.org/10.1007/s10140-010-0877-8

Sargent LA (2007) Nasoethmoid orbital fractures: diagnosis and treatment. Plast Reconstr Surg 120(7 Suppl 2):16S–31S. https://doi.org/10.1097/01.prs.0000260731.01178.18

Schmitt PJ, Barrett DM, Christophel JJ, Leiva-Salinas C, Mukherjee S, Shaffrey ME (2014) Surgical perspectives in craniofacial trauma. Neuroimaging Clin N Am 24(3):531–552., viii-ix. https://doi.org/10.1016/j.nic.2014.03.007

Sung EK, Nadgir RN, Sakai O (2012) Computed tomographic imaging in head and neck trauma: what the radiologist needs to know. Semin Roentgenol 47(4):320–329. https://doi.org/10.1053/j.ro.2012.05.002

Swartz JD (2001) Temporal bone trauma. Semin Ultrasound CT MR 22(3):219–228

Tress EE, Clark RS, Foley LM, Alexander H, Hickey RW, Drabek T, Kochanek PM, Manole MD (2014) Blood brain barrier is impermeable to solutes and permeable to water after experimental pediatric cardiac arrest. Neurosci Lett 578:17–21. https://doi.org/10.1016/j.neulet.2014.06.020

Uzelac A, Gean AD (2014) Orbital and facial fractures. Neuroimaging Clin N Am 24(3):407–424., vii. https://doi.org/10.1016/j.nic.2014.03.008

Watanabe K, Kida W (2012) Images in clinical medicine. Battle's sign. N Engl J Med 367(12):1135. https://doi.org/10.1056/NEJMicm1100820

Weir P, Suttner NJ, Flynn P, McAuley D (2006) Lesson of the week - Normal skull suture variant mimicking intentional injury. Brit Med J 332(7548):1020–1021. https://doi.org/10.1136/bmj.332.7548.1020

Winegar BA, Murillo H, Tantiwongkosi B (2013) Spectrum of critical imaging findings in complex facial skeletal trauma. Radiographics 33(1):3–19. https://doi.org/10.1148/rg.331125080

Yetiser S, Hidir Y, Gonul E (2008) Facial nerve problems and hearing loss in patients with temporal bone fractures: demographic data. J Trauma 65(6):1314–1320. https://doi.org/10.1097/TA.0b013e3180eead57

Yilmazlar S, Arslan E, Kocaeli H, Dogan S, Aksoy K, Korfali E, Doygun M (2006) Cerebrospinal fluid leakage complicating skull base fractures: analysis of 81 cases. Neurosurg Rev 29(1):64–71. https://doi.org/10.1007/s10143-005-0396-3

Zdilla MJ, Russell ML, Koons AW, Bliss KN, Mangus KR (2018) Metopism: a Study of the Persistent Metopic Suture. J Craniofac Surg 29(1):204–208. https://doi.org/10.1097/SCS.0000000000004030

Zide MF, Kent JN (1983) Indications for open reduction of mandibular condyle fractures. J Oral Maxillofac Surg 41(2):89–98

Zimmermann CE, Troulis MJ, Kaban LB (2005) Pediatric facial fractures: recent advances in prevention, diagnosis and management. Int J Oral Maxillofac Surg 34(8):823–833. https://doi.org/10.1016/j.ijom.2005.06.015

Zingg M, Laedrach K, Chen J, Chowdhury K, Vuillemin T, Sutter F, Raveh J (1992) Classification and treatment of zygomatic fractures: a review of 1,025 cases. J Oral Maxillofac Surg 50(8):778–790